# Wear behavior of Ti-6Al-4V for Joint Implants manufactured by Electron Beam Melting

By

**Sanjay Shrestha**

Submitted in Partial Fulfillment of the Requirements

for the Degree of

**Master of Science in Engineering**

in the

Mechanical Engineering

Program

**YOUNGSTOWN STATE UNIVERSITY**

May, 2017

Wear behavior of Ti-6Al-4V for joint implants manufactured
by Electron Beam Melting

Sanjay Shrestha

I hereby release this thesis to the public. I understand that this thesis will be made available from the OhioLINK ETD Center and the Maag Library Circulation Desk for public access. I also authorize the University or other individuals to make copies of this thesis as needed for scholarly research.

Signature:

_____
Sanjay Shrestha, Student                                      Date

Approvals:

_____
*Dr. Jae Joong Ryu*, Thesis Advisor                            Date

_____
*Dr. Guha Manogharan*, Thesis Co-Advisor                       Date

_____
*Dr. Virgil Solomon*, Committee Member                         Date

_____
*Dr. Brett Conner*, Committee Member                           Date

_____
*Dr. Hazel Marie*, Committee Member                            Date

_____
*Dr. Salvatore A. Sanders*, Dean of Graduate Studies           Date

# Abstract

*Powder bed-based EBM technology has been utilized for biomedical implant manufacturing. Anisotropic microstructure of the EBM built implant surface is closely related to wear and corrosion behavior during active biomechanical loadings. A series of experimental studies are performed in ambient and in simulated body fluids. Before the wear tests, local properties are characterized by depth-sensing nanoindentation technique to obtain mechanical properties due to surface anisotropy. Microscale (fretting) contact experiments are conducted using the pure titanium spherical head of instrumented nanoindenter as a well-characterized single asperity to apply controlled sliding contact motions on the EBM-built Ti6Al4V surfaces. Removed volume of the surface is measured to determine the influence of surface anisotropy, contact stress, and synovial environment effect on surface fatigue response. Experimental results indicate that the layer-by-layer fashion of the EBM-built part develops anisotropic microstructure and the microstructure leads to variable tribological properties. In ambient environment with controlled humidity (35%), the wear behavior of the EBM built Ti6Al4V displays a significant dependence on both build orientation and sliding motions. In phosphate buffer saline (PBS) solution, wear rate for most of the EBM built parts increase under the cyclic sliding contacts, while the surface anisotropy effect becomes less significant. The result implies electrochemical attack largely affects the wear of transversely developed parts. However, wear rate of mill-annealed Ti6Al4V decreases in PBS compared to the wear in ambient. Material removal rates in protein-hyaluronic acid solution are significantly reduced in all specimens and sliding directions. Presence of major components in synovial fluids improves lubricative effect under the same mechanical stimuli. In conclusion, the grain morphology and*

*orientation significantly changes the tribological and electrochemical performance of the EBM made Ti6AL4V. Experimental results demonstrate a detailed damage phenomena of joint implant materials manufactured by additive process. Therefore, the detailed understanding will successfully provide a quantitative framework for the influence of building orientation of metal deposition on nano- and micro- scale titanium implant surface damage.*

# Acknowledgements

*First and foremost, I would like to thank Dr. Jae Joong Ryu, the primary advisor of my thesis committee for making the completion of this research possible. Dr. Ryu has helped me immensely throughout this research and has taught me a wealth of knowledge through his understanding, experience and steady patience. Apart from his academic guidance, I have always been a recipient of his generosity and good advice. No words are enough to thank Dr. Ryu for what he has done for me.*

*I will always be grateful to the members of my advisory committee, Dr. Hazel Marie, Dr. Virgil Solomon, Dr. Guha Manogharan and Dr. Brett Conner, for taking time from their busy schedule and serving on my thesis committee. Their valuable insights regarding revisions to be made served me to polish my thesis very well.*

*I am grateful to the opportunities provided to me by YSU, Department of Mechanical and Industrial Engineering. A big thank you to all my colleagues who were directly or indirectly involved with me. I am very thankful to Mathew Caputo for helping me get all the electron microscopy results. I greatly appreciate the time and effort he put towards the work for me. Additionally, I would like to thank Angelo Pelini, Muhammad Qasim Riaz and Mercedes Ferraro, my lab-mates for their helpful discussion regarding my research. I would also like to forward my gratitude to Jeff, Braden and John at Nanovea for helping me resolve problems encountered with the nano-indenter machine.*

*Lastly, I am truly grateful to my family for helping and supporting me to succeed in my life. Their constant guidance and encouragement has helped me overcome tough situations and propelled me to be a better person.*

# Table of Contents

# List of Figures

x

# List of Tables

# List of Papers

## Paper I as Chapter 3

*Experimental Investigation of Micro-scale Contact Fatigue Wear damage on EBM-built Ti6Al4V surface*

Published at Proceeding of the 2016 Industrial and Systems Engineering Research Conference

S. Shrestha, J. Ryu and GP. Manogharan
Department of Mechanical and Industrial Engineering, Youngstown State University, Youngstown, OH, 44555

## Paper II as Chapter 4

*Wear response of EBM built Ti6Al4V: combined effect from anisotropic surface grain and frictional motion*

A paper to be submitted to Journal of Materials Engineering and Performance

S. Shrestha, J. Ryu and GP. Manogharan
Department of Mechanical and Industrial Engineering, Youngstown State University, Youngstown, OH, 44555

## Paper III as Chapter 5

*Wear behavior of electron beam melting (EBM) and wrought Ti6Al4V alloys in simulated physiological solution: Effects of anisotropy, sliding orientation and microstructure*

A paper to be submitted to Journal of Materials Engineering and Performance

S. Shrestha, J. Ryu and GP. Manogharan
Department of Mechanical and Industrial Engineering, Youngstown State University, Youngstown, OH, 44555

# Abbreviations

| Variable | Description |
|----------|-------------|
| Ti6Al4V | Titanium 6-Vanadium 4-Aluminum |
| DDM | Direct Digital Manufacturing |
| CAD | Computer Aided Design |
| AM | Additive Manufacturing |
| RP | Rapid Prototyping |
| SFF | Solid Freeform Fabrication |
| LM | Layered Manufacturing |
| 3D | 3-Dimensional |
| ASTM | American Society of Testing and Materials |
| ISO | International Organization for Standards |
| STL | Stereolithography |
| 2D | 2-Dimensional |
| PBF | Poly Butylene Furanoate (Polymer) |
| CT | Computed Tomography |
| MRI | Magnetic Resonance Imaging |
| EBM/EBAM | Electron Beam (additive) Melting |
| SLM | Selective Laser Melting |
| CoCr | Cobalt Chromium |

| | |
|---|---|
| IUD | Intra-Uterine Devices |
| TJR | Total Joint Replacement |
| THR/THJR | Total Hip Replacement |
| SEM | Scanning Electron Microscope |
| SE | Secondary Electrons |
| BSE | Backscattered Electrons |
| EDX | Energy-dispersive X-Ray Spectroscopy |
| XRD | X-Ray Diffraction |
| CP | Commercially Pure |
| EDM | Electrical Discharge Machining |
| CLA | Center-line Average |
| SiC | Silicon Carbide |
| HF | Hydrogen Flouride |
| $H_2O$ | Water |
| $HNO_3$ | Nitric Acid |
| FFT | Fast Fourier Transform |
| IIT | Instrumented Indentation Technique |
| HCP | Hexagonal Closed Pack |
| BCC | Body Centered Cubic |
| MoM | Metal-on-Metal |
| MoP | Metal-on-Polyethylene |
| CoC | Ceramic-on-Ceramic |

# Chapter 1: General Introduction

## 1.1 Background

The joints or articulations inside a human body play a vital role in the overall functioning of the body as it helps to perform most of the activities in every step of our day-to-day lives. The primary function of the joints is allowing the bones to articulate among each other. Joints can be classified according to the load bearing capability and degrees of freedom. The primary load bearing joints are called synovial joints or freely movable joints. These joints are prevented from direct physical contact to one another by an articular cartilage, which is comprised of connective tissue. The bones around the joints possess a synovial cavity, inside of which lies the synovial fluid, an extremely good natural lubricant, which works under a wide range of loading conditions giving a useful life of approximately 70 years for the articulating bones. However, due to old age, degenerative joint diseases such as arthritis, accidents, fracture or excessive strain, the joints are disturbed from their natural normal working state and even young and dynamic people have to often undergo total joint replacements. Foremost among the advances in the orthopedic implants is the total replacement of joints with modular implant designs. Both the thighbone (femur) and the socket are replaced with artificial hip parts called an implant or prosthesis.

The study of biomaterials dates back to around 4000 years when Egyptians and Romans used linen for sutures, gold, iron for dental replacements, and wood for toe replacements with little to no knowledge about the possible adverse effects such as corrosion. After the World War II, materials such as Nylon, Teflon, silicone, stainless steel and titanium were used. However, the development in the orthopedic implants were

restricted because of a major hindrance – the lack of a metal that would be well tolerated by the tissues. Along with the development in the recent years on better diagnostic tools and surgical procedures came the advancement in the knowledge of materials propelling the need for finding better implant materials that have superior properties and compatibility to the human body. Various classes of materials that are used nowadays as biomaterials include metals, metallic-alloys, polymers, ceramics and composites. Among metals, the most commonly used surgical implants are manufactured out of the three types of materials: austenitic stainless steel, cobalt-chromium alloy, titanium, and its alloys. Ti-alloys are considered as the most suitable implant materials primarily because of the low density and young's modulus as compared to the other metals. Due to the presence of the tenacious solid oxide layer, which gives the maximum passivity for titanium and its derivatives, they are also considered as the most corrosion resistant material.

Metallic implants inserted into the body will eventually undergo some degradation by a variety of mechanisms. Total hip replacements are not once in a lifetime guarantee procedure as the chances of revision surgery required depends on lifestyles, activities, and postoperative care of the patients. The primary reasons associated with the revision surgery are aseptic loosening (failure of the bond between an implant and bone in the absence of any infection), dislocation of prosthesis, implant breakage, wear of acetabular, to name a few. Biomedical literature is unable to pinpoint whether the synovial membrane functions correctly after it is cut to perform a total joint replacement. As a result, if the synovial membrane functions abnormally then over time, it usually is accompanied by direct contact between the articulating surfaces causing asperity contacts that results in the generation of heat and particulate wear debris body. The implant degradation if severe will either be

absorbed, altered or expelled in shape and will result in emitting toxic particles that can be extremely harmful to the living host when absorbed systemically or locally into the host tissue. The useful life of the prosthesis is seriously restricted due to continuous surface fatigue and corrosion at the joint interface. The adverse tissue reaction lowers pH level and increases protein concentration in the synovial fluid, thereby inducing corrosion attack in the implant material.

## 1.2 Additive Manufacturing

AM is one of the emerging manufacturing technologies in which a part is produced by adding materials from bottom up approach layer-by-layer from a 3D computer aided design (CAD) model. This technique differs from the traditional manufacturing in which the material is subtracted off from the stock material to produce the final product. Synonyms for AM include Rapid Prototyping (RP), Solid freeform Fabrication (SFF), Layered manufacturing (LM), Direct digital manufacturing (DDM), and/or 3D printing.
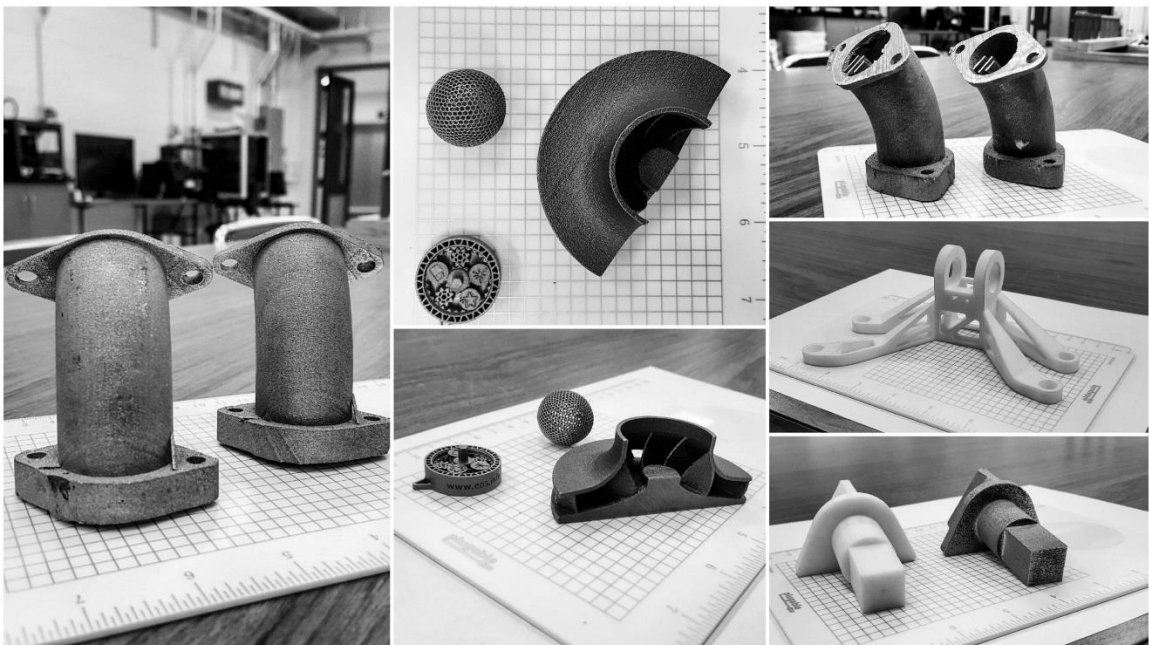


*Figure 1: Examples of parts manufactured by additive manufacturing*

The exact start of AM is difficult to trace, but literature suggests that AM started in the mid-1980s with Stereolithography [1]. During the late 1980s and early 1990s, with the advent of digital revolution and economic development and availability of industrial laser, numerous AM processes emerged from across the globe; Laminated object manufacturing, Selective laser sintering, Fused deposition modeling, 3D printing to name a few. Initially, geometrical prototypes and design models were of primary focus, but after almost two and a half decades, AM has recognized itself as a promising commercial manufacturing technology capable of producing near-net functional parts. Examples of parts fabricated by AM processes are shown in *Figure 1*.

### 1.2.1 Categories of Additive Manufacturing

Various types of additive manufacturing processes are classified. The primary difference in most AM processes is in the type of the material used and the way in which the layers are deposited or the primary source of energy utilized to manufacture the part. The root problem while classifying AM processes into a single type is realized when AM processes, which produces parts in a similar manner, end up being grouped separately (example: stereo-lithography and material jetting with photopolymers) while some processes get lumped together in an odd combination (selective laser sintering combined with 3D printing). Hence, multiple classifications have been presented in the literature, but a perfect one is often difficult to find, as it is wise to identify each individual process for its unique features rather than lump categorizing into a single branch. For reference, there are seven different AM process categories developed by ASTM International given by [2]:

- *Binder Jetting*: a processes in which a binder is printed on top of a powder bed to bind particles together to form part cross section.

- *Directed Energy Deposition*: a single deposition device is used to supply energy to process the material and simultaneously deposit a material (usually powder or wire)

- *Material Extrusion*: a process in which plastic material is heated to a malleable state and extruded through a nozzle; nozzle scans in a pattern, which produces the part's cross-section

- *Material Jetting*: similar to binder jetting, but instead of a binder, ink-jet printing is involved

- *Powder Bed Fusion*: a processes in which a high-energy beam source (usually laser beam or electron beam) is channeled onto a container filled with powder to fuse the particles together

- *Sheet Lamination*: the layer deposition in these processes occur with the material being in the form of a sheet

- *Vat Polymerization*: a processes that utilizes curable resins contained in a vat, which are processed by selectively delivering energy

Another common method to categorize AM based on the materials used are as follows [3]:

- *Liquid Polymer Systems*: liquid photopolymers, hydrogels as the material

- *Discrete Particle Systems*: powders used as the material

- *Molten Material Systems*: materials used in their molten state that flow from a pre-heating chamber where they are heated above their melting point and supplied to produce parts through a delivery system

- *Solid Sheet Systems*: uses some type of energy source laser to cut out profiles from sheet paper to make cross sections piled up with a heat-activated resin to form a 3D part

- *Metal Systems*: direct metal process which utilizes metal powders as the input material, and

- *Hybrid Systems*: a system that incorporates both additive and subtractive assembly



*Figure 2: Biomedical and Aerospace parts manufactured by Electron Beam Melting (EBM) [4]*

## 1.2.2 Electron Beam Melting (EBM)

Electron Beam Melting (EBM) or alternatively referred to as Electron Beam Additive Melting (EBAM) is an AM technique developed at Chalmers University of Technology in the late 1900s and commercialized by Swedish company Arcam AB in the early 2000s [3, 4]. This technique falls under the category of powder bed fusion for metals of AM and is a rapid manufacturing process capable of producing fully dense parts on a layer-by-layer basis with properties equal to those of wrought materials. Each powdered layer is interacted by a high power electron beam that generates the energy needed to melt and solidify subsequently added layers until the whole part is completed [5]. The beam scans the powder bed on a track provided by the 3D CAD-drawing. The EBM process is largely similar to the laser based AM process, however, the difference being an electron beam used as the primary source of energy to fuse the powder particles instead of a laser source [6]. Because of high coupling efficiency with deposited materials, the EBM process is applicable to a variety of metallic materials such as Ti-6Al-4V, CoCr alloys, H13 steel as well as highly reflective materials such as aluminum (Al) [7, 8]. In the biomedical industry,

EBM is increasingly used to produce standard as well as custom orthopedic implants, dental replacements including full set of teeth, while in the aerospace industry, EBM finds its applications directly in the fabrication of components of commercial and military aircraft, space applications, missiles and various subsystems like engines and accessories [7].

*Figure 3* illustrates a schematic representation of the key components of an EBM system. An electron gun generates an electron beam. A current of 60 kEV is applied to the tungsten filament enveloped inside a grid-cup or anode. This heats the filament up to 2200-2700 K generating a beam of electrons that runs down the drift tube. The drift tube comprises of two sets of magnetic lenses: astigmatism lens and focus lens. The first lens corrects for astigmatism and generates a circular beam, whereas, the second lens focuses the beam into correct diameter, a small 0.1 mm spot. Finally, the deflection lens controls the motion of the electron beam and scans the electron beam across the build area.

The build vacuum chamber is where the build process is occurring. During the buildup process, thin layer of powder anywhere in between 50 to 100 μm is spread over the build table via a rake, by fetching the powder from powder hoppers. When the high-speed electron beam travelling at half the speed of light strikes the metal powder, the kinetic energy instantly gets converted to thermal energy thereby raising the temperature above the melting point of the powder and rapidly liquefying the powder bed. Once the successful melting of the layer of powder occurs, the build table is lowered by a distance equal to the thickness of the layer. The rake spreads the powder over to create a new layer for the beam to scan and consequently the powder is melted. The process repeats itself over several cycles until the build is completed.
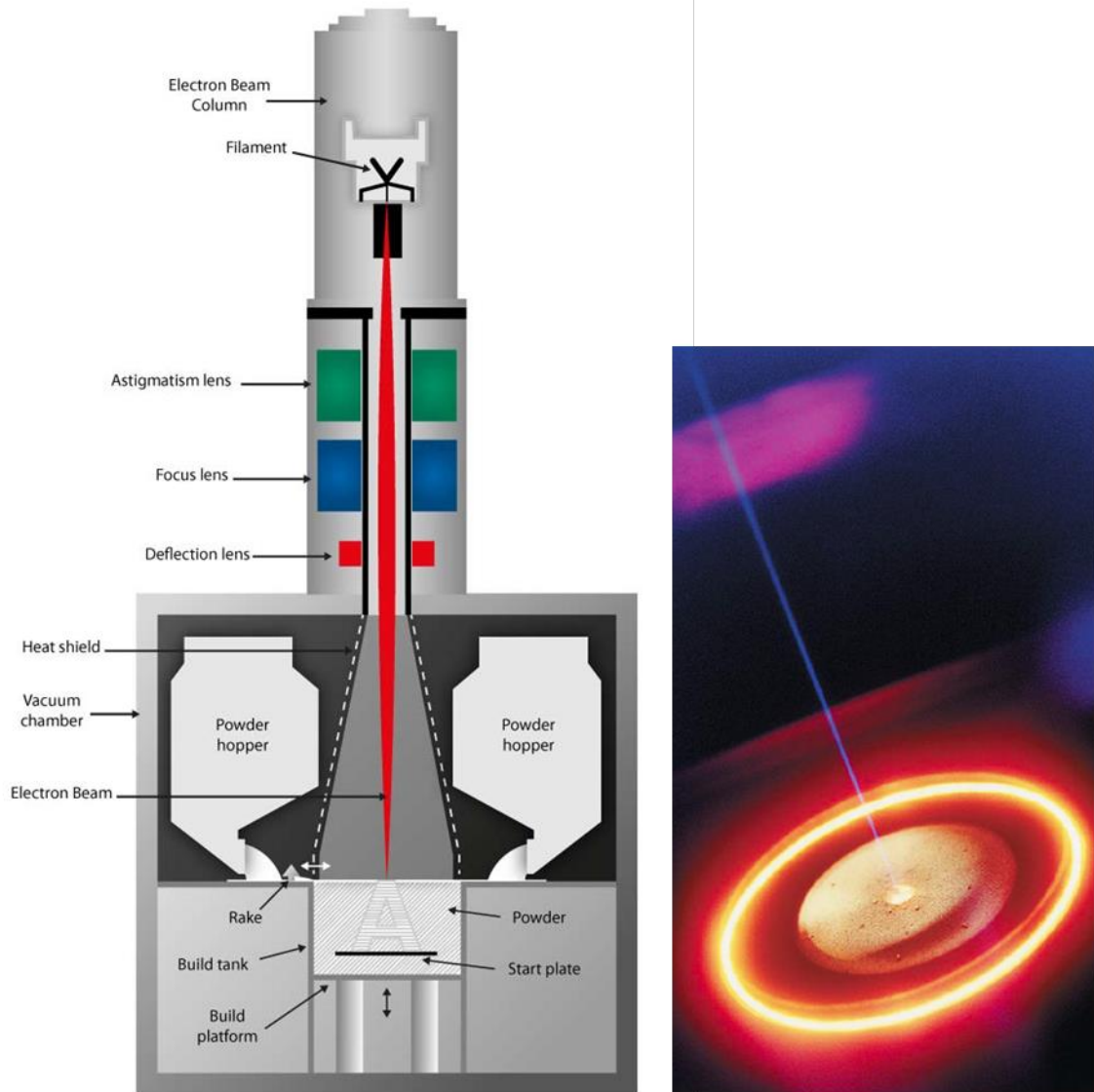
*Figure 3: (a) Schematic representation of EBM system components [9] (b) Electron beam melting the powder inside the build chamber [5]*

Throughout the build process, the electron beam gun and the build table remain stationery, as no mechanical parts are needed to deflect the beam. Due to this, very high scanning speed up to 1000 m/s and fast build rates, up to 60 cm$^3$/hour can be achieved. As compared to selective laser melting (SLM) and other metal additive processes, EBM offers three to five times faster processing speed. The EBM build is maintained in a vacuum to prevent a loss of energy caused by the fast moving electrons colliding with air or gas molecule

making the EBM process energy-efficient, about five to ten times greater than the laser technology. Another benefit it offers is the vacuum supports processing of reactive metals such as titanium that have high affinity for oxygen [5].

Safdar *et al.* [10] categorized the phase transformation of Ti6Al4V when used as an EBM material into three steps. The phase transformation from the liquefied temperature to room temperature follows:

1) Rapid cooling from melt pool temperature of 1900 $^o$C to isothermal hold at ~700 $^o$C;

2) Holding of the build at ~700 $^o$C for entire duration of build; and

3) Slow cooling from ~700 $^o$C to room temperature once the built is finished.

The isothermal hold during the second step has namely two advantages; relatively high temperature in build chamber improves the build rate and secondly eliminates the needs of annealing.

### 1.2.3 Advantages and Disadvantages of AM

Debatable either way, additive manufacturing is not always the right choice; it has distinct advantages and disadvantages. Since additive manufacturing provides an upper hand in customizability as compared to the conventional machining manufacturing, the decision lies with each company and engineer to adopt the additive manufacturing processes that best fits their requirements. Listed below are some of the advantages of AM:

- Low or zero tooling costs with limited or no requirement of fixtures

- Shorter lead time and reduced machining time

- High component complexity with net or near net shaped parts in materials that are hard to machine conventionally like hard metals, ceramics, composites

9

- Reduced material waste or optimal raw material usage and energy consumption

- Wide range of choice of new materials such as polymers (thermoplastics, thermosetters, photo-polyers), metals, ceramics, wood-like parts, composites [11], while including multi-material parts made by soft core and hard skin [12]

- Freeform nature of the process is also beneficial for the production of medical implants

Although AM has promising advantages, the biggest drawbacks of AM processes are the poor surface finish and dimensional accuracy. The first challenge can be related to the inherent nature of the AM processes. Any AM process requires a direct import of a CAD model to generate a surface tessellation to represent the geometry into a set of tool paths. This is usually done with an STL or StereoLithography or Standard Tessellation Language file. Toolpath generation serves as a limitation because most 3D printing processes require deposition done in a layer-by-layer manner, which start with a 3D space tessellation and end with 2D building strategy. This results in discontinuities among the added layers resulting in poorer surface finishes [13]. Another outcome is the common stair stepping effect, which is a normal phenomenon in nearly all AM-fabricated parts. Usually it is referred to as the stair case effect, and is typically associated with fabricated parts that have curved features. In addition, the situation is even worse for droplet-based printing where the fused matter is no longer connected in any direction and hence discontinuities appear in all building directions. In almost all cases, the deposited layer thickness and the resolution of the materials used will hinder the surface finish, and with other factors combined, result in poorer dimensional accuracy, structural and mechanical anisotropies [13, 14]. The layer-by-layer approach causes surface anisotropy, which causes the material

to have mechanical, electrical, thermal, and optical properties inferior to the conventionally manufactured counterparts [15]. On the other hand, for metallic products, it has been reported that the material properties are similar or even better [16, 17]. Hence, it is understood that material properties of the parts produced by AM technology have mixed reviews, requiring the need for rigorous studies in the future.

One facet where AM technology still cannot fully compete with traditional manufacturing is in the mass production arena. In addition, size limitations, time, and costs are a hindrance when the large-sized objects are to be fabricated. In one of the AM processes where liquid polymers are used to build an object, lack of material strength acts as a drawback while manufacturing large parts. The amount of time needed for the build process is significantly high. In terms of investment cost, the cost of most, if not many, 3D printers can go as high as 100,000 for higher end models [17]. So, to incorporate AM technology in a traditional company profitability should be thoroughly considered.

## 1.2.4 Applications of AM

As previously mentioned, AM, because of its significant benefits over the course of its development throughout the years, has found its use in a variety of applications. The improvements in accuracy, cost reductions, mechanical properties of machines and parts made by them has added benefits to the global industry. The three major industrial sectors, Aerospace, Automotive and Biomedical, have benefited the most because of the complex geometric capabilities, customizability, ability to produce parts based on patient-specific data, and the time saved to manufacture these products [3]. Particularly in aerospace and automotive industries, the prime use of AM is seen by bringing flexibility to smaller, core components that are rather advantageous to be made by AM rather than mass-produced.

- Automotive Industry

AM applications in product development sector was dominated by automotive industry, as they were the earliest adopters of AM. As of 2013, approximately 17% of all expenditures on AM have come up from these companies. AM applications in these sectors include rapid prototyping, rapid tooling, custom parts on luxury cars or replacement parts on antique models. Formula one and NASCAR have also used AM as an integral part of their car performance development processes in the form of parts made from nonstructural polymer PBFs, scaled models for wind tunnel testing and parts for full size cars [3]. Ford Motor Company has utilized in-house additive manufacturing processes to improve its tooling fabrication processes. The company has created prototypes, and used sand cores and molds, which was estimated to have saved around four months in production and millions of dollars in the process [18].

- Aerospace Industry

As previously mentioned, the primary advantage for production applications in aerospace is the ability to produce complex engineered geometries with a limited number of processing steps. Weight savings and structural integrity are key in aerospace. Lighter materials mean less energy requirements. Hence, AM processed metals like Titanium and Aluminum serve as the best-fit materials, which have higher strength to weight ratios. Lattice structured (honeycomb) or parts with internal cores (hollow) where weight is saved without losing strength are some of the striking examples of use of AM in aerospace. A perfect example includes an A320 nacelle hinge bracket ash shown in *Figure 4* originally designed as a cast steel part, but later redesigned to be made of Ti-alloy using PBF [19],

reportedly, trimming 10 kg off the mass of the bracket, saving approximately 40% in weight [3].
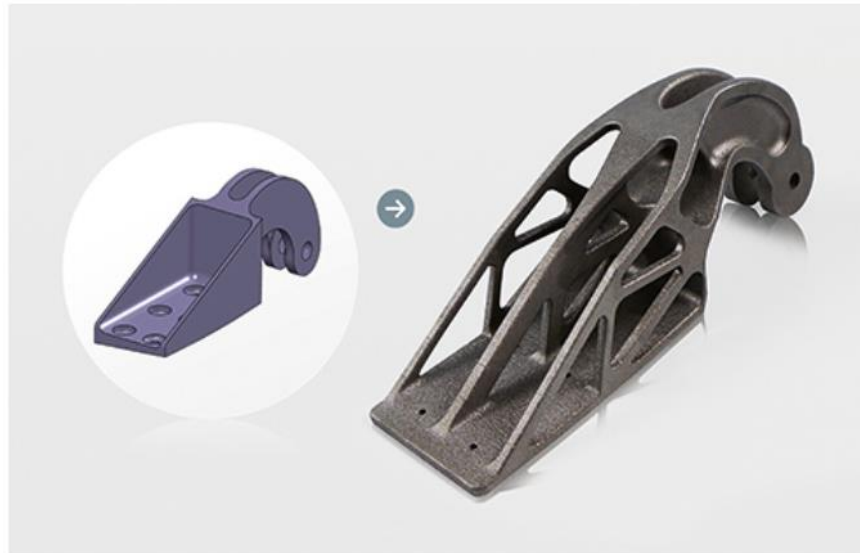


*Figure 4: Conventional steel cast bracket design (left), EOS Ti AM bracket (right). Source: EOS GmbH. [19]*

## 1.3 Biomedical Implants

In the past years, numerous medical devices have been designed to either replace, support or aid biological structures that function inefficiently. These type of products are developed from decade long studies in the biomedical engineering industry and are known as implants. As the name suggests, they are inserted directly inside the human body. The primary function of an implant is to improve the quality of function for the people that use them. The types of biomedical implants are diverse. Depending upon their functionality, biomedical implants range from being bioactive as in coronary stents to containing electronics such as artificial pacemaker in the human heart [20]. Most common implant applications used today are artificial hips, heart pacemakers, breast implants, spine screws, rods and artificial discs, IUDs (Intra-Uterine Devices), metal screws, pins, plates and rods, artificial knees, drug-eluting stents, ear tubes, artificial eye lenses etc [21]. *Figure 5* shows

an example of a biomedical implant (stent) used in a procedure called angioplasty, which includes the insertion of tiny expandable mesh tubes usually made out of medical-grade stainless steel or cobalt alloy metal in the blocked arteries [22].
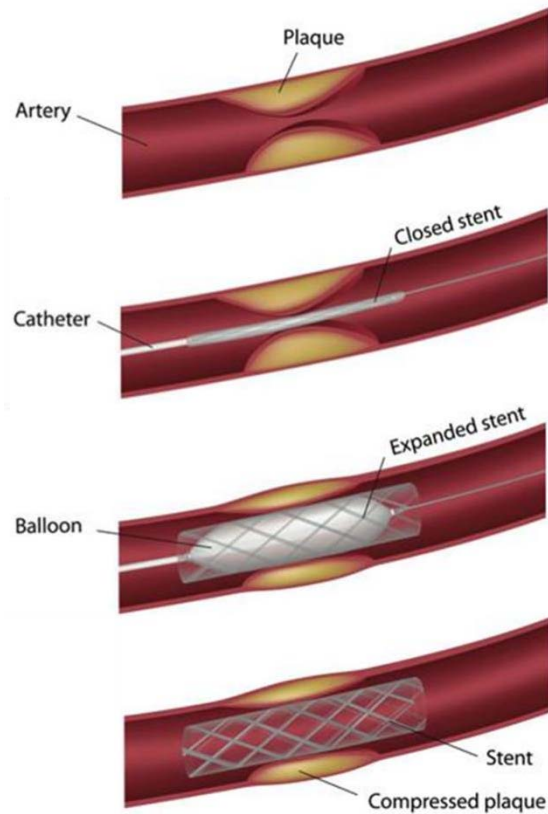


*Figure 5: Application of stent to allow free flow of blood in a plaque region of an artery [22]*

While there is abundant information on every implant types, the focus of this literature study lies on Total Joint Replacements (TJRs). TJRs are surgical procedures that involve removal and replacement of parts of an arthritic or infectious joint. The replacement is generally made of a metal, plastic or ceramic material and is termed as a prosthesis. The main goal of these prosthesis are to replicate the movement of a normal, healthy fully functioning joint. In the past decades, the total number of total joint replacement surgeries has been increasing at an alarming rate. Reported in 2011, almost 1 million total joint replacements were performed in the United States alone, every year this figure is climbing

rapidly [23]. The most common joint replacements are hip and knee replacements, but replacement surgeries are performed on joints such as ankle, wrist, shoulder and elbow.

### 1.3.1 Total Hip Replacement (THR)

One of the many applications of additive manufacturing is for biomedical implants. More specifically, using additive manufacturing to enhance joints used in total joint replacement surgery is an ongoing topic of interest. The most common purpose for a TJR is due to the wear of the articular cartilage, which is called osteoarthritis. The restoration of hip joints have been endeavored as early as the 1800's. However, the methodology used currently was said to first be described by Sir John Charnley in the 1960's [24]. *Figure 6* depicts the major components in a modular total hip joint replacement (THR) system.
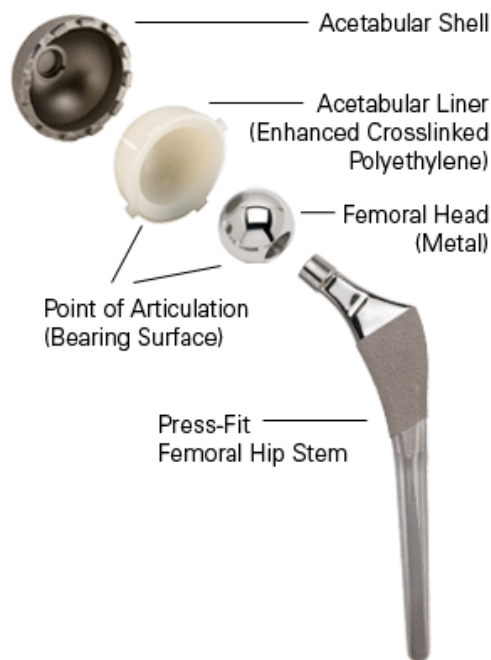


*Figure 6: Major components of a Total Hip Joint
Replacement Modular Design [34]*

For a total hip joint replacement, the components include the femoral head, femoral neck, acetabular liner, and acetabular shell. The acetabular shell fits inside the hip bone,

where the acetabular liner shares the interfaces of the shell and the femoral head. The femoral neck then connects to both the femoral head and the femur bone, and is typically made out of the cobalt, chromium, or ceramic. In addition, the acetabular liner and shell can consist of the same metals, ceramic, and polyethylene. Problems that have been associated with THR involve the loosening or dislocation of the femoral head, the wear of the polyethylene liner, the disintegration of bone tissue (osteolysis), and the tissue irritation due to metal debris from corrosion in the body. These issues commonly result in infections and discomfort for the patient, thus, requiring additional surgery. Additional surgeries after the first THR happens to a high percentage of recipients within 15 years [23]. However, improvements in technology has allowed for research to be done on the enhancement of the hip components, while focusing on the bearing surfaces and biocompatibility of the parts.

## 1.3.2 Biomedical Application of Additive Manufacturing

From early 2000s, AM has been applied in the field of medicine to make custom prosthetics and dental implants [25]. Since AM technology enables the fabrication of customizable products, AM has predominantly found its use in the production of customizable surgical implants and assistive devices for improved heath of general people. 3D-CAD solid models can be generated from computer tomography scan of the patient data and selective AM methods with selected material based on the patient's condition can be used to develop custom biomedical implants via reverse engineering [17]. It has been shown that RP and reverse engineering are effective methods for fabricating very accurate well-functioning implants [26]. Another study mentions RP significantly reduces the design cycle and part production time for customizable implants [27]. The most appealing

feature that attracts the use of AM in biomedical sector is the utilization of medical imaging data in the form of CT or MRI directly for the production of custom implants [28].

Clinical applications of AM could be seen in the form of biomodelling (fabrication of tangible models of human body for surgical planning and testing), design and fabrication of customized implants for prosthetic operations, rehabilitation and plastic surgery, fabrication of porous implants (scaffolds) and tissue engineering, fabrication of specific surgical aids and tools, drug delivery and micron-scale medical devices [28]. Various applications of AM technology in fabrication of biomedical implants include dentistry, hip-joints [28, 29], knee joints [30], parts of skull [26, 27], elbow [31].

However, as appealing as the use can be, several limiting factors of AM include: time and cost, accuracy of RP systems, poor or inaccurate medical imaging data, issues of materials (properties such as flexibility, strength and biocompatibility) [28].

### 1.3.3 Titanium and Its Alloy for Biomedical Applications

The following description of Titanium and its alloys are derived from excerpts from Donache *et al.* [32]. Titanium and its alloys are extensively used in the field of aerospace industry such as components of an aircraft system (aero-engines), space shuttles and sports industry particularly because of the greater strength to weight ratio. Due to its excellent biocompatibility nature, this metal is greatly used in the field of medical industry. Other application fields include chemical, petrochemical and marine environments. Titanium allows superior resistance to corrosion hence its widespread use in the aforementioned industries. Because of its low thermal conductivity, titanium and its alloys are somewhat complicated to process through traditional methods such as milling and turning.

The most common type of the titanium alloy used is (α+ß) alloy, namely, Ti6Al4V. with 6 % wt. aluminum stabilizing the α-phase and 4 % wt. stabilizing the ß-phase. The two-phase material comprises of hexagonal closed pack structure (HCP) of α-phase and body centered cubic (BCC) ß-phase. The transition temperature between the two phase is reported to be 995°C. Various microstructures are developed depending on the cooling rate and prior heat treatment performed. Characteristics microstructures include grain boundary allotriomorph-α, globular or primary-α, Widmanstatten, basketweave, and martensitic.

The mechanical properties of the (α+ß)-Ti6Al4V alloy are dependent on the distribution of the two phases throughout the material and the microstructure. The mechanical properties of wrought Ti6Al4V for surgical applications as standardized by ASTM 1472 are summarized in the *Table 1* below [33].

*Table 1: Mechanical Properties of wrought Ti-6Al-4V*

| Mechanical Properties | |
|---|---|
| Tensile Strength (MPa) | 930 |
| Yield Strength (MPa) | 860 |
| Elongation (%) | 10 |

For an α-ß alloy, the composition permits complete transformation to ß on heating but transforms back to α plus retained and/or transformed ß at lower temperature. It consists of one or more α-stabilizers plus one or more ß-stabilizers. As seen in *Figure 7 (a)* from the pseudo phase diagram of Ti64 alloy, alloying elements that are α-stabilizers such as Aluminum (Al), Oxygen (O) and Nitrogen (N), increase the temperature at which the α-phase is stable whereas elements that are ß-stabilizers such as Vanadium (V) and Molybdenum (Mo), result in the stability of the ß-phase at lower temperatures. The transformation temperature from (α+ß) or α to all ß is known as the *ß-transus temperature*.

It is also defined as the lowest equilibrium temperature at which the material is 100 % ß. The ß-transus is important for the fact that processing and heat treatment often are carried out with reference to some incremental temperature above or below the ß-transus. By moving away from the α-solvus phase boundary, the alloys form significant beta phase when heated. When there is sufficient amount of ß-formers, it is relatively easier to exceed the beta transus by heating. Also, the transformation of lower-temperature alpha to higher temperature beta phase which takes place by heating α+ß alloy is complete if the heating temperature goes above ß-transus. The formation of ß permits α+ß alloys to be strengthened by solution treating (exceeding the ß-transus or at least producing significant ß-phase for subsequent transformation) and aging (heating to produce further change in the transformed ß-martensites, acicular α- and the retained ß).
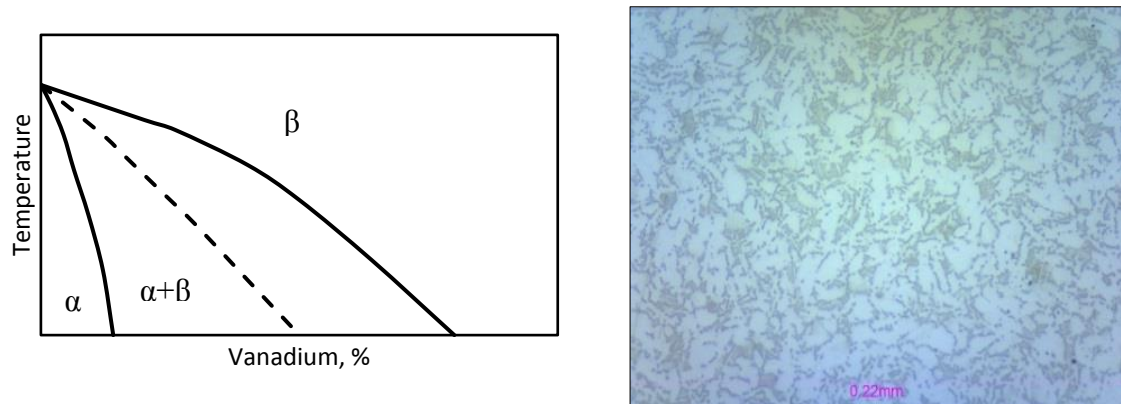


*Figure 7: (a) Pseudo phase diagram for Ti-alloys (b) Mill-annealed Ti6Al4V showing equiaxed microstructure*

Hence, a wide variety of microstructure can be produced by altering the thermomechanical process parameters. It is understood that ß formed at higher temperatures that are cooled to α and martensite variants are often referred in the literature as *transformed ß*. To place the alloy in a soft, relatively machinable condition, the alloy is heated to about 730°C in the lower range of the (α+ß) region, held there for 4 hours, then

furnace cooled to 25° C. This treatment is called mill-annealing which produces a microstructure of globular crystals of ß in an α-matrix as seen in *Figure 7 (b)*.

## 1.4 Research Objectives

As discussed in the previous section, improvement in the fracture and fatigue property of the implant material would be beneficial for patients that have to undergo revision surgeries. Particularly to solve these issue materials with better mechanical properties and functionality needs to be developed such that the major problem of wear and corrosion limiting the useful life of the implants would be resolved.

Direct digital manufacturing (DDM) is the process of making a physical part directly from a computer aided design (CAD) package model. Recently, it has gained its fame in the biomedical implant manufacturing because of the appealing features such as faster design to part production ratio, lower material consumption and rapid manufacturing. The range of customization provided by the DDM allows optimum anatomical restoration in the case of total joint replacements.

Anisotropy as opposed to isotropy, is defined as the property of being directionally dependent, meaning, the properties vary in different directions. The directional solidification of the additively manufacturing technique will result in the development of anisotropic characteristics within the part. Due to this construction, the implants manufactured via DDM, will result in a tribological behavior that might be superior as compared to the conventionally manufactured implant materials. This serves as a vital motivation for this research.

The primary objective of this research is to study the wear behavior of the additively manufactured electron beam melted Ti6Al4V-alloy in ambient and simulated biological

environments and compare it with the traditionally manufactured counterpart material. Additionally, the aim is to relate the observed wear response to the microstructure, anisotropy and mechanical properties of the material.

## 1.5 Thesis Outline

This thesis contains six chapters. Chapter 1 presents an introduction and background to the overall research. Section 1.1 briefly discusses the background of the research. Section 1.2 provides an introduction of additive manufacturing, its categories, advantages and disadvantages along with its applications followed by an overview of electron beam melting process. Section 1.3 provides a general overview of Biomedical Implants, Total Hip Replacements and a concise description of the biomedical material Titanium. Research Objectives are highlighted in Section 1.4 while Thesis Outline is provided in this section.

Chapter 2 presents the detailed discussion about the methodology used for this study. Various analytical methods used to characterize the mechanical properties, quantification of the wear volume and inspection of the wear phenomenon are presented.

Chapter 3 through Chapter 5 presents the majority of the study conducted for the overall research in either published paper format or a manuscript format. Each individual chapter includes an introduction, methodology, results and discussion followed by conclusion provided on specific topic of interest.

Finally, the conclusions drawn from the overall research are presented in Chapter 6 with recommendations for further future work.

## 1.6 References

1. Levy, G. N., Schindel, R., & Kruth, J. P. (2003). Rapid manufacturing and rapid tooling with layer manufacturing (LM) technologies, state of the art and future perspectives. *CIRP Annals-Manufacturing Technology*, *52*(2), 589-609.

2. Standard, A. S. T. M. (2012). F2792. 2012. Standard Terminology for Additive Manufacturing Technologies. *West Conshohocken, PA: ASTM International. See www. astm. org.(doi: 10.1520/F2792-12)*.

3. Gibson, I., Rosen, D. W., & Stucker, B. Additive Manufacturing Technologies Rapid Prototyping to Direct Digital Manufacturing. 2010.

4. ArcamAB. *Arcam History*. Date accessed 4/09/2017; Available from: http://www.arcam.com/company/about-arcam/history/

5. ASM International. Date accessed 4/09/2017; Available from: http://www.asminternational.org/documents/10192/1882071/amp16503p045.pdf/ d03429d3-895c-4403-8f84-ec33f3a9d172/AMP16503P045

6. Murr, L. E., Gaytan, S. M., Ramirez, D. A., Martinez, E., Hernandez, J., Amato, K. N., ... & Wicker, R. B. (2012). Metal fabrication by additive manufacturing using laser and electron beam melting technologies. *Journal of Materials Science & Technology*, *28*(1), 1-14.

7. Cormier, D., Harrysson, O., & West, H. (2004). Characterization of H13 steel produced via electron beam melting. *Rapid Prototyping Journal*, *10*(1), 35-41.

8. NCSU. Web Page. Date accessed 4/09/2017; Available from: https://camal.ncsu.edu/ebm-produced-copper-aluminum-network-structures/

9.  ArcamAB. Web Page. Date accessed 4/09/2017; Available from: www.arcam.com/solutions/creating-value-additive-manufacturing/

10. Safdar, A. (2010). Microstructures and surface roughness of EBM produced Ti-6Al-4V. Solid Mechanics, Lund University.

11. Kruth, J. P., Leu, M. C., & Nakagawa, T. (1998). Progress in additive manufacturing and rapid prototyping. *CIRP Annals-Manufacturing Technology*, *47*(2), 525-540.

12. Mathewson, B. B., Hebbart, R., Choitt, S., Newmant, W. S., Cawleyttt, J. D., & Heuerttt, A. H. (1998, January). Machine design, control and performance of automated computer-aided manufacturing of laminated engineering materials. In *Proceedings of the Solid Freeform Fabrication Symposium* (pp. 335-342).

13. Guessasma, S., Zhang, W., Zhu, J., Belhabib, S., & Nouri, H. (2015). Challenges of additive manufacturing technologies from an optimisation perspective. *International Journal for Simulation and Multidisciplinary Design Optimization*, *6*, A9.

14. Mahamood, R. M., Akinlabi, E. T., Shukla, M., & Pityana, S. (2014). Revolutionary Additive Manufacturing: An Overview. Lasers in Engineering (Old City Publishing), 27.

15. Ivanova, O., Williams, C., & Campbell, T. (2013). Additive manufacturing (AM) and nanotechnology: promises and challenges. Rapid Prototyping Journal, 19(5), 353-364.

16. Murr, L. E., Esquivel, E. V., Quinones, S. A., Gaytan, S. M., Lopez, M. I., Martinez, E. Y., ... & Stafford, S. W. (2009). Microstructures and mechanical properties of

electron beam-rapid manufactured Ti–6Al–4V biomedical prototypes compared to wrought Ti–6Al–4V. *Materials characterization*, *60*(2), 96-105.

17. Huang, S. H., Liu, P., Mokasdar, A., & Hou, L. (2013). Additive manufacturing and its societal impact: a literature review. *The International Journal of Advanced Manufacturing Technology*, 1-13.

18. Web Page. Dated accessed 2/6/2017; Available from: http://www.spilasers.com/whitepapers/practical-applications-and-uses-for-additive-manufacturing/

19. EOS. Date accessed 2/09/2017; Available from: http://www.eos.info/eos_airbusgroupinnovationteam_aerospace_sustainability_study.

20. Web Page. Date accessed 2/20,2017; Available from: https://en.wikipedia.org/wiki/Implant_(medicine)#cite_note-FDAClassDB-2

21. Web Page. Date accessed 2/21/2017; Available from: http://www.medical-directions.com/10-most-common-medical-implants-and-info/

22. Web Page. Date accessed 2/21/2017; Available from: http://www.secondscount.org/treatments/treatments-detail-2/heart-stents-tools-treating-blocked-blood-vessels-2

23. Popovich, A., Sufiiarov, V., Polozov, I., Borisov, E., & Masaylo, D. (2016). Producing hip implants of titanium alloys by additive manufacturing. *International Journal of Bioprinting*, *2*(2).

24. Ashman, B., Cruikshank, D., & Moran, M. (2016). Total hip replacement: Relieving pain and restoring function. *British Columbia Medical Journal*, *58*(9).

25. Cui, X., Boland, T., D D'Lima, D., & K Lotz, M. (2012). Thermal inkjet printing in tissue engineering and regenerative medicine. *Recent patents on drug delivery & formulation*, *6*(2), 149-155.

26. Singare, S., Dichen, L., Bingheng, L., Yanpu, L., Zhenyu, G., & Yaxiong, L. (2004). Design and fabrication of custom mandible titanium tray based on rapid prototyping. *Medical engineering & physics*, *26*(8), 671-676.

27. He, Y., Ye, M., & Wang, C. (2006). A method in the design and fabrication of exact-fit customized implant based on sectional medical images and rapid prototyping technology. *The International Journal of Advanced Manufacturing Technology*, *28*(5), 504-508.

28. Giannatsis, J., & Dedoussis, V. (2009). Additive fabrication technologies applied to medicine and health care: a review. *The International Journal of Advanced Manufacturing Technology*, *40*(1), 116-127.

29. Popov, I., & Onuh, S. O. (2009). Reverse engineering of pelvic bone for hip joint replacement. *Journal of medical engineering & technology*, *33*(6), 454-459.

30. He, J., Li, D., Lu, B., Wang, Z., & Zhang, T. (2006). Custom fabrication of a composite hemi-knee joint based on rapid prototyping. *Rapid prototyping journal*, *12*(4), 198-205.

31. Truscott, M., De Beer, D., Vicatos, G., Hosking, K., Barnard, L., Booysen, G., & Ian Campbell, R. (2007). Using RP to promote collaborative design of customised medical implants. *Rapid Prototyping Journal*, *13*(2), 107-114.

32. Donachie, M. J. (2000). *Titanium: a technical guide*. ASM international.

33. Standard, A. S. T. M. (2002). F136-02a: Standard specification for wrought titanium-6 aluminum-4 vanadium ELI (extra low interstitial) alloy for surgical implant applications (UNS R56401). West Conshohocken, PA: ASTM International; 2002, DOI: 10.1520/F0136-02A.

34. Exactech. Web Page. Date accessed 2/20,2017; Available from: http://exactech.co.jp/patients-caregivers/joint-replacement-surgery/hip-replacement/components-hip-replacement

# Chapter 2: Materials and Methods

## 2.1 Sample Manufacturing

In all of the study, the sample and powder material used was Ti-6Al-4V alloy. For the EBM-built samples, standard, Arcam Ti6Al4V powder was used. The sample manufactured was a cube of dimension 15 x 15 x 15 mm$^3$. Standard printing parameter by Arcam was used to build the specimen with layer thickness of 50µm and powder fraction size of 45-106 µm in an Arcam Q10 model (Arcam, Mölndal, Sweden). Traditionally manufactured mill-annealed specimen was supplied in the form of a cylindrical rod 1 inch in diameter and 10 cm long by ATI Allvac Corp. (Monroe, North Carolina).

## 2.2 Material Characterizations

For the analysis of the samples, various characterization techniques were utilized. Since, the focus of this research was to analyze the wear response of the material in relation to the mechanical properties, microstructure, surface anisotropy, many of the techniques used are for characterizing the surface properties. A brief summary of the different techniques used for the study are presented below.

### 2.2.1 Nanoindentation Tests

The following description of the nanoindentation technique is information based on Fischer *et al.* [1] and Ramirez *et al.* [2]. Nanoindentation is based on the standard of instrumented indentation, ASTM E2546 and ISO 14577. The test uses an established method where an indenter tip of a known geometry is driven by applying an incremental load into a specific site of the material to be tested. Upon reaching a pre-set maximum value, the normal load is retracted until complete relaxation. A piezo actuator applies the load and a high sensitivity load cell measures the load in a controlled loop. Usually, a high

precision capacitive sensor measures the position of the indenter with respect to the sample surface in real time [1]. The nanoindentation test schematics is shown in *Figure 8.*

Nanoindentation techniques have been utilized effectively to determine indentation hardness, young's modulus of elasticity and yield strength of various specimen materials from their corresponding load-displacement measurements. In a conventional hardness test, the size of a residual plastic impression in the specimen is measured as a function of the indenter load, from which, the area of contact for a given indenter load is determined. However, in a nanoindentation test, the size of the residual impression is only a few microns and hence, it becomes very difficult to obtain a direct measure using optical techniques. In nanoindentation testing, the load is applied to the indenter and the depth of penetration beneath the specimen surface is measured. The geometry of the indenter is known which allows the size of the area of contact to be determined. The modulus of the specimen material also can be obtained via this procedure, which uses the "stiffness" of the contact, that is, the rate of change of load and depth [2].
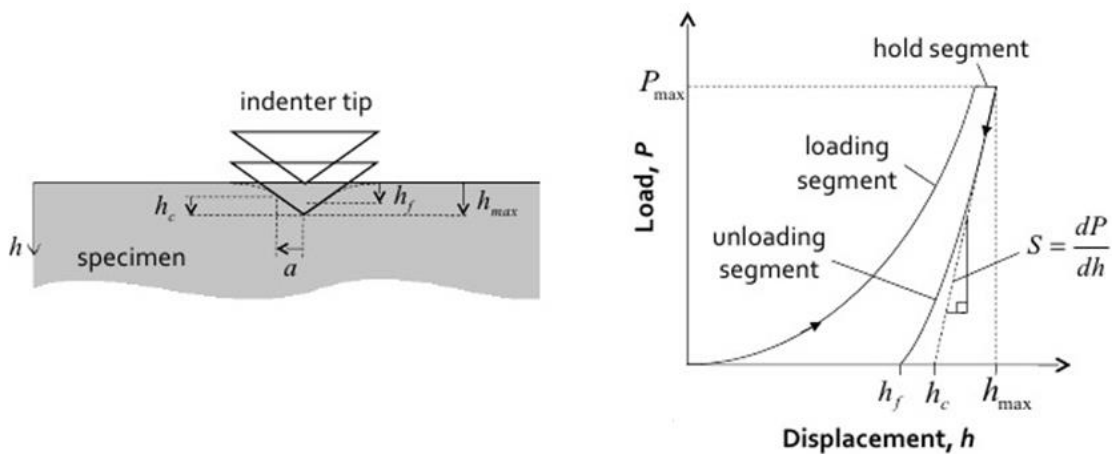


*Figure 8: Nanoindentation schematics (a) showing nanoindentation geometries and (b) typical load-displacement curve in an indentation test*

Usually in a typical test, force and depth of penetration are recorded during a cycle of loading and unloading with load applied from zero to some maximum and then from maximum force back to zero. The depth of penetration along with the known geometry of the indenter gives an indirect measure of the area of contact at maximum load, from which the mean contact pressure, and thus hardness, may be estimated. The material attempts to regain its original shape when the load is removed, but is prevented from doing so because of plastic deformation. However, the relaxation of elastic strains within the material allows some degree of recovery. The initial portion of this elastic unloading curve when analyzed, gives an estimate of the elastic modulus of the indented material. For the most common types of indenters, the compliance curves are very similar as shown in *Figure 9 (b)*.
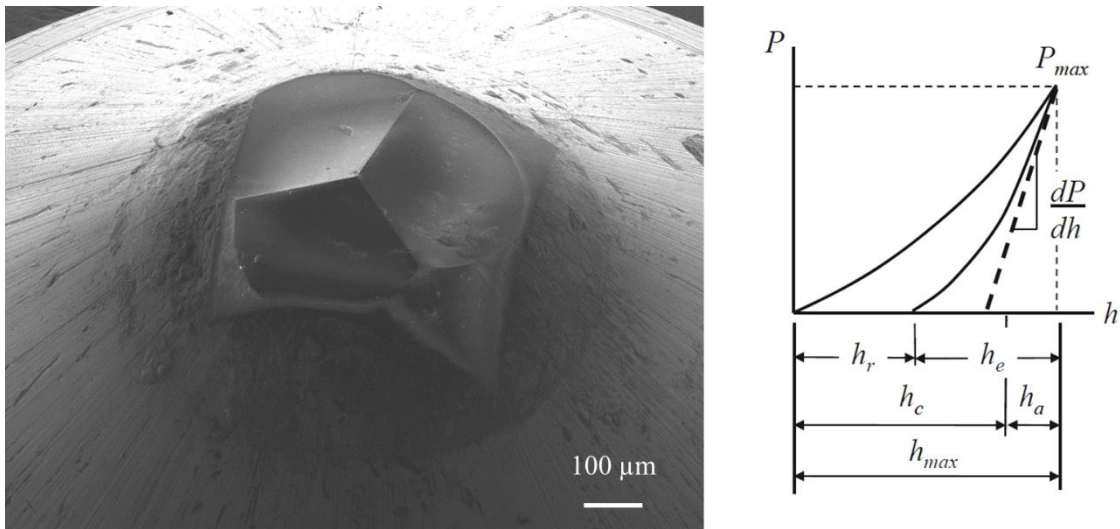


*Figure 9: Compliance curves, a typical Berkovich load-displacement curve, loading and unloading, from a nanoindentation experiment with maximum load $P_{max}$ and depth beneath the specimen free surface $h_{max}$. The depth of the contact circle hc and slope of the elastic unloading dP/dh allow specimen modulus and hardness to be calculated.*

The mean contact pressure of the contact is a meaningful quantity in indentation hardness, and is determined by dividing the indenter load by the projected area of the contact. The mean contact pressure, when determined under conditions of a fully developed plastic zone, is usually termed as the indentation hardness, $H$, of the specimen material.

$$H = \frac{P}{A} \tag{1}$$

where, $P$ is the applied load and $A$ is the projected area of contact.

In nanoindentation testing, the displacement of the indenter is measured and the size of the contact area (at full load) is estimated from the depth of penetration with the known geometry of the indenter. Berkovich indenter shown in *Figure 9 (a)* is a three-sided pyramid generally used in small-scale indentation studies. For Berkovich tip geometry, the projected area of contact, $A$, is dependent on the depth of contact circle $h_c$ (refer *Figure 9*) given by the relation [2]:

$$A = 3\sqrt{3}h_c \tan^2 \theta \tag{2}$$

For Berkovich, $\theta = 65.27°$, so,

$$A = 24.494h_c^2 \tan^2 \theta \approx 24.5h_c^2 \tag{3}$$

Hence, the mean contact pressure or hardness is:

$$H = \frac{P}{24.5h_c^2} \tag{4}$$

The indentation modulus is determined from the slope of the unloading curve at the maximum load as a function of $dP/dh$ given by:

$$E^* = \frac{1\sqrt{\pi}}{2\sqrt{A}} \frac{dP}{dh} \tag{5}$$

$$\frac{1}{E^*} = \frac{1-\upsilon^2}{E} + \frac{1-\upsilon_i^2}{E_i} \tag{6}$$

where, $E^*$ is the reduced elastic modulus, $E$ is the elastic modulus of the specimen and $E_i$ is the elastic modulus of the indenter material. Similarly, $v$ and $v_i$ are the poisson's ratio of the specimen and the indenter material.

The following description on determination of the yield strength via cylindrical flat punch indenter is based on Leroux *et al.* [3,4]. The stress at which a material starts to deform plastically and is no longer able to regain its original shape when the applied stress is removed is called Yield Strength. For practical applications, it indicates the upper limit to the load that can be applied to mechanical components, and is deemed crucial in materials production including annealing, forging, rolling and pressing.

Zhong Hu. *et al.* [5] has shown through micro-/nano-indentation testing, successful characterization of the elastic modulus and yield strength of the metallic materials. Usually, the yield strength characterization follows the same procedure as of the hardness test. However, the striking difference being, a cylindrical flat tip as shown in *Figure 10 (a)* and *(b)* with a known surface area is utilized as an indenter. A typical load-displacement curve for indentation with a cylindrical flat tip indenter is shown in *Figure 10 (c)*. The yielding part of the loading portion of the compliance curve is taken for the determination of the yield strength unlike the elastic unloading analysis done with a Berkovich indentation. The load applied during the test is well beyond the yield strength of the material. The first derivative infliction point, or a change from positive to negative of the second derivative, corresponds to the measured yield point as shown in *Figure 10 (d)*. Physically, as the load increases, the local roughness is squeezed, and the sample is squeezed down more slowly (because of the flat surface) as the depth increases. When the yield point is reached, the supporting load capacity of the material is surpassed and the flat tip starts penetrating at

increased speed. The point at which the slope of the compliance curve changes from increasing to decreasing indicates the onset of plastic deformation. The corresponding load at this point divided by the area of contact area of contact gives the yield strength of the material.

The yield strength of the sample is determined using the following equation:

$$\sigma_y = \frac{4P}{\pi d^2} \tag{7}$$

where, $\sigma_y$ is the yield strength, $P$ is the normal load applied and $d$ is the diameter of the indenter.
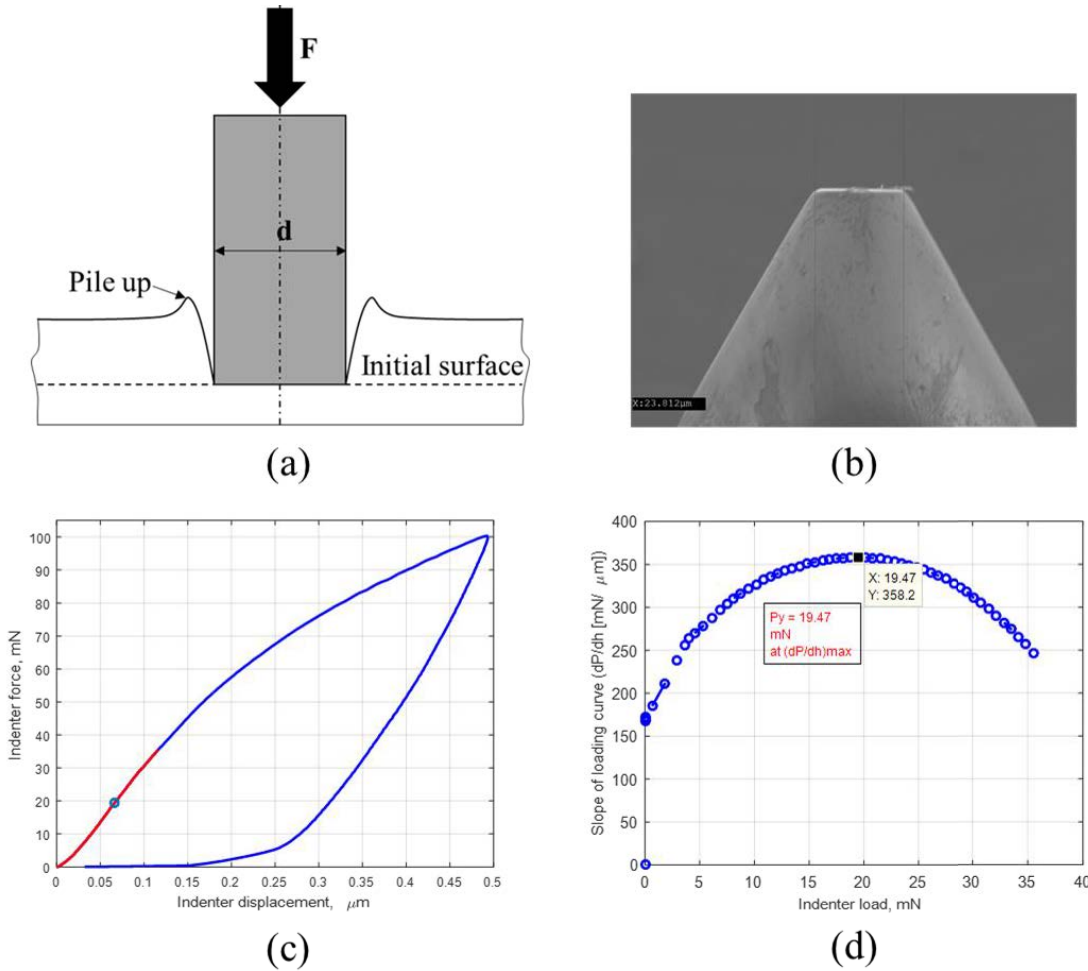


*Figure 10 (a) Schematic representation of indentation performed by a cylindrical flat-tip indenter (b) SEM image of a cylindrical flat-tip indenter taken at 1000x (c) a typical flat-tip indentation compliance curve and (d) point of infliction vs indenter load for the determination of yield point*

## 2.2.2 Surface morphology measurement

- Chromatic Confocal Technique (White Light Interferometry)

The non-contact chromatic confocal technique as shown schematically in *Figure 11 (a)* uses white light source that passes through the objective lens with very high degree of chromatic aberration. Since the light from the surface hitting the objective lens will have varying wavelength, the refractive index of the objective lens will vary accordingly. Each individual incident white light will refocus at different height. With a given resolution of the lens, a single monochromatic point will be focalized to form the image. The confocal configuration of the system allows only the focused wavelength to pass through the spatial filter and all other wavelengths will be out of focus. Thus, in this technique, all wavelengths intercepting the line of CCD will be liminated and only ones that aline with CCD will indicate the position of the maximum intensity, which directly corresponds to the z-height distance [6]. A 3D representation of a commercially pure 1mm dia. worn counter face spherical indenter surface mapped by this method is shown in *Figure 11 (b)*. The surface morphology for all of the wear tests were obtained using this technique.
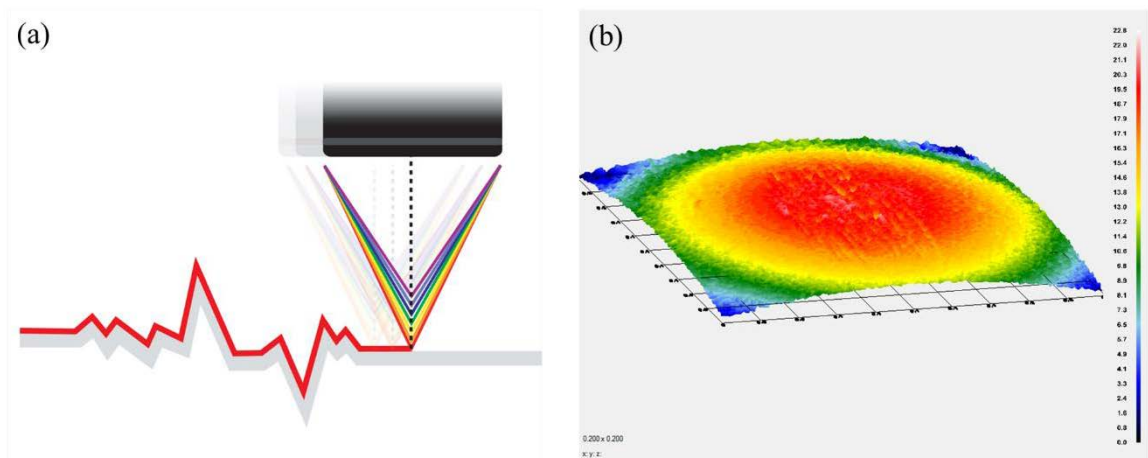


*Figure 11(a) Chromatic confocal technique [6] (b) Representative CCT 3D generation of a counterface material*

- Scanning Electron Microscope (SEM)

The scanning electron microscope (SEM) is a type of an electron microscope that produces microscopic images of a sample by scanning it with a focused beam of an electron. The process is similar to that of the EBM discussed earlier in Chapter 1 section 1.5. An electron gun present at the top of the column comprising a filament or a sharp tip produces a cloud of electron beam either by thermal emission or by field emission. The high-energy electrons (1 to 30 keV) are accelerated down towards the chamber and passes through a combination of lenses and apertures producing a very fine sized focused beam (of the order of nanometers) that hits the sample surface. Usually, both the column as well as the chamber are well maintained at vacuum via a combination of pumps.

Upon interaction of the electron beam to the sample, a number of signals are generated. For general usage to obtain the surface morphology the secondary electrons (SEs) emitted from roughly few microns below the samples surface are detected by a secondary electron detector and based on the intensity of the reflected electrons, information about the surface topography is obtained. The depth of penetration is dependent on the accelerating voltage and density of the sample.

Another type of signal generated when the electron interacts the specimen are the backscattered electrons (BSEs). In contrast to the SEs, BSEs are due to the scattering of the primary electron beam. The number of the BSEs and thus the intensity, increases as the atomic number of the element increases. Due to this reason, BSE images provide information about the different atomic species in the sample based on the brightness of the image.

Both SEs and BSEs mode were utilized to obtain the microstructures, grain morphology and wear morphologies in this study. Also, SEM was utilized to obtain the indenter tip images.

## 2.2.3 Surface Chemical Analysis

- Energy-dispersive X-Ray Spectroscopy (EDX)

Characteristic X-rays that are emitted from deeper zone of the interaction volume, allow the user to obtain quantitative and qualitative information regarding the chemical and elemental composition of the sample. When an electron beam hits the sample, the atom within the inner shell at its ground state is ejected resulting in an electron hole in the shell. Correspondingly, to fill up the hole, the electron from a higher-energy shell jumps on to the lower energy shell thereby releasing energy equal to the difference between the higher energy shell and lower energy shell in the form of an X-ray. An energy-dispersive spectrometer measures the number and energy of the X-rays emitted from the specimen. Each individual element will have characteristic atomic structure and the energy level where the shells sit, the energies of the X-rays obtained thus via EDS allows the elemental composition of the specimen to be measured.

EDX was used for the identification of the α and ß-phase elements and to quantify their chemical composition.

- X-Ray Diffraction (XRD)

XRD is a widely used analytical technique that uses x-rays that strike on a single crystal and produces scattered beams. A detector detects the scattered diffraction patterns from which information regarding crystal structure, lattice parameters, phase identification and information about unit cell can be obtained. XRD was utilized to obtain the phases present in the EBM-build Ti6Al4V specimens.

## 2.3 References

1. Ramirez, J.; Cyclical Nanoindentation Stress-strain measurement. Web Page. Date accessed 4/09/2017; Available from: http://nanovea.com/App-Notes/nanostressstrain.pdf

2. Fischer-Cripps, A. C. (2011). Nanoindentation testing. In *Nanoindentation* (pp. 21-37). Springer New York.

3. Li, D; Leroux, P; Yield & Tensile Strength of Steel & Aluminum using MicroIndentation. Web Page. Date accessed 4/09/2017; Available from: http://nanovea.com/App-Notes/nanostressstrain.pdf

4. Leroux, P. (2011). An indentation test that measures yield strength. *Advanced Materials and Processes*, *169*(10), 34.

5. Hu, Z., Lynne, K., & Delfanian, F. (2015). Characterization of materials' elasticity and yield strength through micro-/nano-indentation testing with a cylindrical flat-tip indenter. *Journal of Materials Research*, *30*(04), 578-591.

6. Nanovea Profilometers Brochure. Web Page. Date accessed 4/10/2017; Available from: http://nanovea.com/wp-content/themes/wp-nanovea/brochures/profilers.pdf

# Chapter 3: Experimental Investigation of Micro-scale Contact Fatigue Wear damage on EBM-built Ti6Al4V surface

S. Shrestha, J. Ryu and GP. Manogharan
Department of Mechanical and Industrial Engineering, Youngstown State University, Youngstown, OH, 44555

## Abstract

Superior tribo-corrosion resistivity of titanium alloys has drawn attention from biomedical industries. Design freedom of additive manufacturing (AM) technology has been a major advantage for custom biomedical implants. Therefore, additively manufactured Ti6Al4V joint implants would be a desirable solution for optimum orthopedic replacements. In this study, surface fatigue behavior of AM made Ti6Al4V is investigated to understand the correlations between process-induced anisotropic properties and fatigue wear resistance. Repeated single asperity sliding contact experiment is employed to simulate contact fatigue motions. Wear damage rate and roughness evolution are monitored as a function of mechanical stimuli and additive layer orientations. Results are compared with traditional (mill-annealed) Ti6Al4V surface. This newer understanding of fatigue wear mechanism on AM made implants will promote the extensive biomedical application of AM technology by identifying optimal build orientations.

**Keywords**: Additive manufacturing, nanoindentation, surface contact fatigue, biomedical implants

## 3.1 Introduction

Direct digital manufacturing is the process of making a physical product directly from CAD (Computer Aided Design) data. Direct digital manufacturing technologies have rapidly evolved over the past decade and are gaining applications in aerospace, functional components and biomedical implant manufacturing [1-2]. Some of the appealing features of direct digital manufacturing systems include; reduced part development time, lower or no process engineering time, lower material consumption and faster design-to-part production [3-4]. The layer by layer principle of additive manufacturing (AM) has been employed for a variety of materials including plastics, ceramics and metals. Several studies have classified and compared different AM processes [5-6]. More recently, the ability to directly manufacture metal components with complex part geometries without tooling (e.g. molds, dies or fixtures) has been a topic of great interest. The huge investment associated with tooling typically necessitates the production of medium to large batch sizes to reduce the unit cost of components and hence, traditional manufacturing methods are preferred for mass production. A study has highlighted the advantage of additive methods for production volume of one, when compared to conventional methods [7].

Wear and corrosion of orthopedic implants is a crucial issue and has been found to significantly limit the useful life of implants. Wear and fretting corrosion in the artificial joint result in the formation of soluble and particulate debris that can migrate in locally or systemically and may induce a cascade of inflammatory events that may ultimately result in bone loss by osteolysis and subsequent implant failure [8-9]. It can be clearly seen that enhancing the durability and reliability of total joint replacements (TJRs) is critical engineering problem that affects the society and economy. In spite of the widely

appreciated magnitude of this problem, there is a critical gap in the knowledge base that reveals the influence of AM induced microstructure on the wear and fretting corrosion of implants.

Fretting corrosion of modular implant material is a critical problem and often limits the service life of the implants. It results in metal degradation due to simultaneous action of mechanical loading and electrochemical oxidation. These two mechanisms do not occur independently, but are correlated in a complex way and are influenced by factors such as (a) elastic and plastic properties of the surfaces (b) contact pressure (c) roughness of the contact surfaces and (d) corrosive environment. The major questions that still exist are: 1) What is the mechanism for onset of material damage at the interface? 2) How can the onset of failure in the interfaces for a given set of materials and interface conditions be predicted? 3) How do the material properties, implant design and surface roughness affect these mechanisms and predictions? This lack of understanding severely limits the designers and manufacturers in their efforts to optimize current surface finishing operations in order to produce more durable and reliable total joint replacements.

There are numerous works which address the wear and corrosion of interfaces in total joint replacements (TJRs) [8-9]. In a modular TJR, the interface between metallic femoral head and polymeric acetabular insert undergoes progressive wear. However, the interface between femoral head and stem in modular joints undergoes mechanical-loading-assisted corrosion or fretting corrosion. Historically, wear in polymer-metal interface has been studied using a joint-simulator or a conventional tribological testing machine such as a reciprocating tribometer or pin-on-disk apparatus. Fretting corrosion response of the modular implants has been generally quantified through electrochemical measurements or

measurement of weight loss during exposure to chemical environment [10-11]. Laboratory wear tests, observations of the surfaces of clinically retrieved implants and analysis of wear particles suggest that wear occurs via the following four mechanisms: adhesive wear, abrasive wear, three-body wear, and surface fatigue wear. Although a number of studies on wear and fretting corrosion of interfaces in TJRs have been conducted, they have all almost exclusively focused on obtaining a rate of material damage in order to compare the performance of different implant materials. In terms of the effects of AM induced microstructure on damage mechanism, the effects of AM processing which finally governs wear and corrosion damage by correlating to its surface grain morphology and grain orientation has not been studied. Therefore, it is critical to identify the mechanisms of wear and corrosion, and identify an optimum grain structure resulting from layer-based AM which could inhibit the damage mechanism. The motivation for this study is to understand the single asperity surface damage characterization of medical grade AM surfaces (Ti6Al4V-grade 5) using Nanoindenter-based experimentation to determine the rate of surface damage based on manufacturing processes and process-induced microstructures.

## 3.2 Approach

### 3.2.1 Material Description

The materials used in this investigation are mill-annealed Ti6Al4V and additive manufactured Ti6Al4V in two different build orientations. A 25 mm diameter mill-annealed Ti6Al4V rod was cut into 2.5 mm thick disks using electrical discharge machining (EDM). Ti6Al4V powder (89.375% Ti, 6.36% Al, 3.96% V, 0.02% C, 0.22% Fe, 0.08% O, 0.01% N, 0.001% H, and 0.001% Y) was printed into 50.8 mm diameter disk using standard electron beam melting (EBM) print parameters (layer thickness of 50μm

with powder size distribution of 45-106μm) using Arcam Q10. Two groups of EBM specimens were fabricated along two different building orientations as shown in *Figure 12*. The EBM specimens were cut into four quadrant pieces using EDM. The surfaces were prepared through a series of polishing using SiC discs (grit counts: 180, 320, 1000 and 4000) with water, a 9 μm diamond suspension, and finally with a 0.06 μm colloidal silica suspension to achieve mirror finish. All the specimens indicated a center-line average (CLA, Ra) between 13.8nm to 17.5nm over 200μm cut-off distance. The specimens were etched in a solution of 100ml of distilled water ($H_2O$), 6ml of nitric acid ($HNO_3$), and 3mL of hydrogen fluoride (HF) to inspect the microstructures. Microstructure of mill-annealed Ti6Al4V exhibited a bimodal grain structures as shown in *Figure 12 (a)*. Vertically EBM-built (EBM-z) specimens showed lamellar microstructural features as in *Figure 12 (b)*. *Figure 12 (c)* illustrated a combined lamellar and equiaxed structures at the grain boundaries on laterally EBM-built (EBM-y) specimen surfaces. Mechanical properties of
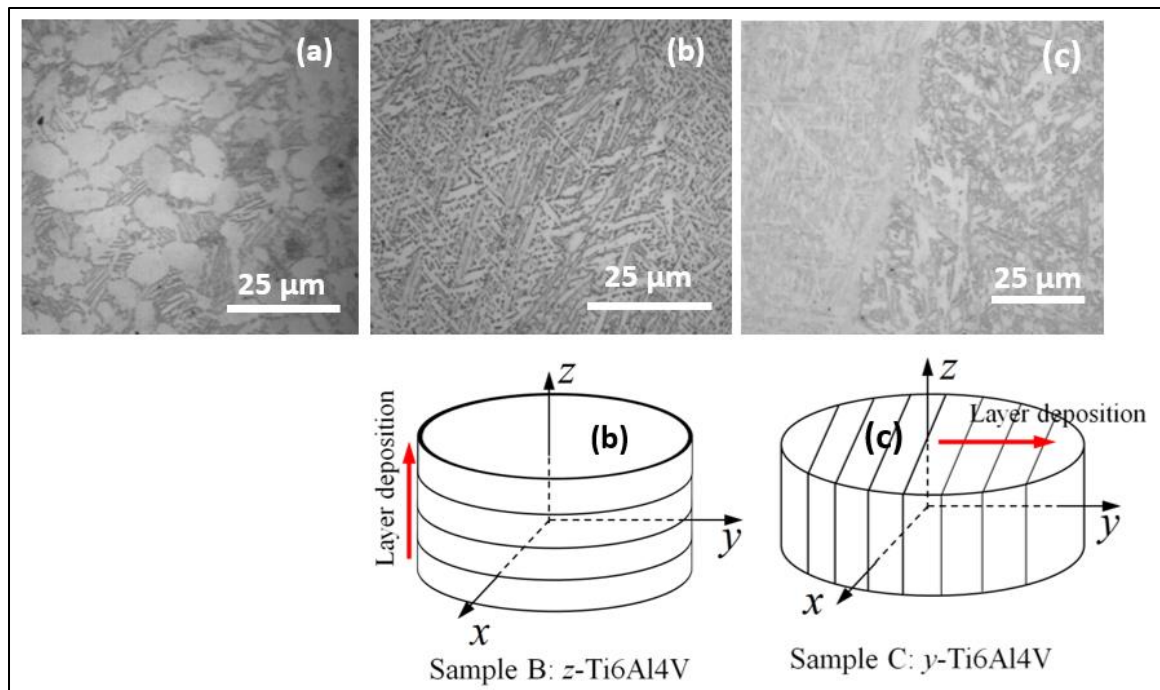


*Figure 12: Microstructures of mill-annealed Ti6Al4V specimen (a), vertically EBM-built (EBM-z) specimen (b), and laterally EBM-built (EBM-y) specimen (c)*

41

the specimen surfaces were measured using nano indentation technique. A standard Berkovich indenter was selected and force control scheme at the rate of 4.5 mN/sec up to a maximum load of 140 mN was performed during a full indentation cycle. The slope of load-depth curve at the maximum indentation load of 140 mN was evaluated during the unloading process to calculate elastic modulus (E, GPa) and indentation hardness (H, GPa). The specimens were subjected to 50% of nominal yield strength of each specimen in ambient conditions and controlled humidity (35±3%).

### 3.2.2 Contact Stress Estimation

In order to investigate the effects of manufacturing process on wear and friction resistance, it is necessary to compare material removal based on relative contact stress approximated from yield strength of the materials rather than the load. In order to analyze and facilitate comparison of wear response, Hertzian analysis was used to estimate the average contact pressure. The nominal maximum normal load to yield the titanium surface was estimated based on (1) measured mechanical properties of mill-annealed Ti6Al4V using nanoindentation technique, (2) published properties of EBM-produced Ti6Al4V, (3) silicon nitride indenter by the manufacturer and (4) measured tip radii of indenter head. In order to ensure the elastic range of the nominal contact load during the cyclic sliding contact test, 50% of the normal load that yields the surface was applied. The normal force and true indenter penetration was continuously monitored during the test in ambient conditions and controlled humidity (35 ± 3 %).

### 3.2.3 Surface Wear

A nanoindenter-based mechanical tester (Nanovea, Irvine, CA) was utilized for the single asperity fatigue contact experiment. The mechanical tester consists of a nanoindenter

and a high resolution step-motor motion stage. The nano-resolution (nN) load cell monitors precise normal loads and the piezoelectric feedback module measures the displacement responses. The high resolution motion stage accurately controls the horizontal motion of the specimen relative to vertical motion of the indenter tip. Silicon nitride ($Si_3N_4$) spherical indenter tips (Nanovea, Irvine, CA) were used in the present study.

Silicon nitride tip size was measured using an optical profilometer prior to each study
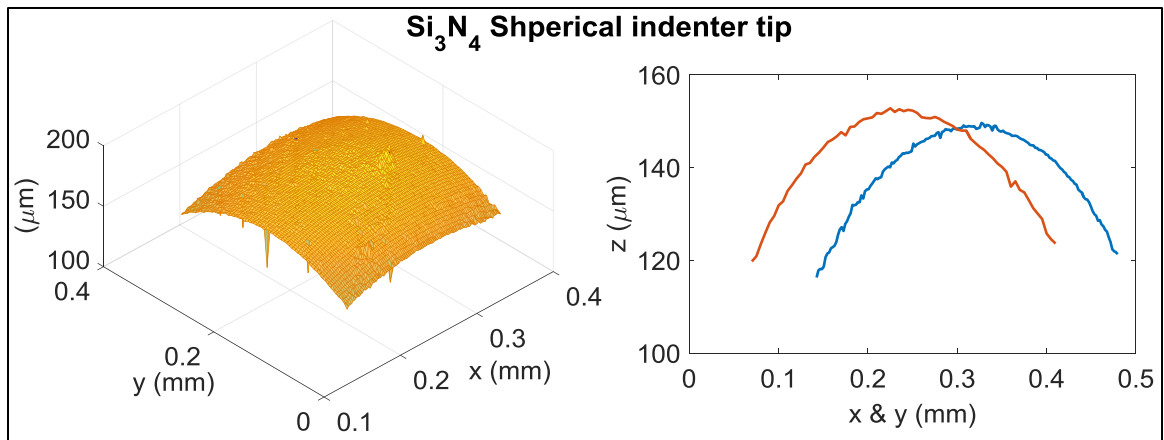


*Figure 13: Indenter tip characterization*

to ensure application of accurate contact stress as shown in *Figure 13*. Two principal axes of the tip radii were selected from the scanned profile and monitored after each contact test to ensure any negligible change in the indenter shape. Microscale raster-scanning motion of the indenter tip with constant normal load was applied in the rectangular area (200 µm x 40 µm) of the specimen surface. *Table 2* summarizes the nominal properties of the contact materials.

*Table 2: Mechanical Properties of contact surface materials*

|  | Mill-Annealed Ti6Al4V | Electron Beam Melting processed Ti6Al4V | $Si_3N_4$ AFM probe |
|---|---|---|---|
| Young's Modulus | 116 GPa | 117 GPa | 310 GPa |
| Poisson's Ratio | 0.35 | 0.35 | 0.27 |
| Yield Strength | 1047 MPa | 950 MPa | - |

Surface damage response was investigated on three different specimens: mill-annealed, vertically EBM-built, and laterally EBM-built Ti6Al4V. For each test, an initial 400 μm x 200 μm profilometric image of test area was recorded using an optical sensor (Nanovea, Irvine, CA) with 0.5 μm resolution prior to the wear test. Cyclic sliding contact was then preformed on an area of 200μm x 40μm at the center of the 400μm x 200μm scanned area. The tip was rastered across this area at 200μm/sec for 30 minutes at the desired contact force. Under this raster-scanning setup, each 200 μm-long sliding contact repeats approximately 300 times within the test area for 30 minutes. Final surface image was recorded using optical profilometer on the same initial surface, 400μm x 200μm. The fretting wear experiments were conducted at normal contact loads of 69.5mN on mill-annealed Ti6Al4V and 52.06mN on both EBM-built Ti6Al4V surfaces. The surface damage of indenter tips was also monitored to capture any minor changes in contact stresses during continuous sliding motions.

## 3.2.4 Post-Processing

Surface damage was calculated based on material removed from 200μm x 40μm area during the experiment using optical profilometer images before and after fatigue sliding contact. The specimen surface was mirror-polished but some undesired surface imperfections such as scratches or adhesive tear out pits from polishing still existed. In order to minimize the effects from such surface imperfections, the final profile data after contact damage experiment was subtracted from initial surface profile on the test site. This technique negates any unexpected effects due to initial surface topologies and precisely evaluates the wear volume by fretting contact as shown in *Figure 14*. Representative surface image of the damaged mill-annealed Ti6Al4V surface is shown in *Figure 14 (b).*
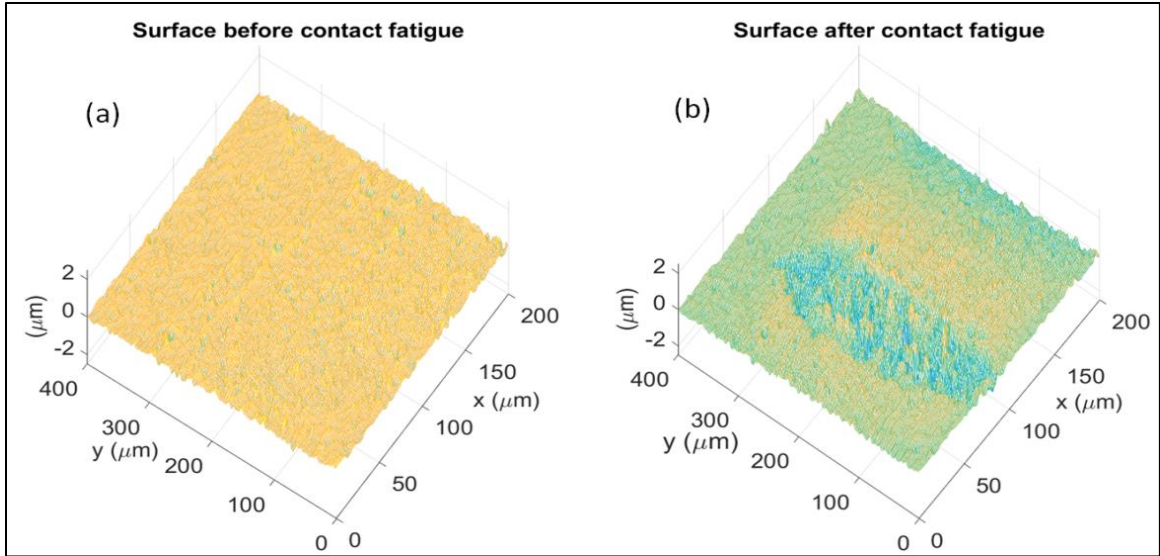
*Figure 14: Image processing to compute the wear volume after sliding contact*

## 3.3 Results and Discussion

Using nanoindenter-based single asperity contact experiments, wear depth of Ti6Al4V surfaces processed using three different processing conditions (mill-annealed, EBM-z, EBM-y) was obtained. The respective results were compared based on their fundamental mechanical properties such as elastic modulus and indentation hardness (*Figure 15*).
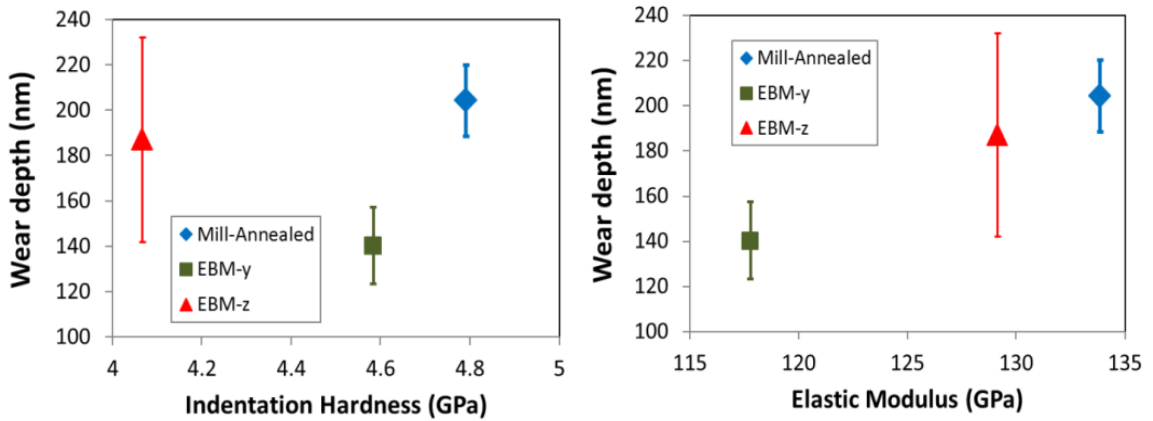


*Figure 15: Surface wear depths compared as a function of mechanical properties measured by nanoindentation*

The measured trench depths are plotted as a function of elastic modulus and indentation hardness values measured using nanoindentation technique. The standard deviation (shown

45

as error bars) is a result of large deviations in wear depth. As found in most contact wear phenomena, the material removal rate varied with different manufacturing process and orientation. It was observed that trench depth significantly increased in surfaces with lower indentation hardness. The mill-annealed samples showed the lowest wear rate while EBM produced specimens showed greater wear rate. Interestingly, laterally EBM-built samples (EBM-y) showed superior wear resistivity than vertically built samples (EBM-z). It was found that volume of material removed is a weak function of mechanical properties (indentation hardness and elastic modulus). Interestingly, superior mechanical properties of mill-annealed Ti6Al4V showed the highest rate of wear damage. This result implies that nominal values of mechanical properties may not dictate the nature of wear and friction resistivity of the surfaces. The process-induced microstructures characterized the anisotropic lamellar structure of the EBM-z surface that causes a larger variation of the wear depths. The result implies that the sliding direction and locally varying lamellae orientations would result in inconsistent wear behaviors based on test sites.

The surface amplitude change at the roughness modes was studied to identify the surface roughness evolution process during sliding contact. *Figure 16* presents the power spectrum after Fast Fourier Transform (FFT) computation which illustrates distinctive behaviors as roughness changes at specific spatial frequency (1/μm). The FFT spectrum successfully illustrates the correlations between wear rate and roughness evolutions. The mill-annealed surface presents greatest roughening (*Figure 16*) and greatest wear rate (*Figure 15*). Similarly, EBM-y surface showed the least roughening and least wear rate. The vertically built EBM surface (EBM-z) is subjected to uniform growth of roughness heights over broad roughness modes, while laterally built EBM surface (EBM-y) is

46

subjected to growth in roughness at long surface modes. Both mill-annealed and EBM-z surfaces undergo increase in roughness at all roughness height domain. However, a notable
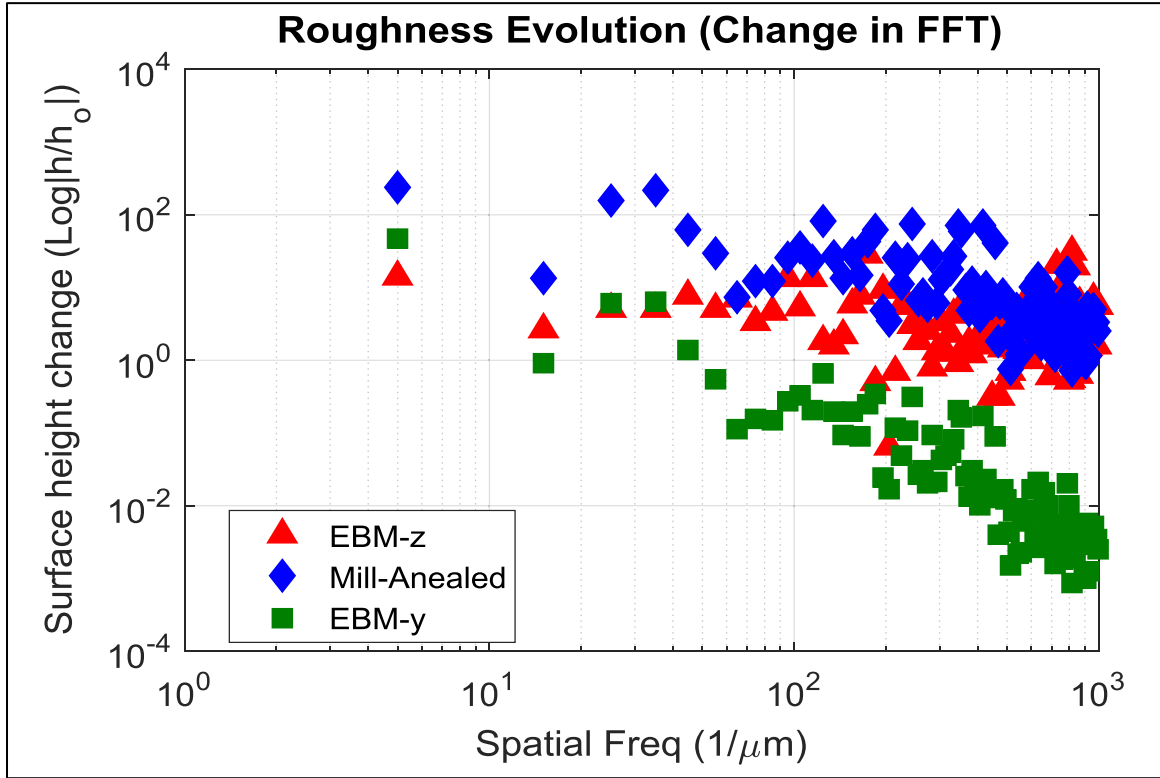


*Figure 16: Roughness evolution of three specimen surfaces represented by log(h/ho) , where h and ho are final and initial surface amplitudes, respectively*

flattening process (decrease in roughness) on EBM-y surface was observed at higher surface frequency domain.

## 3.4 Conclusion

The wear damage process of the surfaces developed by different manufacturing processes is a complicated mechanism that cannot be determined solely from microstructure or nominal mechanical characteristics. It must be elucidated by considering the combined effects of processing as well as resulting grain structures. This study presented the surface contact fatigue behavior of Ti6Al4V surfaces based on processing methods. The complex dependence of wear resistance on contact load, microstructure, and

stress suggests that wear mechanism varies with traditional and AM approach as well as AM orientation. In addition, as observed in EBM-y surfaces, lateral EBM building orientation would suggest a possible avenue to achieve superior tribological characteristics on the medical grade Ti6Al4V. A further study on residual stress and resulting wear mechanism is required (e.g. Laser AM with post-processing of annealing) to compare EBM and other metal AM processed Ti6Al4V surfaces.

## 3.5 References

1. Gibson, I., Rosen, D. and Stucker, B., 2010, "Chapter 14: Direct Digital Manufacturing", Additive manufacturing technologies, Springer, New York, U.S.

2. Frazier, W.E., 2010, "Direct Digital Manufacturing of Metallic Components: Vision and Roadman", 21td Solid Freeform Fabrication symposium, Austin, USA.

3. Chiu, W.K. and Yu, K.M., 2008, "Direct Digital Manufacturing of Three-Dimensional Functionally Graded Material Objects", Computer-Aided Design, Vol. 40 (12), pp. 1080-1093.

4. Czajkiewicz, Z.J., 2008, "Direct Digital Manufacturing, New Product Development and Production Technology", Economics and Organization of Enterprise, Vol. 2, pp. 29-37.

5. Yan. X and P. Gu., 1996, "A review of rapid prototyping technologies and systems", Computer Aided Design, Vol. 28 (4), pp. 307-318.

6. Pham, D. T. and Gault, R. S., 1998, "A comparison of rapid prototyping technologies", International Journal of Machine Tools and Manufacture, Vol. 38 (10-11), pp. 1257-1287.

7. Petrick I.J. and Simpson, T.W., 2013, "3D Printing Disrupts Manufacturing: How Economies of One Create New Rules of Competition", Research-Technology Management, Vol. 56(6), pp. 12-16.

8. Mosleh, M. and Suh, N.P. 1996, "Wear particles of polyethylene in biological systems", Tribology Transactions, Vol. 39, pp. 843 - 848.

9. Hirakawa, K. and Jacobs, J.J., Urban, R., and Saito, T., 2004, "Mechanisms of failure of total hip replacements - Lessons learned from retrieval studies", Clinical Orthopaedics and Related Research, Vol. 420, pp. 10 – 17.

10. Hallab, N.J., Messina, C., Skipor, A. and Jacobs, J.J., 2004, "Differences in the fretting corrosion of metal-metal and ceramic-metal modular junctions of total hip replacements", Journal of Orthopaedic Research, Vol. 22, pp. 250-259.

11. Mathew, M.T., Nagelli, G., Pourzal, R., Fischer, A., Laurent, M.P. and Wimmer, M.A., 2014, "Tribolayer formation in a metal-on-metal (MoM) hip joint: An electrochemical investigation", Journal of Mechanical Behavior of Biomedical Materials, Vol. 29, pp. 199-212.

# Chapter 4: Wear response of EBM built Ti6Al4V: combined effect from anisotropic surface grain and frictional motion

S. Shrestha, J. Ryu and GP. Manogharan
Department of Mechanical and Industrial Engineering, Youngstown State University, Youngstown, OH, 44555

## Abstract

Ti6Al4V is the most widely used implant material owing to its biocompatibility, superior tribo-corrosion resistivity and suitable mechanical properties. The freedom of design provided by AM provides advantage for the fabrication of custom biomedical implants. The current research is aimed at studying the wear response of Ti6Al4V joint implants manufactured via electron beam melting (EBM) in an effort to shed more light on the idea of using AM as a desirable solution for optimum orthopedic replacements in lieu of joint implants manufactured via conventional manufacturing methods. A comprehensive study of surface fatigue behavior in relation to the AM-induced anisotropy, microstructure, and mechanical properties in the dry sliding environment has been discussed. Repeated single asperity sliding contact experiments were conducted to simulate contact fatigue motions. Commercially pure Grade-2 Titanium-spheres of 1 mm in diameter were used as the counter-face material. The tests performed were varied in their sliding direction to investigate the effects of layer deposition on the EBM-built samples. Material characterization was done by instrumented indentation technique (IIT). The normal load corresponding to 25 % of the average yield strength of the material was used for the scratch test. The reciprocating scratch tests were conducted at a constant normal load of 37 mN

equaling to a Hertzian contact pressure of 318 MPa. The results obtained after quantifying the worn surface showed EBM-built material to have superior wear resistance as compared to the mill-annealed specimen. The effect of anisotropy on the material wear was seen significant. Furthermore, the variation in the wear volume with change in the sliding orientation was approximately 63 % and 88 % for vertically built EBM-X and horizontally built EBM-Z specimens, respectively.

## 4.1 Introduction

Titanium alloys specifically (Titanium, 6-Aluminium, 4-Vanadium) are the most commonly used material for biomedical applications namely because of its superior mechanical properties such as high strength to weight ratio, superior resistance to corrosion, better fatigue characteristics, biocompatibility. For these reasons, many of the applications can be seen in manufacturing surgical implants (dental, orthopedic) [1, 2]. The surface characteristics that affect biocompatibility are surface texture, steric hindrance, binding sites, and hydrophobicity (wetting) [3]. Over the years, researchers have considered improving the fracture and fatigue properties of these implant materials. The mechanical characteristics of these materials are directly dependent on the prevailing microstructure. Various manufacturing methods are employed to explore new avenues on processing these materials to obtain different microstructures thereby bringing superior and/or desirable properties. Traditionally, metal implants are manufactured mostly by casting the mold to the desired part and finishing the part by hot working and machining. The microstructure imparted onto the part is dependent on: i) the way the part solidifies as it cools down after casting, ii) strain rate during hot working and iii) heating because of machining [4]. Also, residual stresses in these parts causes the part to have inferior mechanical properties to begin with which require further heat treatment procedures to alleviate the resulted stresses. However, additive manufacturing (AM) is seen to have emerged as a new technology to produce functional parts directly from 3D CAD models. Materials processed include ceramics, plastics, metals, bio-tissue, etc [5]. Applications in biomedical implant manufacturing is a keen area primarily because of the custom designed manufacturing capability of the direct digital manufacturing technique. Specially because

almost in all cases the manufacturing of these implants are greatly dependent on patient specific data, hence, AM is proving to be an ideal solution to overcome the prevailing challenges in custom biomedical implant manufacturing [6].

Electron Beam Melting (EBM) is one of the powder-bed fusion metal AM process that is increasingly used to process Ti6Al4V. It has been discussed that EBM has higher energy-efficiency and prints metallic parts more rapidly as compared other similar laser-based systems. In addition, parts fabricated via EBM were shown to have less residual stress than parts fabricated via other metal-AM methods [7-9]. The study of the microstructure in relation to the mechanical properties of metal AM processes have been investigated in a number of reports [9-11]. However, the study of the effects of anisotropy, microstructure and mechanical properties with the wear and corrosion of Ti6Al4V has not been studied in detail. Ti6Al4V surfaces are known to have poor wear resistances in dry sliding environment due to low protecting tribo-oxides formed at its surface [12, 13]. Therefore, there is an urgent need to develop an understanding of the multifactorial mechanism of wear and corrosion and identify an optimum microstructure resulting from stepwise additive layering that inhibits the implant failure. With growing challenges in material selection and production and increasing demand of metal joint replacements, it is of utmost interest to explore the different material options and their manufacturing methods to find the optimum material. The present research aims at investigating the wear behavior of EBM-built Ti6Al4V parts built in different orientations and making a comparative study against commercial mill-annealed Ti6Al4V material.

## 4.2 Materials and Methods

### 4.2.1 Overview

Traditionally manufactured Ti6Al4V mill-annealed samples are procured. Using electron beam melting (EBM), Ti6Al4V samples are additive manufactured complying to ASTM standards. To analyze the effects of AM process-induced surface anisotropy, the samples are evaluated in two different orientations: horizontal (x-direction) and vertical (z-direction), referenced as EBM-X and EBM-Z throughout this article. Whereas, for mill-annealed samples, no particular orientation is considered because the process induces transversely isotropic surface properties. The experimental design for this study consists of determining the mechanical properties of each individual build material and using those properties to determine a Hertzian contact load to perform wear tests to inspect the tribological response of the materials under study. Nano-indentation tests are performed to determine the mechanical properties including modulus of elasticity, indentation hardness value and yield strength. A single wear test configuration or tribo-system (linearly reciprocating pin-on-flat) is employed to investigate the tribocorrosion effect on AM versus traditionally made Ti6Al4V alloy subjected to sliding against a 1mm dia. grade-2 Titanium (indenter) in dry ambient environment.

### 4.2.2 Materials and Preparation

The materials used in this study is Ti6Al4V-alloy manufactured by standard electron beam melting (EBM) using Arcam Q10 (Mölndal, Sweden) with layer thickness of 50 μm and powder size of approximately 45~106 μm and traditionally manufactured mill-annealed Ti6Al4V supplied by ATI Allvac Corp. (Monroe, North Carolina). The chemical composition of the alloy provided by the manufacturers are presented in *Table 3*.

*Table 3: Summary of Ti6Al4V Chemical Composition for EBM and Mill-annealed Ti6Al4V*

| Elements | Percentage weight composition (%) | | | | | | | |
|---|---|---|---|---|---|---|---|---|
| | Aluminum (Al) | Vanadium (V) | Carbon (C) | Iron (Fe) | Oxygen (O) | Nitrogen (N) | Hydrogen (H) | Titanium (Ti) |
| EBM | 6 | 4 | 0.03 | 0.1 | 0.15 | 0.01 | 0.0003 | Balance |
| Mill-annealed | 6.37 | 4.04 | 0.032 | 0.21 | 0.17 | 0.028 | n/a | Balance |

To investigate the process induced anisotropic properties of EBM manufactured Ti6Al4V, two sets of samples, are manufactured with different build orientations. As shown in *Figure 17*, square layers (15 mm x 15 mm) are built along Z direction of the build with the final product being a cube that has its sides of 15 mm.
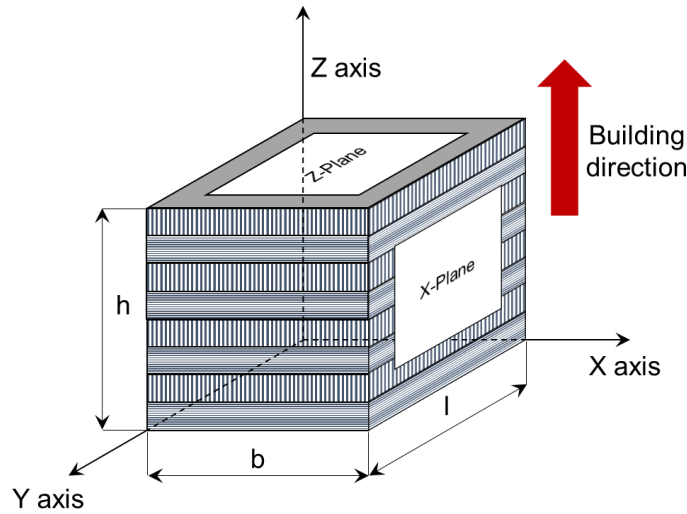


*Figure 17: EBM built Ti6Al4V cube specimen showing layer build up, Z-plane of the specimen represents building direction perpendicular to the vertical direction of the specimen while X-plane represents building direction parallel to the vertical direction, l=b=h=15mm*

The characteristics layer build-up process causes EBM-X to have anisotropic layers that shows different mechanical properties in the two axes of x and y, while, the EBM-Z has transversely isotropic layers showing similar mechanical properties in both the axes on the deposited layer [2, 11, 14]. The 15 x 15 x 15 mm³ EBM cube is cut with fine abrasive diamond cutter into three specimens of thickness 5 mm each with same cross section,

56

while, mill-annealed sample obtained as 1" diameter cylinders is cut by electronic discharge machining to 15 x 15 x 5 mm$^3$ in dimension. After the samples are cut to required dimension, each sample is hot mounted onto a phenolic polymer.

According to ASTM E2546: Standard Practice for Instrumented Indentation Testing: in order to perform nano- and micro-scale indentation tests, the sample surfaces are required to be mirror finished. The as-built samples are mechanically ground and polished by standard metallographic sample preparation methods, with successive grit polishing to 4000 grit followed by 0.06 μm silica suspension on micro fiber cloth giving mirror-like finish. The samples were thoroughly sonicated successively with acetone, methanol and distilled water for ten minutes and inspected under optical microscope before performing the tests. The average roughness is Ra (centerline average) = 23.5 ± 1.4 nm over 200 μm length profiles.

### 4.2.3 Microstructure and Characterization

In order to understand the relation of the anisotropy observed in the samples processed with different processing techniques and its resulting mechanical properties, microstructure of each individual builds are inspected. The samples are mirror polished and are prepared for optical metallography by etching in a solution of 100 mL $H_2O$, 6 mL $HNO_3$, and 3 mL HF. The etched samples on their Z-plane are observed in a Zeiss A/M optical microscope under dark and bright light scopes. Further, EBM-X and EBM-Z are investigated by X-ray diffraction (XRD) and Energy Dispersive Spectroscopy (EDS) to determine the phases present and the chemical composition of individual phases. Crystallographic phase identification is obtained by XRD using a Bruker Prospector CCD Diffractometer copper micro-source X-ray tube at room temperature. XRD are carried out in the range of 20 - 90°

for a period of 2 hours. EDS analysis in the form of horizontal line scan is conducted along a 10 µm line scan from etched samples to determine the chemical composition and atomic weight percentages of the elements present from the scanned area.

A series of nano-indentation tests are performed on mill-annealed, EBM-X and EBM-Z samples with a nano-module M1 mechanical tester from Nanovea (Irvine, CA). Instrumented indentation testing (IIT) is utilized to determine mechanical properties for the samples with respect to their build. IIT is shown to have successfully determined mechanical properties namely elastic modulus, hardness and yield strength of materials [15-17].

Standard Berkovich indenter is used to indent in random spots on Z-planes of mill-annealed, EBM-Z and EBM-X specimens to determine local elastic modulus and hardness while cylindrical flat top indenter is employed to evaluate yield strength of the materials. The nano-indentation technique is a force driven system that engages a constant loading rate of the indenter while simultaneously measuring nanoscale displacement over a complete indentation cycle. The correlation between indentation load and displacement is made to determine the fundamental mechanical properties. Indentation parameters used are summarized in *Table 4*. In total, nine Berkovich indents are made using mapping feature in random areas of the EBM-Z, EBM-X and mill-annealed samples to determine the elastic moduli. The unloading portion of the load-displacement curve (10 - 40%) is considered as an elastic recovery of the material and is used to evaluate contact stiffness to determine the elastic modulus. Average value for each set of experiments are analyzed to compare the mechanical properties for all set of builds. A representative load-displacement curve to evaluate elastic modulus for each build material is shown in *Figure 18 (a)*.

*Table 4: Nano-indentation Test Parameters*

| Elastic modulus measurement | | Yield strength measurement | |
|---|---|---|---|
| **Parameter** | **Value** | **Parameter** | **Value** |
| Indenter | Standard Berkovich | Indenter dime | 5 µm - diameter |
| Peak load | 140 mN | Peak load | 100 mN |
| Loading rate | 280 mN/min | Loading rate | 200 mN/min |
| Unloading rate | 280 mN/min | Unloading rate | 200 mN/min |
| Creep time | 0 sec | Creep time | 0 sec |
| Contact load | 0.1mN | Contact load | 0.1 mN |

Yield strength measurements are carried out using a 5 µm diameter diamond cylindrical flat punch. The loading portion of the load displacement curve is utilized to determine the yield strength of the material. The yielding is set to occur during the loading of the indenter and at a load where the material starts to deform plastically, the material yields at this point. Using the slope of the load against the displacement, point of inflication is calculated and at the maximum slope, the yielding load is determined. The yielding load (P) divided by the area of impression given by $P/\pi a^2$ where, a is the contact radius of the indenter, gives the yield strength of the material. A representative load-displacement curve is shown for indentation with a cylindrical flat punch and load at yield point is marked in the plot in *Figure 18 (b)*.
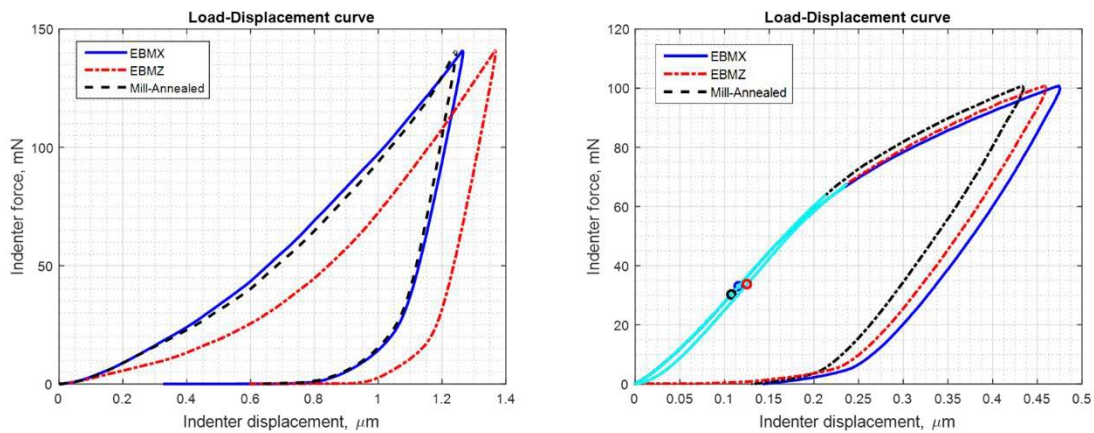


*Figure 18: Load-displacement curves for specimens obtained from (a) A Standard Berkovich Indentation and (b) Cylindrical Flat-top Indentation*

## 4.2.4 Experimental Procedure

Commercially pure (CP) grade-2, 1mm diameter Ti-spheres supplied by Nanovea (Irvine, CA) are used to conduct the single sliding contact fatigue experiment. The Ti-spheres attached to an indenter holder is rubbed against the as-built Ti sample surfaces in order to emulate the practical application as in the case of a custom modular prosthesis wherein a medical grade Ti-alloy femoral head contacts femoral stem at the interface. The material properties of the medical grade-2 Ti-alloy supplied by the manufacturer is provided in *Table 5*.

*Table 5: Mechanical Properties of CP grade-2 Ti-indenter head*

| Modulus of Elasticity | Percentage weight composition (%) of elements | | | | | |
|---|---|---|---|---|---|---|
| 103 GPa | Carbon (C) | Iron (Fe) | Oxygen (O) | Nitrogen (N) | Hydrogen (H) | Titanium (Ti) |
| Poisson's Ratio 0.35 | 0.1 | 0.3 | 0.25 | 0.03 | 0.015 | Balance |

In order to take into account effects of indenter being worn prior to the scratch test, the indenter balls are thoroughly sonicated in acetone before use and never reused. Hertzian contact theory is applied to determine the elastic contact load required to perform the reciprocating sliding test. Assuming the real contact between the sample surface and the indenter to be elastic in nature, normal contact load corresponding to 25 % of the Hertzian contact pressure is chosen as the testing load. Elastic moduli for indenter and sample along with their corresponding Poisson's ratio are used to obtain a composite elastic modulus for the contacting pair of surfaces. The semi-contact radius for a circular contact is then calculated with iterative normal load values giving a range of contact radii for varying loads. With known yield strength of the material obtained from IIT, 25 % of the yield stress value is equated with the iterative contact pressure obtained by dividing the iterative load

with real contact area computed by Hertzian contact theory at yield point. The equations

and the process used to calculate the normal test load is summarized in *Table 6.*

Table 6: Summary of determination of test load using Hertz Contact Theory

| Contact Parameters | Calculated Values |
|---|---|
| Elastic contact pressure ($P_e$) $$P_e = 0.25 * \sigma_{y\ avg}$$ | $\sigma_{y\ avg}$ = 1272 MPa $P_e$ = 0.25*1272 = 318 MPa |
| Composite Elastic Modulus ($E_r$) $$\frac{1}{E_r} = \frac{1-v^2}{E} + \frac{1-v_i^2}{E_i}$$ | $v_i=v=0.35$ E = 114 GPa $E_i$ = 103 GPa $E_r$ = 61691.40 MPa |
| Semi-contact radius (a) $$a = \left(\frac{3WR}{4E_r}\right)^{\frac{1}{3}}$$ | W = 10mN, a = 0.00393mm W = 20mN, a = 0.00495mm W = 30mN, a = 0.00567mm W = 40mN, a = 0.00624mm |
| Average Contact Pressure ($P_r$) $$P_r = \frac{W}{\pi a^2}$$ | $P_r$ = 205.89 MPa $P_r$ = 259.41 MPa $P_r$ = 296.95 MPa $P_r$ = 326.84 MPa ← |
| @ $P_e$= $P_r$ | W = **37**mN, a = 0.00608mm, $P_r$ = 318 MPa |

Single asperity reciprocating sliding contact fatigue experiment (pin-on-flat) is

performed complying to ASTM B-2 standards to simulate the relative motion at the

interface between the femoral head and the stem (MoM hip joints) on z-planes of finished

EBM-Z, EBM-X and mill-annealed specimens. The schematics of the pin-on-flat wear test

and wear area is shown in *Figure 19 (a)* where a CP grade-2 Ti-pin reciprocates on mirror

polished sample surface. Wear tests are performed based on the orientation of the layer

buildup of differently processed samples to analyze the effects of anisotropy. For EBM-X,

reciprocating tests are performed in two directions: along and across the layer deposition.

In addition, in the case of EBM-Z, wear tests are performed in two distinct directions

inclined at 45° to one another. For transversely isotropic mill annealed sample, tests are

performed along directions that have random orientations. The schematics of the test setup

for all material build is depicted in *Figure 19 (b)* through *(d)*. The parameters for the

reciprocating wear tests are chosen considering an oscillating frequency of 1 Hertz of travel

in a normal walking motion. The in-vitro fretting fatigue test is carried out for a time period

of 30 minutes. With the sliding traverse of the indenter head at 0.1 mm per second and a

total sliding distance of 100 μm, each test is performed for 900 cycles. The test parameters

for the reciprocating wear test is summarized in *Table 7*. All tests are performed in a closely

monitored environment with temperature 25 ± 3° C and relative humidity 27 ± 3 %.
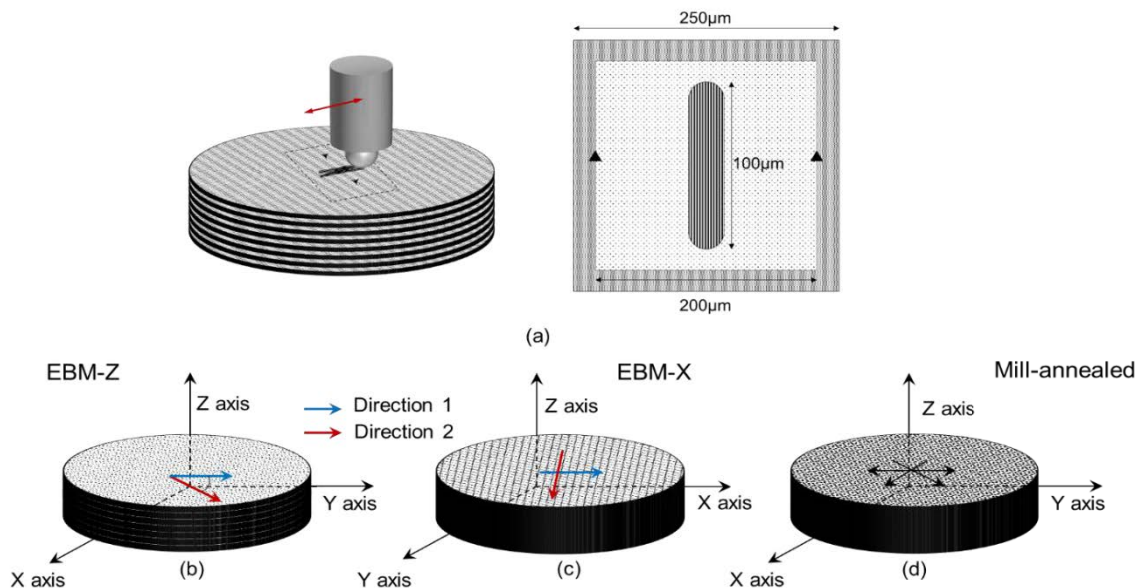


*Figure 19: Wear test schematic showing (a) Pin-on-flat test setup and wear area schematic (b) EBM-Z (c) EBM-X and (d) Mill-annealed sample. Arrows over the surface indicate the direction of tests performed*

*Table 7: Pin-on-flat Experimental Parameters*

| Parameters | Value |
|---|---|
| CP grade-2 Ti-pin | 1 mm diameter |
| Normal contact load | 37 mN |
| Sliding distance | 0.1 mm |
| Sliding speed | 0.6mm/s |
| Wear test duration | 30 mins |

The wear test is quintuplicated on z-plane of each individual specimens with consistent testing parameters and environments. The number five is chosen for quantified wear volume to have statistical significance. All tests are performed in dry ambient environment and the effects of building orientations and sliding directions on contact fatigue process are studied.

The sample and the pin surfaces are inspected using a single point 3D optical profilometer PS2 (Nanovea, CA). The estimation of wear volume involves the technique of deducting the height values of a 3D surface scan data between the initial and final scan of the worn surface before and after the wear test. The optical profilometer scans the surface topography by combining sets of linear scan runs over a given area. The profilometer is rastered within a square area of 0.25 x 0.25 mm$^2$ with the wear test positioned at the center of each scan. The schematics of the scan for the entire wear estimation is shown in *Figure 20*. In order to have sufficient amount of data points to analyze the wear volume, finer resolution scans with a pixel size of 1 μm in both x and y axes of the scanning plane is chosen. The scan parameters for generating the surface topography of the wear area is summarized in the *Table 8*.
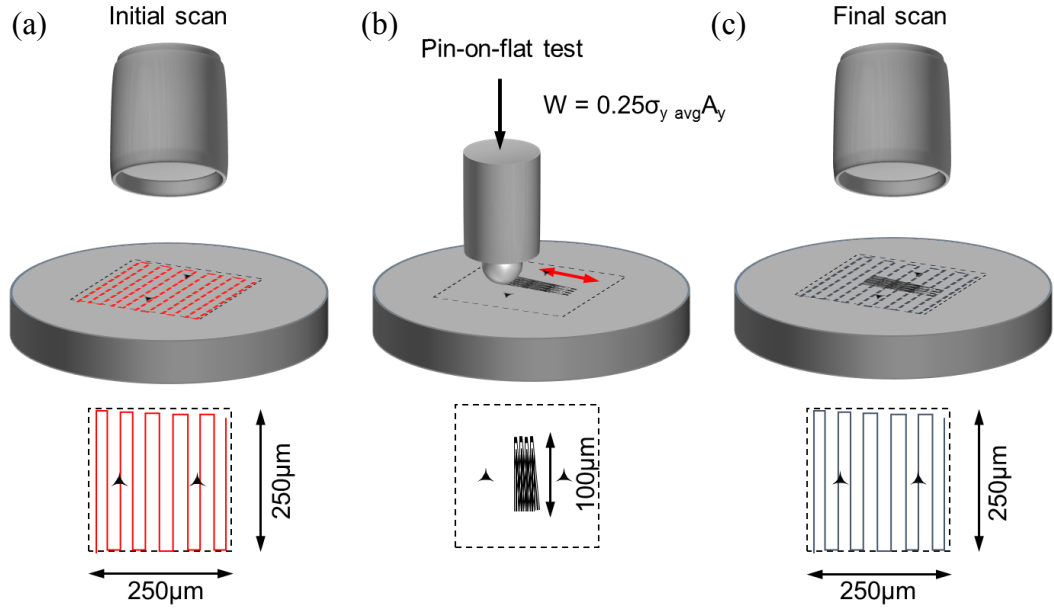
*Figure 20: Overall wear characterization schematics showing optical profilometer to scan the a) initial and c) final topology of the surface. Also shown is b) sample undergoing pin-on-flat test*

*Table 8: Surface scan parameters*

| Parameters | Value |
|---|---|
| X scan length | 0.25 mm |
| X step size | 2.5 μm |
| Y scan length | 0.25 mm |
| Y step size | 2.5 μm |
| Acquisition Rate | 2000 Hz |
| Averaging | 150 |

Image analysis is done to perform wear volume measurement of the scanned surface data. Berkovich impressions are made on both sides of the wear test to take into account any translation effects if ever the sample needed to be unmounted from the stage and replaced.

The image processing allowed the user to pick the impression points that served as reference to align the wear test data from before and after scans. This is done to evaluate the wear volume in a more precise manner and to consider any undesirable translation of

the sample and surface flaws. The scanned surface data is flattened using a quadratic interpolation of surface height values for both initial and final scanned surface data. The surface data is normalized by subtracting off from the mean roughness values. By subtracting the final levelled surface data from the initial levelled surface data, precise wear volume is calculated. A representative wear volume analysis of a single wear test is shown in *Figure 21*.

(a)

(b)

(c)
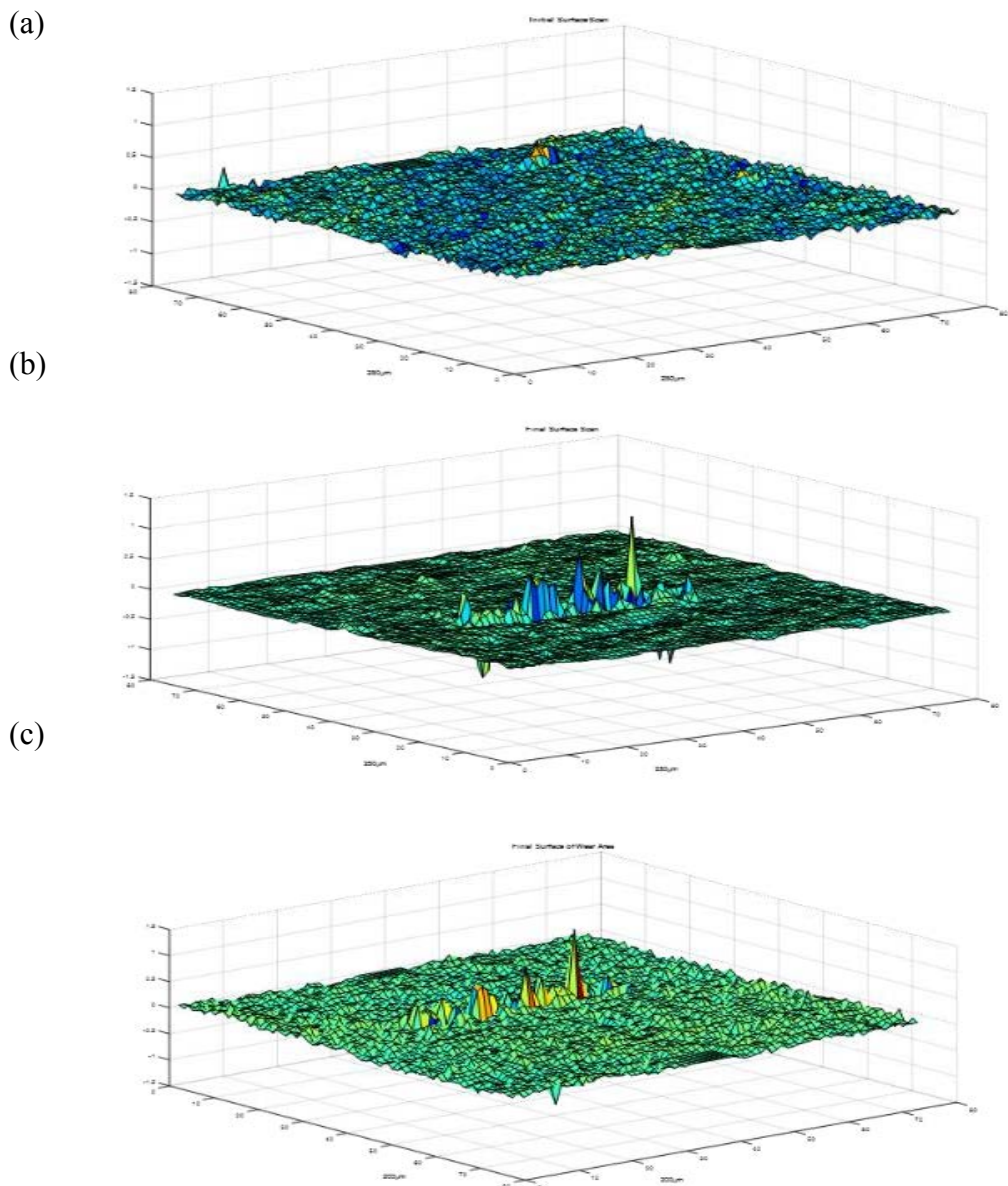


*Figure 21: Representative surface topography obtained after image processing (a) before wear test (b) after wear test and (c) final surface after deduction*

## 4.3 Results and Discussion

### 4.3.1 Microstructure

As described on the literature by numerous authors [10, 14, 18] the bulk microstructure of EBM-built Ti6Al4V consists of uniform lamellar acicular α-plates oriented in different directions as shown in *Figure 22 (d) and (e)*. α-colonies are found in small number while ß-rods are located sparingly throughout the microstructure. The grain boundary α are observed along some of the grain boundaries of the prior ß-phase. Within the prior ß-grains, a transformed (α+ß) microstructure is seen with both colony and Widmanstatten morphology for both EBM-Z and EBM-X. From z-plane of EBM-X, distinct long irregular columnar prior-ß structure are seen as dark and light bands whereas EBM-Z shows the microstructure parallel to the build direction in which an equiaxed microstructure can be observed. Within the columnar prior ß-grains (α+ß) lamellar microstructure is observed for both the planes parallel and perpendicular to the build. The width of the columnar prior ß-grains varies significantly from some 200 μm to over 1000 μm in length. Also noticable is the scanned layers in for the EBM-X surface *Figure 22 (a) and (b)*. Mill-annealed Ti6Al4V shows the bulk microstructure of globular crystals of ß present in an α-matrix. The equiaxed microstructure is seen throughout all planes of mill-annealed sample with dark ß-phases embedded in light α-matrix as seen in *Figure 22 (c)*. XRD scan as in *Figure 23* revealed α and ß-phases. This XRD study supports crystallographic phase observations on EBM built Ti6Al4V by optical microscopy. α-Ti (HCP) and ß-Ti (BCC) phases are seen in the diffraction pattern with characteristic peaks (101) for α-phase and (110) for ß-phase. The XRD data corroborates numerous XRD studies performed on EBM-Ti6Al4V in the literature [7, 10, 11, 18]. *Figure 24 (a)* shows SEM image taken on backscattered mode

where ß-phase are seen as the bright flat or circular rods orienting in the plane perpendicular to the screen and α-phase as the dark plate like structures. ß-phase is known to have a higher percentage of ß-stabilizing elements such as V, Mo while α-phase has very low percentage of the ß-stabilizers. EDS taken from bright and dark regions from the microstructure are shown in *Figure 24 (b)*. EDS spectra of α-phase consists of atomic percent of 86.2 % of titanium, 3.6 % of vanadium, and 10.2 % aluminum, while, ß-phase which if found in smaller concentration consisted of greater atomic percent of vanadium with 76 % of titanium, 18 % of vanadium and 6 % of aluminum. The greater atomic percentage of V as in the case of z-plane of EBM-X specimen stabilizes the ß-phase by lowering α-ß transition temperature. Therefore, more amount of vanadium is detected that induces very fine ß-precipitations in Widmanstätten α-platelets. This is verified by backscatter micrographs taken of the polished microstructure.
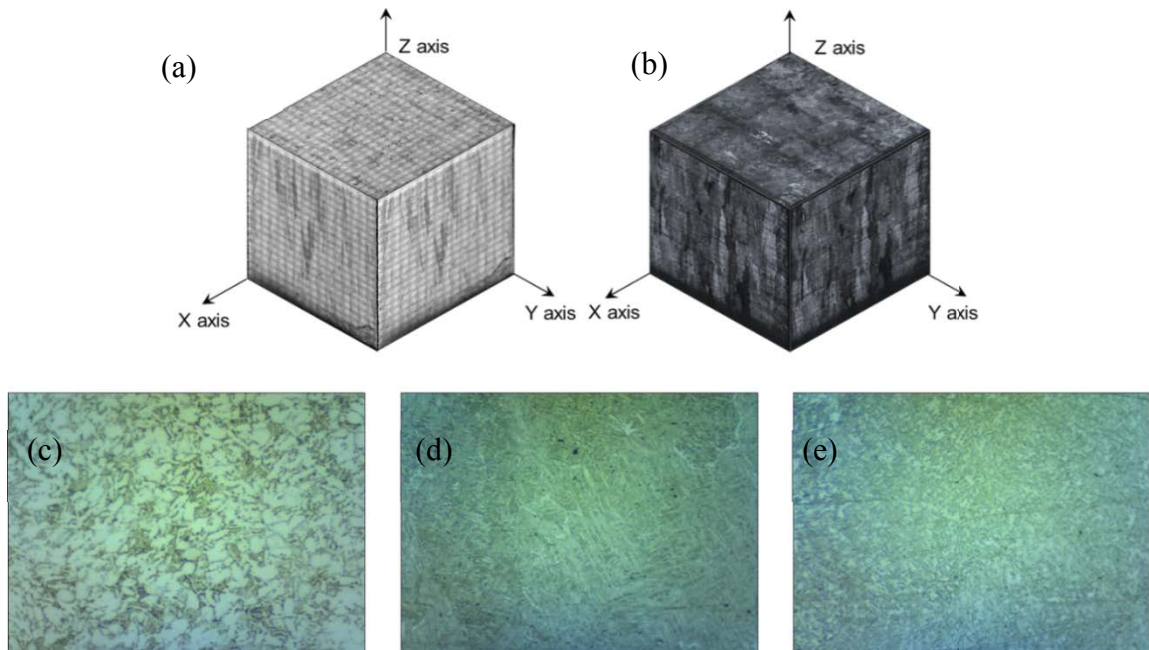


*Figure 22: 3D microstructural EBM specimen cube (15 x 15 x 15 mm3) shown in (a) bright field mode and (b) dark field mode, Microstructure comparison among mill-annealed (c), EBM-X (d) and EBM-Z (e) specimens*
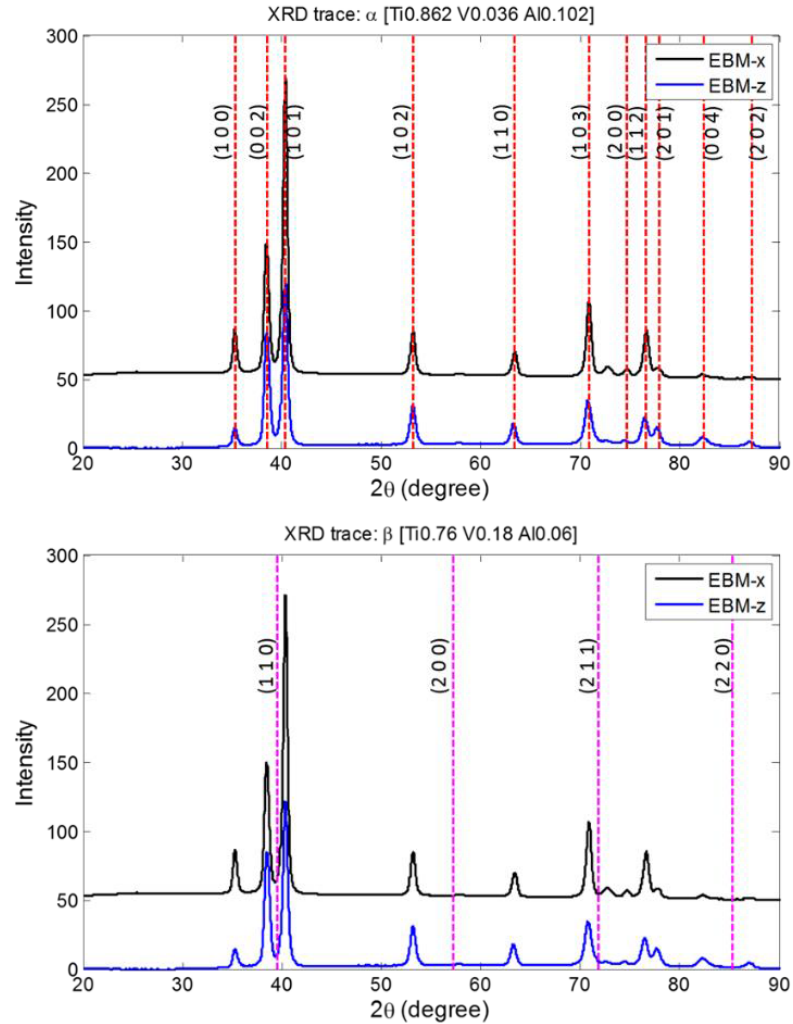
*Figure 23: XRD spectrum of EBM built specimen and phases present*

The phase appears brighter in contrast due to the increase of vanadium in the localized phase. It forms non-homogeneous microstructure. The z-plane of EBM-Z specimen presents relatively uniform distribution of rod shaped ß-grains. It establishes transversely isotropic surface [19]. In addition to the build orientations, the EBM pattern used to develop two different specimens causes different effects from isothermal annealing and therefore the finer α/ß microstructure on EBM-Z specimen induces greater elastic moduli and yield strengths.
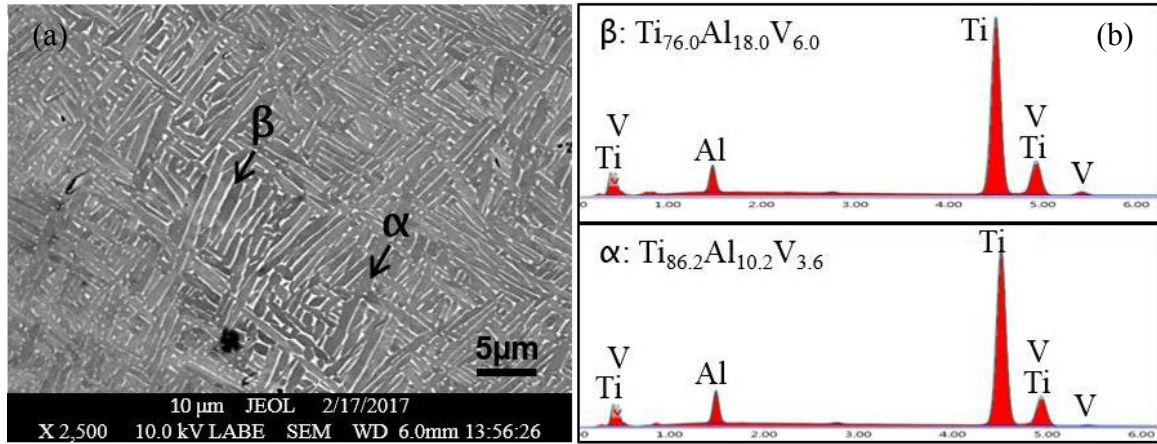
*Figure 24: EDS inspection of chemical composition: ß-phase showed to have greater atomic fraction of vanadium (ß-stabilizer)*

## 4.3.2 Mechanical properties of EBM and mill-annealed Ti6Al4V

Instrumented Indentation Technique (IIT) is utilized to characterize the mechanical properties for various Ti6Al4V builds. Using a standard Berkovich tip, a total of 9 indentation tests performed on EBM-X, EBM-Z and mill-annealed samples provided the elastic modulus and indentation hardness. Indentation stiffness is obtained from the slope of the unloading portion of a load-displacement curve, which are used to calculate elastic moduli for each Ti6Al4V builds. The averaged elastic moduli of each specimen represent individual mechanical property of the corresponding Ti6Al4V-builds. *Figure 25 (a)* summarizes the average elastic moduii and indentation hardness of all Ti6Al4V builds. The results obtained concludes Elastic modulus, which is the measure of a material's stiffness or resistance to elastic deformation, to be the least in EBM-X among the EBM-builds, while the bulk-manufactured mill annealed has the highest elastic modulus.

Indentation hardness is calculated simply by dividing the contact load by the projected area of indenter impression. In calculating the projected area, the depth associated with the impression is always plastic. Hence, in most metals that undergo indentation deformation, the depth of the indenter impression is primarily the result of plastic deformation. For this

fact, indentation hardness gives a good metric of plastic deformation among different materials and as such is closely related with the yield strength of the material. *Figure 25 (a)* shows mill-annealed Ti6Al4V to have the highest indentation hardness compared to the EBM builds. The superior indentation hardness of mill-annealed TI6Al4V is accounted by the microstructure being equiaxed and homogenous throughout the material. Surprisingly, within the AM built samples, the lesser homogeneous material with anisotropic characteristic showed to have superior indentation hardness compared to transversely isotropic counterpart. Theoretically, in the literature, relations derived among indentation hardness and elastic modulus are shown to be directly proportional to one another [Johnson's Expanding Cavity model]. However, the same relation is seen in mill-annealed and EBM-Z while it is not so for EBM-X.
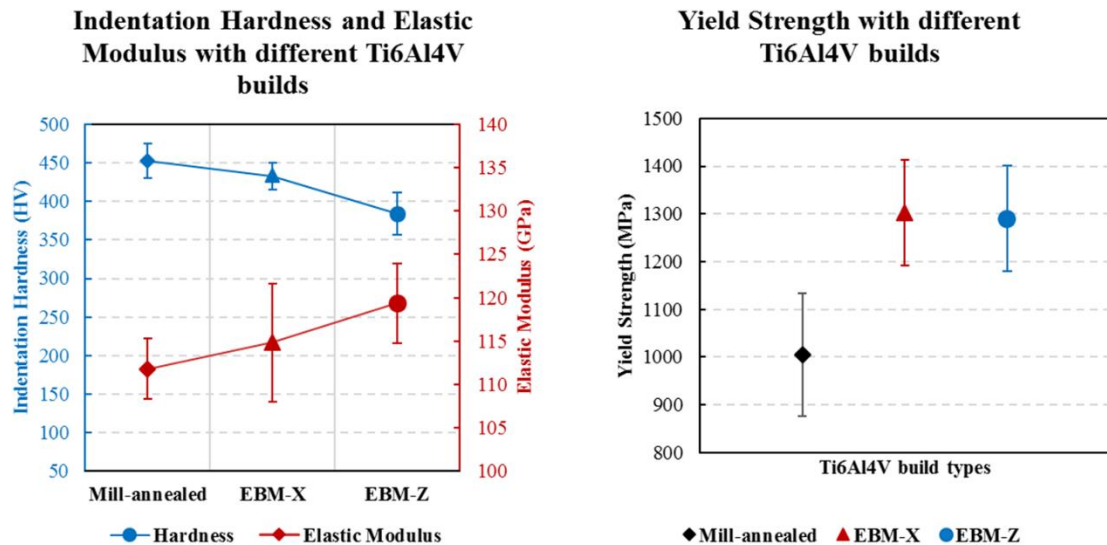


*Figure 25: Comparison of indentation hardness, elastic modulus and yeild strength obtained from nano-indentation for conventional mill-annealed Ti6Al4V vs additively manufactured EBM Ti6Al4V*

The yield strength determined by cylindrical flat punch indentations provide a measure of comparing one face of mechanical property: Yield strength. The diameter of the flat punch used is 5 μm. The yield point is identified at the maximum indentation stiffness

(dP/dh). The load at the maximum slope of the load-displacement curve is divided by the circular impression area. The load at this point initiates the onset of strain hardening on the material under loading and causes the material to yield. The average of 9 flat punch impressions are presented on *Figure 25 (b)* for all three specimens. The results show that the yield strength is the least for mill-annealed Ti6Al4V with 1005 MPa and comparable values of 1302.23 MPa for EBM-X and 1290.31 MPa for EBM-Z specimens. The yield results corroborate with the indentation hardness obtained for the additively manufactured samples while the case is not true for mill-annealed specimens. The values of yield strength for EBM-Ti6Al4V for both builds were comparatively higher from the published yield strength values given by the manufacturer. However, literature shows that the yield strength for parts manufactured by EBM shows a variation in the yield strength value ranging from 900-1400 MPa. For the case of mill-annealed Ti6Al4V, the results were still higher than the manufacturer's report but the deviation obtained was smaller.

### 4.3.3 Dry sliding wear behavior of Ti6Al4V surfaces

The volumetric wear for five tests are quantified using an optical profilometer and image processing and the average of the results are presented in *Figure 26*. All of the tests are performed in the ambient environment. 1mm grade-2 Ti6Al4V sphere is used in grinding the sample with abrasive wear on the Ti-surfaces. Reciprocating sliding contact tests are performed in two different orientation on each set of sample to identify the effects from the combination of surface anisotropy and sliding orientation.

During the sliding fatigue contact test, the reciprocating motion of Ti-sphere is set as both parallel (D1) and perpendicular (D2) to the build direction for EBM-X specimen. While, for EBM-Z specimen, two directions (D1 and D2) chosen are always perpendicular

to the build direction, but are angled to one another at 45°. For mill-annealed specimen, the

sliding orientation are chosen randomly since the material is transversely isotropic.
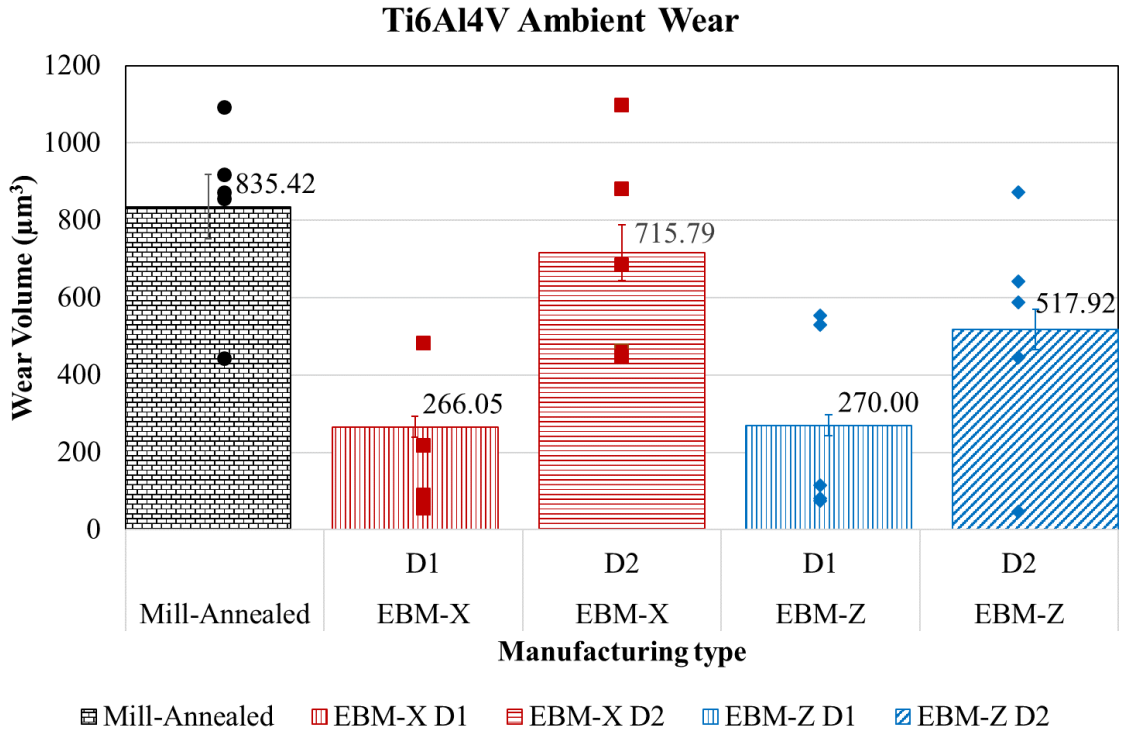


*Figure 26: Wear response of mill-annealed and EBM-Ti6Al4V as a function of build orientation and sliding direction*

The volumetric wear is determined as 835.42 $\mu m^3$ for mill-annealed specimens, which

was the greatest among all the material builds. For laterally built EBM-X specimen, tests

done on the direction D2 (across the deposited build layers) showed to have the second

greatest volumetric wear of 715.79 $\mu m^3$. On the contrary, test performed along the vertical

direction of the deposited layers showed to have the least wear volume of 266.05 $\mu m^3$ for

the entire study. This seems legit for the fact that tests performed, do not intersect prior

beta grain boundary and there are enough chances of the test to lie within a single prior ß-

grain region. The size of the prior ß-grain is in the order of several hundred microns

magnitude as shown in *Figure 22 (a)* and *(b),* while the wear width of the reciprocating

test is roughly around 10 microns. Comparing the wear volume among the vertically and

horizontally oriented tests in EBM-X specimen, significant difference in the wear is observed simply by varying the orientation of the tests. Similar difference is seen for EBM-Z specimen where the wear increased by a factor of 1.92, from 270.00 to 517.92 $\mu m^3$, when the angle between the tests was oriented at 45°. Ideally, EBM-Z has orthogonal anisotropy ($E_x = E_y$) on its build plane and should have comparable wear characteristics but this clearly was not the outcome from the experiments.

Additionally, a one-way analysis of variance (ANOVA) test was performed to determine if the means of the wear volume for the additively manufactured samples were statistically different from one another. The results from one-way ANOVA is presented in *Table 9*. It can be observed that there was a significant effect of sliding test orientation on the wear response of the EBM samples at the p<0.05 level for the four conditions: EBM-X D1, D2, EBM-Z D1 and D2 [F (3,16) = 3.419, p = 0.043].

*Table 9: One-way ANOVA results for wear volumes of EBM-X and EBM-Z specimens*

ANOVA

| Source of Variation | SS | df | MS | F | P-value | F crit |
|---|---|---|---|---|---|---|
| Between Groups | 706330.1714 | 3 | 235443 | 3.419 | **0.043** | 3.2388715 |
| Within Groups | 1101806.496 | 16 | 68863 | | | |
| | | | | | | |
| Total | 1808136.668 | 19 | | | | |

Overall, the EBM-Z sample is seen to have greatest wear resistance in the dry ambient environment while the mill-annealed sample has the least wear resistance. This could be explained by the fact that comparatively, mill-annealed being the hardest of the material results in the softer indenter grade-2 Ti material to wear out quicker as compared to when rubbed against the EBM-built counterparts. As a result the wear debris that are chipped off from the indenter material in combination with the wear debris produced from the sample surface during the wear tests, result in the contacting pair to wear in combined mechanism

of fretting, surface fatigue and three-body wear. The fine particulate debris that spalls off during the test when oxidized in the air produces harder oxide particles, which abrades the metal surface even further and the wear accelerates as the test progresses. Hence, this mechanism could possibly explain the highest wear behavior in the dry ambient environment as in the case of mill-annealed specimen. The lesser wear seen in the case of AM-built Ti6Al4V is accounted by the lower stiffness (elastic moduli) and indentation hardness of the material.

## 4.4 Conclusion

Wear characteristics of Ti6Al4V alloy manufactured from two different techniques are evaluated for the purpose of biomedical implementation. Fatigue contact of spherical titanium slider was used to simulate fretting motions at modular interfaces of hip prostheses. Pin-on-flat wear tests are carried out in dry ambient environment with oscillating tribometer in accordance with the standards ASTM G133-95. The tribological response of the different Ti6Al4V materials as influenced by anisotropic grain morphology, microstructure and mechanical properties are investigated. The following observations and conclusions are drawn.

i) The microstructure of mill-annealed Ti6Al4V is found to be equiaxed (α+ß) structure, with ß-lamellae homogenously distributed in the α-matrix. EBM specimens showed to have uniform lamellar acicular α-plates surrounded by sparingly distributed ß-rods, some colonies of α are also seen. In both of the build orientations, the characteristic, basket weave Widmanstatten pattern in Ti6Al4V is observed. For EBM-X specimen, prior-ß grains were characteristic feature having light and dark bands of long columnar structure. The prior ß-

grain boundary presented α-grain boundary. EBM-Z specimen, showed to consist of patches of α-colonies homogenously distributed through its z-plane.

ii) Both elastic modulus and indentation hardness show the traditional mill-annealed material as the superior-most among all materials under study. The elastic modulus is the least for mill-annealed Ti6Al4V making it more suitable as an implant material since lower moduli reduces the stress shielding effects in implants. The EBM-samples had comparatively higher elastic moduli with lower indentation hardness with EBM-X having properties in between mill-annealed and EBM-Z specimens. Yield strength however, obtained by IIT is found to be comparable with the published value for mill-annealed sample while for EBM-builds the values obtained were higher than the published data. On the contrary, the obtained yield strength values do comply with the experimental results of yield strength determined by numerous researchers. Among the EBM-X and Z, both have very close yield strength values.

iii) The wear behavior seen in all tests are characterized by fretting in combination with surface fatigue. Mill-annealed samples exhibited greatest wear loss while EBM-Z surface showed to have the most wear resistance for test performed at an inclined direction. For EBM-X specimen, tests performed inline with the layer deposition showed to have higher wear resistance as compared to tests performed across the layers.

The experimental result concludes tribological response is in accordance with the measured mechanical properties. The influence of anisotropic grain morphology significantly changes the wear resistance of EBM built joint implants. The transversely

isotropic plane of EBM-Z specimen has superior fatigue resistance. In order to promote the fatigue and wear resistance, the build orientation is critical and it is necessary to study influence of thermal cycles on microstructure of products. Treatments would be applicable and necessary to obtain isotropic surface.

## 4.5 References

1.  Murr, L. E., Amato, K. N., Li, S. J., Tian, Y. X., Cheng, X. Y., Gaytan, S. M., ... & Wicker, R. B. (2011). Microstructure and mechanical properties of open-cellular biomaterials prototypes for total knee replacement implants fabricated by electron beam melting. *Journal of the mechanical behavior of biomedical materials*, *4*(7), 1396-1411.

2.  Harrysson, O. L., Cansizoglu, O., Marcellin-Little, D. J., Cormier, D. R., & West, H. A. (2008). Direct metal fabrication of titanium implants with tailored materials and mechanical properties using electron beam melting technology. *Materials Science and Engineering: C*, *28*(3), 366-373.

3.  Wikipaedia. Web Page. Data accessed 3/03/2017; Available from: https://en.wikipedia.org/wiki/Titanium_biocompatibility

4.  Song, B., Zhao, X., Li, S., Han, C., Wei, Q., Wen, S., ... & Shi, Y. (2015). Differences in microstructure and properties between selective laser melting and traditional manufacturing for fabrication of metal parts: A review. *Frontiers of Mechanical Engineering*, *10*(2), 111-125.

5.  Mathewson, B. B., Hebbart, R., Choitt, S., Newmant, W. S., Cawleyttt, J. D., & Heuerttt, A. H. (1998, January). Machine design, control and performance of automated computer-aided manufacturing of laminated engineering materials. In *Proceedings of the Solid Freeform Fabrication Symposium* (pp. 335-342).

6.  Gibson, I., Rosen, D., & Stucker, B. (2015). Direct digital manufacturing. In *Additive manufacturing technologies* (pp. 375-397). Springer New York.

7.  Kok, Y., Tan, X., Tor, S. B., & Chua, C. K. (2015). Fabrication and microstructural characterisation of additive manufactured Ti-6Al-4V parts by electron beam melting: This paper reports that the microstructure and micro-hardness of an EMB part is thickness dependent. *Virtual and Physical Prototyping*, *10*(1), 13-21.

8.  Sun, Z., Tan, X., Tor, S. B., & Yeong, W. Y. (2016). Selective laser melting of stainless steel 316L with low porosity and high build rates. *Materials & Design*, *104*, 197-204.

9.  Do, D. K., & Li, P. (2016). The effect of laser energy input on the microstructure, physical and mechanical properties of Ti-6Al-4V alloys by selective laser melting. *Virtual and Physical Prototyping*, *11*(1), 41-47.

10. Al-Bermani, S. S., Blackmore, M. L., Zhang, W., & Todd, I. (2010). The origin of microstructural diversity, texture, and mechanical properties in electron beam melted Ti-6Al-4V. *Metallurgical and materials transactions a*, *41*(13), 3422-3434.

11. Rafi, H. K., Karthik, N. V., Gong, H., Starr, T. L., & Stucker, B. E. (2013). Microstructures and mechanical properties of Ti6Al4V parts fabricated by selective laser melting and electron beam melting. *Journal of Materials Engineering and Performance*, *22*(12), 3872-3883.

12. Budinski, K. G. (1991). Tribological properties of titanium alloys. *Wear*, *151*(2), 203-217.

13. A. Molinari, G. Straffelini, B. Tesi and T. Bacci, "Dry sliding wear mechanisms of the Ti6Al4V alloy," *Wear,* vol. 208, no. 1-2, pp. 105-112, 1997.

14. Tan, X., Kok, Y., Tan, Y. J., Descoins, M., Mangelinck, D., Tor, S. B., ... & Chua, C. K. (2015). Graded microstructure and mechanical properties of additive manufactured Ti–6Al–4V via electron beam melting. *Acta Materialia*, *97*, 1-16.

15. VanLandingham, M. R. (2003). Review of instrumented indentation. *Journal of Research of the National Institute of Standards and Technology*, *108*(4), 249.

16. Wright, S. C., Huang, Y., & Fleck, N. A. (1992). Deep penetration of polycarbonate by a cylindrical punch. *Mechanics of materials*, *13*(4), 277-284.

17. Lu, Y. C., & Shinozaki, D. M. (2008). Characterization and modeling of large displacement micro-/nano-indentation of polymeric solids. *Journal of Engineering Materials and Technology*, *130*(4), 041001.

18. Lu, S. L., Tang, H. P., Ning, Y. P., Liu, N., StJohn, D. H., & Qian, M. (2015). Microstructure and mechanical properties of long Ti-6Al-4V rods additively manufactured by selective electron beam melting out of a deep powder bed and the effect of subsequent hot isostatic pressing. *Metallurgical and Materials Transactions A*, *46*(9), 3824-3834.

19. Safdar, A., Wei, L. Y., Snis, A., & Lai, Z. (2012). Evaluation of microstructural development in electron beam melted Ti-6Al-4V. *Materials Characterization*, *65*, 8-15.

# Chapter 5: Wear behavior of electron beam melting (EBM) and wrought Ti6Al4V alloys in simulated physiological solution: Effects of anisotropy, sliding orientation and microstructure

A paper to be submitted to Journal of Materials Engineering and Performance

S. Shrestha, J. Ryu and GP. Manogharan
Department of Mechanical and Industrial Engineering, Youngstown State University, Youngstown, OH, 44555

## Abstract

Metal-on-Metal (MoM) modular implant systems have been quite common in the TJR industry as compared to the Metal-on-Polyethylene (MoP) or Ceramic-on-Ceramic (CoC) with numerous academic researches focusing on studying, in particular, the wear and corrosion behavior of the MoM implants. Metal additive approaches, such as electron beam melting (EBM) is increasingly used nowadays to process biomaterial Ti6Al4V used in the THR implants, by selectively melting layers of metallic powder bed with high-energy electron beam. The aim of this study is to investigate the synergistic effect of tribo-corrosion for tribological contacts in simulated biological fluids in traditionally manufactured (wrought) Ti6Al4V and EBM Ti6Al4V alloy with the wrought material as reference. The tribological behavior of the materials in the physiological solution was investigated by employing a reciprocating pin-on-flat type test setup in accordance with ASTM G133-95. The physiological solution included phosphate-buffer-saline (PBS) solution and a protein concentration environment (PBS+BSA+HA) that had similar concentration to that of a synovial fluid. As a counter pair, a CP Ti sphere of 1mm in diameter was used. The results show the wrought specimen to have superior wear response

in both of the simulated environments. Another striking observation was the material wear for all builds in the protein rich environment C1 were significantly reduced when compared to the aqueous PBS environment. However, larger fluctuations in the wear behavior was observed for the protein rich environment. On average, material wear decreased by a factor of 12 and 20, for wrought and EBM-built, Ti6Al4V, respectively. Surface energy or wettability of the fluid, which plays a significant role in promoting lubrication by fluid entrapment, was accounted for by the greater wear resistance in the more viscous PBS+BSA+HA. The surface anisotropic effects on the wear behavior in the EBM-built specimens was found to be insignificant.

**Keywords:** EBM, Ti6Al4V, Physiological solution

## 5.1 Introduction

Ti6Al4V has been used as an effective implant material for quite a few years primarily because of its better mechanical properties, excellent corrosion resistance accounting to TiO$_2$ solid oxide layer, biocompatibility, relatively low Young's modulus, higher strength to weight ratio and non-magnetic behavior [1]. However, the tribological properties of Ti6Al4V is found to be poor because of "low resistance to plastic shearing, low work hardening and low protection exerted by the surface oxides [2]." It is for this reason that the Ti6Al4V with suitable mechanical properties that results in reducing the undesirable low wear resistance be manufactured. Additive manufacturing (AM) is particularly doing this by changing the way the metals and alloys are manufactured these days. Metal additive approaches, particularly, powder-bed fusion is increasingly used nowadays to process Ti6Al4V. Electron Beam Melting (EBM) is one of the powder-bed fusion process that selectively melts layers of metallic powder bed with a supplied computer aided design model for the part [3]. The advantage of this additive approach is manufacturing of customizable implants with desirable mechanical properties. EBM parts are reported to have manufactured at faster processing speed and the process is deemed to be energy-efficient as compared to other similar laser-based systems [4, 5]. Many have tried to characterize the microstructure and mechanical properties of parts: short, small builds to large-sized, manufactured by EBM [3, 5-8]. Some literature show properties superior compared to the cast parts while others report on both comparable and inferior properties. However, in regards to the wear and tribo-corrosion, which are considered as one of the important properties for biomedical application, to the best knowledge of the author, there have not been comprehensive studies focusing on the existing relationship between the

mechanical properties, microstructure, constitution phases, anisotropic effects and influence of synovial fluids on the wear of the material.

Although, Total joint replacements (TJRs) is considered as a landmark achievement in the orthopedic history, the number of revised surgeries being performed as a result of combined effects of wear and corrosion of the implant material has come out to be a heavy burden to the patients, surgeons and overall in the health care system [9]. Kurtz. *et al*. [10] reported that the number of TJRs (both total hip arthroplasty and total knee arthroplasty) is likely to be increased in the USA alone, by colossal 673 %. The studies clearly represent the magnitude of the problem, thus demand strong understanding of the phenomenon, and prompt mitigation of the issue.

The hip replacement system has been designed in the form of rotational ball and socket assembly. Modular designs favoring customization have been highly preferred with THR comprising components, namely, acetabular cup: a hemispherical cup implanted in metallic backup fixed into the pelvis, femoral stem: fitted into the femur, and a femoral head, that articulates in the acetabular cup. The most common combination of the components include metal-on-metal (MoM), metal-on-polyethylene (MoP) or ceramic-on-ceramic (CoC) or any other suitable combination.

In the modular THR design, accounting to the superior reduction of joint friction, the interface is made between metallic femoral head and polymeric acetabular insert. Biologically inert material such as ultra-high molecular weight polyethylene (UHMWPE) have also been used as an acetabular cup material, however, the presence of large amounts of inactive particular matter is seen to have accounted for strong macrophage responses leading to osteolysis at and around the bone-implant interfaces [11]. Loosening of

components of a hip replacement surgery has been largely accounted to local bone resorption due to polyethylene wear debris [9]. The lower wear resistance provided by the polymeric inserts limits its useful life.

MoM joint prosthesis have been used as an effective alternative to MoP bearings that was in the industry for about half a century [12-14]. For a 4-7 years follow-up, MoM articulation appeared to be more effective in reducing wear and loosening when compared with MoP articulation [15]. Larger femoral heads and thinner acetabular cups used in optimized MoM hip joint designs result in much smaller clearance causing much lower wear rates and wear volumes [16, 17]. However, while comparing both the designs, the quantity of metallic wear debris released for MoM is of nano-scale and are larger in number as compared to that released for MoP whose particle size is sub-micrometers. These minuscule particulate debris migrate into effective joint space stimulating foreign-body response causing bone loss due to induced osteolysis. As a result of the bone loss, joint friction escalates near the bone implant zones causing progressive degradation of the implant leading to its failure [18]. The extremely complex and variable conditions [19, 20] the TJR implants encounters, together with the tribological contacts made due to locomotion, causes accelerated degradation of the implant. Clinical examination reveal metal ions released from the implants onto the body leads to various phenomena: transportation, metabolism, accumulation in organs, allergic reactions and carcinoma. Large release of metal ions is generally considered harmful to human health [21-23]. Numerous reports showed that earlier designs for MoM hip joints survived for two to three decades while majority failed only after a few years [24, 25]. To tackle this important issue for improving the durability of currently employed implants, there has been numerous on-

going researches focusing on the development of optimum alternative materials or improving the wear resistance of existing materials for TJRs.

In terms of analyzing the wear response of the materials, commercial joint-simulators or tribological testing methods such as tribometer or pin-on-disk or pin-on-flat apparatus systems are employed. Results from the in-vitro wear tests as well as in-vivo studies of the retrieved implants suggests that the material degrades via a complicated intertwining mechanism among physical, chemical and physiological phenomena at the joint interface [26-28]. Mostly, past studies on wear and fretting corrosion of interfaces in TJRs have exclusively focused on determining the rate of material damage in order to compare the performance of different implant materials without the fundamental understanding of the multifactorial mechanism.

Currently most of the implant materials for TJRs are fabricated by conventional methods. Efforts are made to understand the microstructural evolution, distribution and mechanical properties of the AM parts, however, critical gap in the knowledge base that centers on the influence of AM induced microstructure on contact fatigue and oxidational wear of implants hinders the practical application of the AM-built implants. Therefore, there is an urgent need to develop an understanding of the multifactorial mechanism of wear and corrosion and identify an optimum microstructure resulting from stepwise additive layering that inhibits the implant failure. The purpose of this research is to investigate the behavior of AM-Ti6Al4V for THRs. In this article, the author will try to investigate the influence of the anisotropic microstructures of electron beam AM-made Ti6Al4V materials on wear and corrosion resistance in simulated synovial fluids. Findings from this research will help predict the overall life cycle of AM-made orthopedic implants under fatigue loadings at the modular joint replacements and help identify optimal AM build orientation for the vast application for biomedical devices.

## 5.2 Experimental Section

### 5.2.1 Materials, Fabrication and Sample Preparation

EBM-built samples were fabricated using Arcam Q10 (Arcam AB, Molndal, Sweden). The powder used to fabricate the parts was Ti-6Al-4V powder. The powder size ranged from 45 to 106 μm while the layer thickness for the build was approximately 50 μm. The nominal composition of the Ti6Al4V powder is provided as: 6.0Al-4.0V-0.03C-0.1Fe-0.15O-0.01N-0.0003H and the balance being Ti (wt. %). EBM Ti-samples were fabricated as cubes of dimension 15 x 15 x 15 mm$^3$. To investigate the anisotropy effects of the EBM process, samples were wire cut along vertical and horizontal plane of the build axis with thickness of 5 mm. To counter the effects of rapid solidification of the layers at bottommost and topmost region of the build, the middle slice was chosen and made ready to be prepared as shown in *Figure 27*. The cube sliced on the horizontal axis is termed as EBM-Z sample while the cube cut along the vertical axis of the build is termed as EBM-X sample throughout this article.
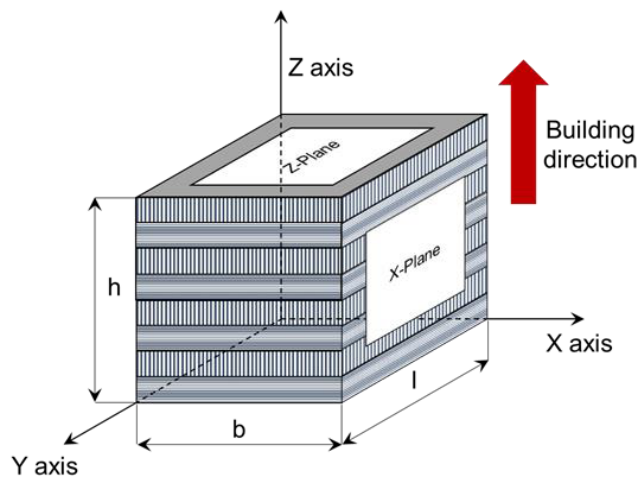


*Figure 27: EBM built Ti6Al4V cube specimen showing layer build up, Z-plane of the specimen represents building direction perpendicular to the vertical direction of the specimen while X-plane represents building direction parallel to the vertical direction*

The wrought mill-annealed Ti6Al4V samples were supplied in a form of a rod by ATI Allvac Corporation (Monroe, North Carolina) and had the dimension of dia. 25.4 mm x 100 mm. Mill-annealed Ti6Al4V samples were also sliced using fine abrasive diamond cutter into 15 x 15 x 5 mm$^3$ sample. Both AM and mill-annealed samples after they are cut into the required dimension are mounted onto a phenolic resin to be prepared metallographically. All three samples are mechanically ground successively through 180, 220, 320, 1000, 4000 grits followed by 0.06 μm silica suspension on micro fiber cloth giving mirror-like finish. After inspecting the surfaces in the optical microscope, all of the samples were ultrasonically cleaned in acetone, ethanol and de-ionized water for 10 minutes respectively and stored in a desiccator prior to testing. Surface roughness measures of the samples were performed by optical profilometer (S2) from Nanovea (Irvine, California). The average roughness Ra (center line average) of 18, 20 and 8 nm over 500 μm length profile was found for mill-annealed, EBM-X and EBM-Z samples.

### 5.2.2 Microstructural Characterization Techniques

The anisotropy in the build resulting in differing mechanical properties is related with the microstructure inhabited by the materials. For this purpose, the samples are required to be inspected at a microscopic level. The mirror-finished samples are etched using Kroll's reagent (92 mL $H_2O$, 6 mL $HNO_3$ and 2 mL HF) for 30 seconds. The revealed microstructure was mapped for the entire surface and the images stitched together in different planes are represented in microstructural cube for the EBM builds. Scanning electron microscope (SEM; JOEL-JSM-7600F; 20 kV, JOEL Ltd., USA) was employed to examine the microstructure. For chemical composition, energy dispersive x-ray

spectroscopy (EDX) (Oxford Instruments Plc., Abingdon, UK) equipped with SEM was used. For phase identification, (JEM-2100 SEM/TEM, JOEL Inc., USA) was employed.

### 5.2.3 Mechanical Properties Evaluation and Wear Test

Instrumented indentation technique (IIT) was employed to determine the mechanical properties: micro-hardness, elastic modulus and yield strength for all materials under study. Nanovea's M1 mechanical tester (Irvine, California, USA) machine was used with standard Berkovich indenter to determine micro-hardness and elastic modulus while 5 μm dia. cylindrical flat punch to determine the yield-strength. A detailed description of the evaluation of the mechanical properties is presented in Chapter 4, Section 4.2.3. Complying to ASTM G133-95, reciprocating pin-on-flat sliding wear tests were performed on polished surfaces on each individual samples in physiological aqueous mediums. Commercially pure (CP) grade-2 Titanium ball of 1 mm in diameter was used as a counter-face and rubbed against the reciprocating Ti-6Al-4V samples. The single asperity contact fatigue experiment had the following test parameters: the frequency of the test at 1 Hertz, sliding distance of 100 μm, sliding speed of 6 mm/s for a period of 30 minutes. Simple geometric equation of volumetric addition of the wear trench for the entire wear track gave the wear volume in cubic microns for each individual wear test. To analyze the effect of the anisotropy in the builds, a total of 5 tests were performed in the physiological solutions. Tests performed were oriented in specific directions based on different builds. For vertical built EBM-X specimen, two directions were chose, direction parallel (in line) to the layer deposition and direction perpendicular (across) the layer deposition. For horizontally built EBM-Z specimen, since the material is isotropic, wear tests should ideally yield similar results as no anisotropy is influenced. To vary the sliding orientation, a direction parallel

to the side and another direction at an angle of 45º was chosen. Similarly, for homogenous mill-annealed specimen, tests were performed in random orientations. The schematic of the wear test and the experimental design is made clear from *Figure 28*.
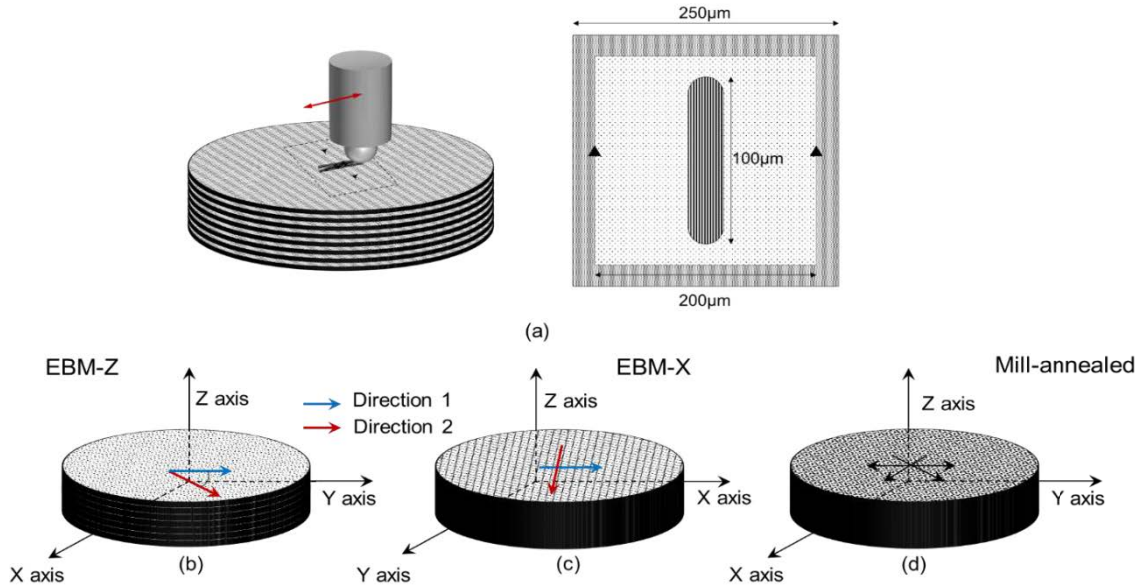


*Figure 28: Wear test schematic showing (a) Pin-on-flat test setup and wear area schematic (b) EBM-Z (c) EBM-X and (d) Mill-annealed sample. Arrows over the surface indicate the direction of tests performed*

## 5.2.4 Surface Characterization

Three-dimensional images of the worn surfaces were taken using a white-light interferometer based optical profilometer (Nanovea, Irvine, CA). Images of the surfaces were taken before and after experiments in order to evaluate the morphological changes that occurred as a result of the tribocorrosion test. Before conducting the test, target test area was marked using indentations to account for any translation effects. Additionally, the worn area, wear morphology and wear debris were investigated using SEM (JOEL-JSM-7600F; 20 kV, JOEL Ltd., USA) to examine the fretting behaviors of the interacting metal surfaces.

### 5.2.5 Synovial Fluids

The smooth motion between the bone surfaces of the femoral head and acetabulum in the joints is as a result of synovial fluid present on a durable layer of articular cartilage. A thin layer of roughly 50 μm of synovial fluid forms around the surface of the cartilage, which also seeps into the micro cavities and irregularities in the articular cartilage surface [29]. During the movement, the synovial fluid held in the cartilage seeps out mechanically to maintain a layer of fluid on the cartilage surface. The functions of a healthy synovial fluid includes reduction of wear and friction, shock absorption and nutrient and waste transportation. However, total joint replacements causes the natural cartilage to be replaced by the synthetic joint material usually in the form of MoM or MoP prosthesis. The useful lives of these prostheses are seriously affected when the joint interface goes through continuous surface fatigue and tribo-corrosion. The presence of elements such as Ni, Co, and Cr, in implants made out of stainless steels and Co-Cr alloys have been reported to have carcinogenic effects [30, 31]. Also, long-term existence of V and Al ions in Ti-alloys has been found to cause Alzheimer's disease, osteomalacia, and neuropathy in the long term [32]. The soluble and particulate debris that form as a result of combination of wear and trio-corrosion migrate locally or globally throughout the system and may induce a cascade of inflammatory events that may ultimately result in bone loss and subsequent implant failure. The adverse tissue reaction lowers pH level up from a normal value of 7.768 ± 0.044 to 2.0 and increase protein concentration up to 60 g/L in the synovial fluid. Therefore, the unhealthy joint fluid further influences the tribo-corrosion of the joint [33, 34].

To simulate the effect of protein concentration on the tribological response of the anisotropic implant materials, wear test of ASTM standard G199-95 is employed. As a control group, phosphate buffer saline (PBS) is used and a solution is prepared to replicate the healthy and unhealthy synovial fluid in human joints. Hyaluronic acid (HA) is a major structural component of cartilage that consists of an alternating copolymer β-glucuronic acid-(1-3)-β-N-acetylglucosamine-(1-4). Both of the hyaluronic acid (Sigma-Aldrich) and bovine serum albumin (Fischer Scientific) are dissolved in PBS to form an extracellular matrix-protein mixture. The solutions consist of the following compositions:

i.   PBS: NaCl 9g/L + $KH_2PO_4$ 0.144 g/L + $Na_2HPO_4$-$7H_2O$ 0.795 g/L

ii.  C1: PBS + 19g/L Bovine Serum Albumin (BSA) + 3g/L Hyaluronic Acid (HA)

A series of experiments are conducted to understand the influence of variable concentrations of synovial fluid on synovial lubrication effect. *Figure 29 (a)* shows the stage of the M1 tester to perform the simulated joint motion while *Figure 29 (b)* shows a custom liquid cell fabricated out of UHMPE to conduct the tests in simulated physiological solution.
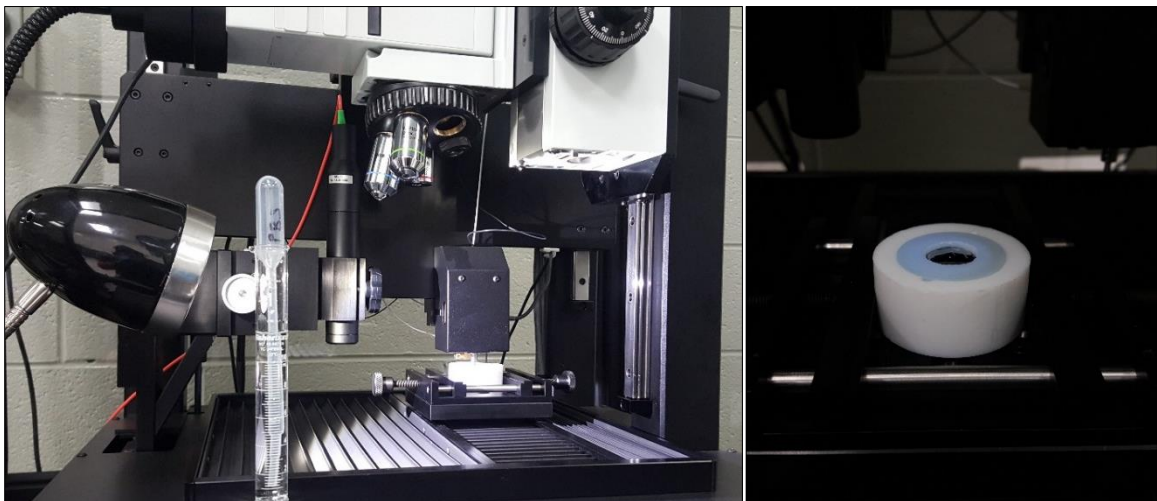


*Figure 29 (a) Nanovea Mechanical M1 Tester (b) Custom tribo-cell made of UHMPE used for aqueous environment test*

## 5.3 Results and Discussion

### 5.3.1 Microstructure

*Figure 30* shows the microstructure of mill-annealed Ti6Al4V and EBM-Ti6Al4V. Mill-annealed sample as in *Figure 30 (a)* shows characteristic equiaxed α/ß microstructure with globular crystals of inter-granular-ß embedded in α-matrix. It can be clearly seen that the majority of microstructure of the EBM-built sample is lamellar α/ß as in *Figure 30 (b)* and *(c)*. A much coarser but homogenous α/ß microstructure is seen in the as cast conventionally manufactured heat-treated specimen as compared to the AM EBM-built specimen which has much finer microstructure. Columnar prior-ß structure whose long
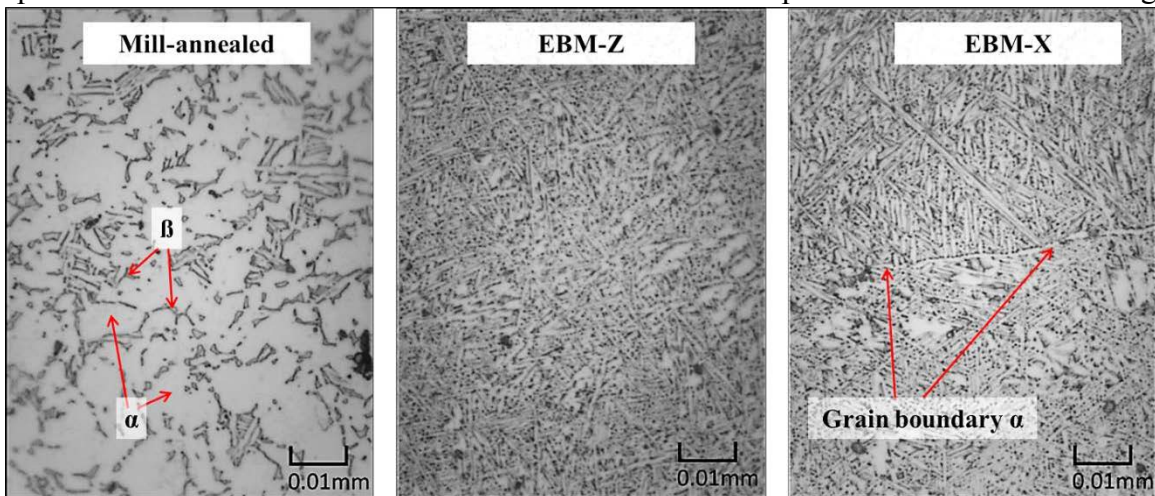


*Figure 30: Microstructure of Ti6Al4V showing (a) equiaxed α/ß for mill-annealed (b) basket-weave α/ß for EBM-Z and (c) widsmanstatten for EBM-X; Note: Grain Boundary α phase is seen running across as a horizontal line separating the columnar prior ß-grains in EBM-X sample*

axis is aligned with the build direction is seen in the z-plane of EBM-X specimen whereas equiaxed grains and fine Widmanstatten (α+ß) structure is seen in EBM-Z. The long columnar prior ß-grains are delineated by α-grain boundary as seen in *Figure 30 (c)*. Within the prior-ß, either colony (α+ß) or Widmanstatten (α+ß) is seen throughout the sample. XRD (X-ray diffraction) patterns shown in *Figure 31* obtained for EBM-X and EBM-Z samples show peaks mostly comprising α while characteristic ß-peak (220) was present for

ß-phase. This is in line with many microstructural studies previously done by authors [3, 5-8]. One interesting phenomenon observed on EBM-Z built sample was the variation of intensity seen for the characteristics ß-peak at different locations in the sample. XRD patterns revealing difference in the intensities meaning variation in the ß-content within the isotropic EBM-Z surface. From the XRD patterns obtained for the EBM-built samples, comparably stronger intensities were seen for ß-phase of EBM-Z specimen as compared to EBM-X specimen. Since, the approach for the determination of the mechanical properties of the specimens is instrumented indentation technique, which largely involves interaction within the surface volume of the material; the differing microstructure seen on the
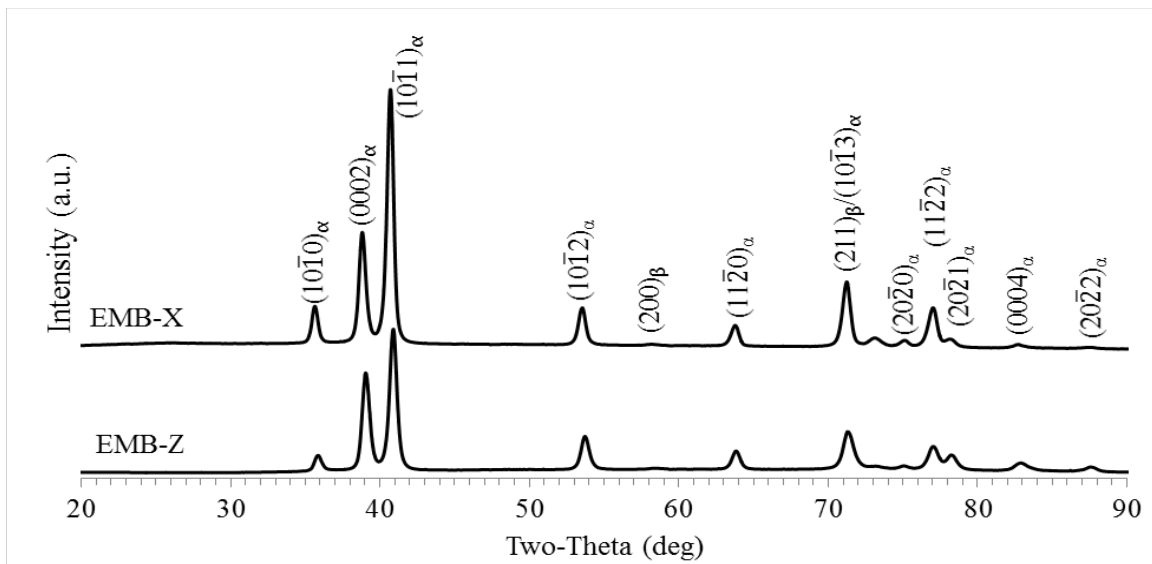


*Figure 31: X-ray diffraction scans of EBM-X and EBM-Z samples*

specimens will play a significant role in the varying mechanical properties: indentation hardness, elastic modulus and yield strength. In addition, effect of grain size on frictional characteristics of many materials have been studied in combination with their wear behavior. The studies show that friction coefficient and in turn wear decreases with a decrease in grain size [35].

## 5.3.2 Mechanical Properties of Ti6Al4V Builds

*Figure 32* shows the mechanical properties of the EBM-built and mill-annealed samples obtained through IIT. *Figure 32 (a)* graphs the elastic modulus for the materials, which show EBM-Z having the greatest followed by comparable values for mill-annealed and EBM-X specimen. The elastic modulus for mill-annealed sample is comparable to the ones listed on the literature: 113.8 GPa [36]. Also, on the same graph is plotted the indentation hardness for different Ti6Al4V builds. Hardness is usually defined in indentation experiments as force divided by the indentation area. Surprisingly,
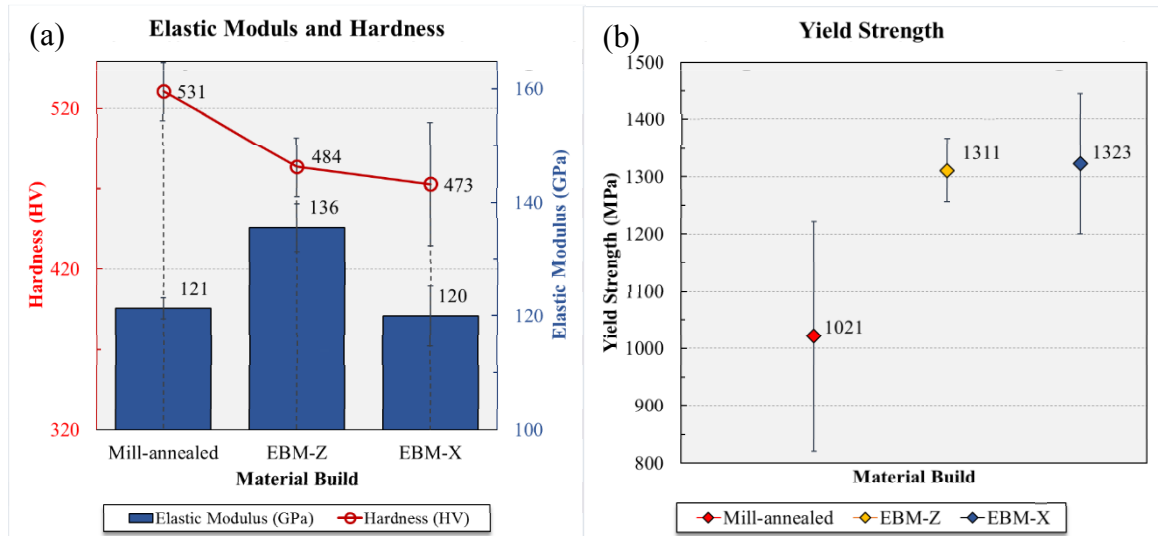


Figure 32: Elastic Modulus, Hardness and Yield Strength of Ti6Al4V builds

in the final product. For the top-most and bottom-most layers of the EBM-built samples, the layers undergo rapid solidification as they are in contact with the relatively cooler stainless steel base plate (for the bottommost layer) and the inert atmosphere inside the machine (for the topmost layer). This causes martensitic microstructure development in the parts. Martensite is a very strong phase for Ti-alloys and results in increased yielding strength of the material. One surprising aspect from the study was the hardness of the material, which is generally directly related with the yield strength of the material were

lower for the EBM-built samples which contradicts the proposed co-relation found in the literature [35]. One possible reason to explain this would be since the micro-hardness was determined locally; the location where the indentations were performed could significantly cause differing results. Literature have shown that hardness in the micro-scale for EBM-built part is dependent on the height of the build. It has been reported that the hardness of the part decreases as the height of the build increases [37]. The sample built for this study is 15 mm tall. Since the sample used to perform the indentation was taken from the middle slice, meaning at a height of 10 mm, it has been reported that the micro-hardness for a build of height 15 mm is approximately around 335 HV, but from this study, it is seen that the Vickers hardness value for EBM is 478.5 HV approximately 150 HV greater than the reported value. Also, mill-annealed sample that showed the greatest hardness of 531 HV has almost double micro hardness as compared to forged-annealed specimens having a hardness value of 349 HV [36]. The greater hardness of mill-annealed specimen is attributed to the post-processing (heat treatment) done on the specimen to impart superior mechanical characteristics. The superior hardness and yield strength of the materials in this study is found to be similar to the results reported by Murr. *et al*. [37].

### 5.3.3 Wear Behavior and influence of the physiological environments

Pin-on-flat wear tests are performed on the polished surfaces to analyze the influence of AM-induced anisotropy and synovial environments on wear resistance. A total of 5 wear tests are carried out each in two preferred orientations for AM built Ti6Al4V while for mill-annealed build, the tests are randomly oriented. Wear volumes are analyzed after image processing and the quantified values obtained are compared across specimens to identify the effects of (i) surface anisotropy, (ii) sliding orientation, and (ii) physiological

environment on the wear mechanism.

*Figure 33* shows the overall wear of each individual material build and their corresponding wear in the PBS and C1 environment. It is revealed that the material wear for all builds in the protein environment C1 is significantly reduced when compared to the aqueous PBS environment.

The tabulated test data for PBS and C1 wear tests is presented in *Table 10.*

*Table 10: Wear Volume Data for tests performed in PBS and C1 environments*

| | Wear Volume ($\mu m^3$) | | | | |
|---|---|---|---|---|---|
| **PBS** | **Mill-annealed** | **EBM-X Vertical** | **EBM-X Horizontal** | **EBM-Z Vertical** | **EBM-Z Angled** |
| Test 1 | 387.54 | 477.32 | 511.70 | 484.25 | 634.77 |
| Test 2 | 205.48 | 517.77 | 745.06 | 595.08 | 591.81 |
| Test 3 | 395.09 | 675.38 | 621.29 | 661.25 | 669.51 |
| Test 4 | 176.43 | 375.67 | 606.58 | 660.24 | 514.56 |
| Test 5 | 318.76 | 571.57 | 588.02 | 538.64 | 770.21 |
| Average | 296.66 | 523.54 | 614.53 | 587.89 | 636.17 |
| S.D (±) | 101.49 | 111.13 | 84.29 | 77.19 | 94.65 |
| S.E (±) | 45.39 | 49.70 | 37.70 | 34.52 | 42.33 |
| **C1** | **Mill-annealed** | **EBM-X Vertical** | **EBM-X Horizontal** | **EBM-Z Vertical** | **EBM-Z Angled** |
| Test 1 | 33.10 | 34.71 | 20.16 | 47.47 | 70.57 |
| Test 2 | 10.78 | 6.87 | 6.21 | 10.74 | 15.29 |
| Test 3 | 14.30 | 48.24 | 47.64 | 27.37 | 37.59 |
| Test 4 | 17.94 | 37.76 | 35.47 | 10.78 | 21.86 |
| Test 5 | 40.35 | 9.87 | 15.76 | 50.51 | 21.75 |
| Average | 23.29 | 27.49 | 25.05 | 29.37 | 33.41 |
| S.D (±) | 12.78 | 18.19 | 16.46 | 19.18 | 22.34 |
| S.E (±) | 5.71 | 8.14 | 7.36 | 8.58 | 9.99 |
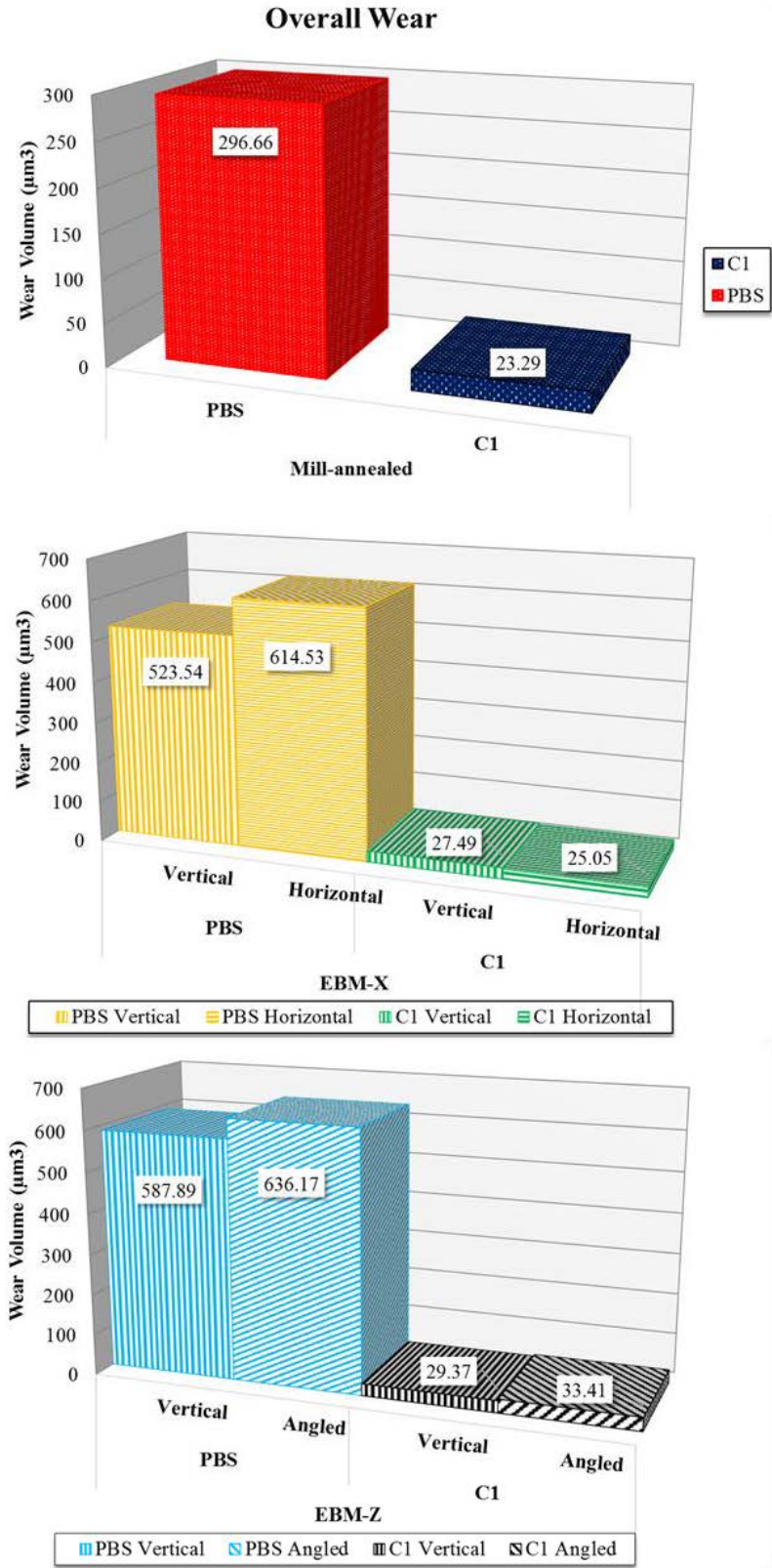
*Figure 33: Overall wear of Ti6Al4V builds on differing environment*

With significant increase in the protein concentration from PBS to C1, it is seen that the lubrication effects significantly prevail. High protein concentration makes the medium more viscous as such the surface energy or wettability of the fluid plays more significant role to promote joint lubrication. Overall, on average material wear decreased by a factor of 12 and 20, for mill-annealed and EBM-built, Ti6Al4V, respectively. *Figure 34* shows the representative SEM micrographs of the morphology of the wear track for the tests performed in PBS and C1 for each individual specimen. It can be clearly seen that the wear width for
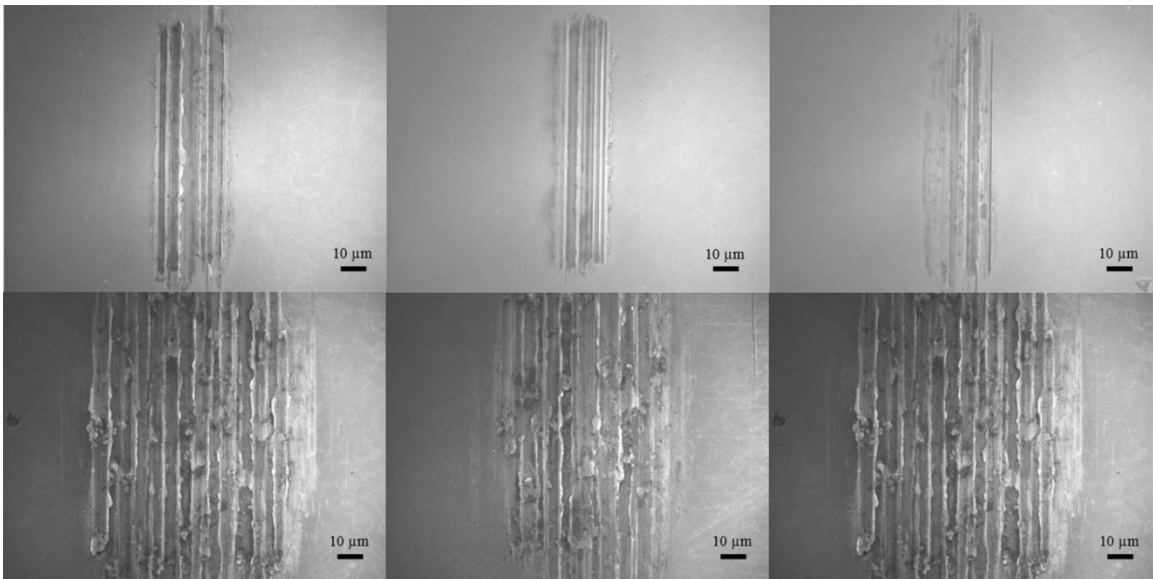


*Figure 34: SEM image showing wear morphology for (a) Mill-annealed (b) EBM-X and (c) EBM-Z specimens, Top row images represent tests performed on C1 while bottom row images show tests performed in PBS solution*

tests performed in PBS solution is significantly greater as compared to the tests performed on C1. The longitudinal grooves seen in the wear tracks in C1 has smaller width and are shallower as compared to the deeper grooves in PBS. It has been known that serum helps improve the lubricating ability of MoM joints by not only providing a boundary-lubricating tribo-film but also reducing the surface tension and consequently improving fluid entrapment in between the interface [38]. The sliding velocity for the pin-on-flat reciprocating test is relatively high with 6 mm/min. For lubricated conditions in both PBS as well as C1, at higher

speed, the hydrodynamic lubricant film forms at the interface and minimizes the wear rate. C1 has greater viscosity as compared to PBS because of an addition of the extracellular matrix HA and protein serum BSA. Since, PBS medium allows lesser fluid entrapment and poorer fluid-film lubrication, greater wear occurs among asperities in contact, which causes increase in the real contact area during sliding. The result of which is greater counter-face wear which is seen as thicker grooves being formed during the reciprocating motion.

To confirm the actual width of the wear track imprinted by the cyclic reciprocating motion of the counter-face on top of the specimen, mating surfaces were inspected under the SEM. *Figure 35* shows the wear morphology for the counter face material *(a)*, magnified in *(b)* and the same wear trench for the specimen *(c)*. The wear width as seen in the *Figure 35* is almost exact. In addition, the wear volume loss was quantified for both mating surfaces and was found to be very close to one another.
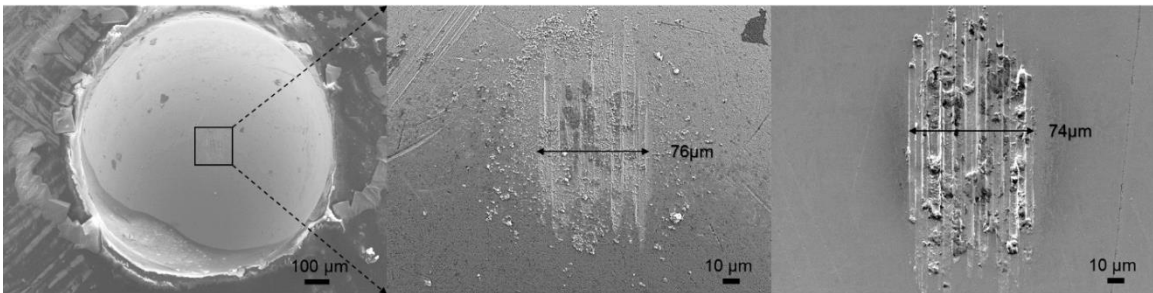


*Figure 35: SEM micrograph showing wear track on counter-face 1mm CP grade-2 Ti (a) and (b), PBS test on EBM-Z*

*Figure 36 (a)* and *(b)* shows the overall wear in PBS and C1 physiological solutions. In the PBS environment, mill-annealed specimen showed the greatest wear resistance, while comparable wear volumes were observed in the EBM-built samples. The effect of anisotropy was not severe among the samples. Among the AM builds, on average, EBM-X showed greater wear resistance, with tests performed along the layer orientation having the least wear when compared to tests across the layer build deposition.
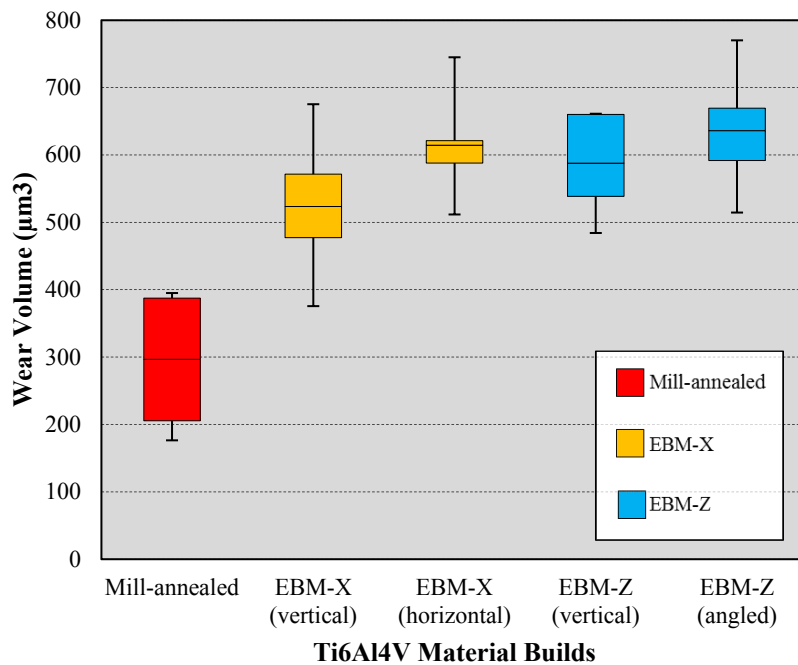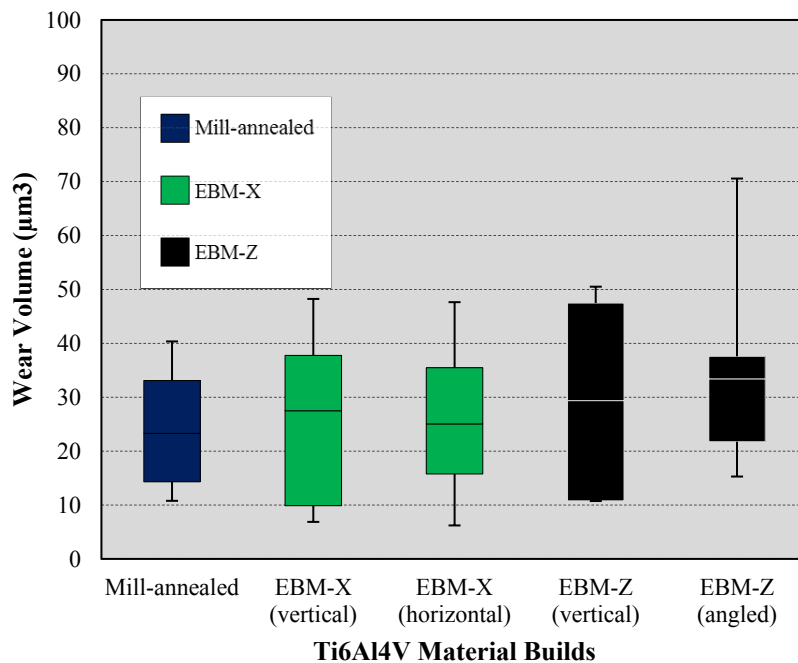
*Figure 36: Box-plot showing overall wear response of Ti6Al4V specimens as a function of build orientation and sliding direction in different physiological solutions (a) PBS (b) Concentration C1 (PBS+HA+BSA)*

The wear volume for tests performed in the horizontal direction (across the layer) increased by 17 %. For the EBM-Z specimen having transversely isotropic properties, a variation of 8 % in wear volume was observed. Tests performed at a diagonal direction to the two edges of the sample showed superior wear resistance in contrast to the vertically oriented test. In most cases, the standard deviation for all of the tests in PBS environment appeared consistent.

The tests performed in the C1 protein concentrated environment showed significant reduction in the wear. Similar trend in the material's wear response was seen with mill-annealed specimen being the most wear resistant while both the EBM-builds had comparable wear volumes. The effect of anisotropy is revealed insignificant again while comparatively EBM-Z had greater wear. The wear response as a result of test orientation reversed in the case of EBM-X specimen with greater wear on tests along the build layers in contrast to the tests performed across the layers. The wear increased by 8 % for the horizontal direction. The wear response with test orientation remained the same for EBM-Z specimens with diagonally oriented tests having greater wear compared to vertically oriented tests. The standard deviations on all the tests appear greater as compared to the PBS environment meaning greater variance occurred in the protein rich environment.

Additionally, a one-way analysis of variance (ANOVA) test was performed to determine if the means of the wear volume for the additively manufactured samples were statistically different from one another. The results from one-way ANOVA is presented in *Table 11*. The results show that in both the cases, there were no statistically significant differences between group means as determined by one-way ANOVA at the $p < 0.05$ level for the four conditions: EBM-X D1, D2, EBM-Z D1 and D2 [$F_{(3,16)} = 1.39$, $p = 0.28$] for

PBS tests and [$F(3,16) = 0.17$, $p = 0.92$] for C1 tests. This means that the effect of the sliding test directions seemed insignificant.

*Table 11: One-way ANOVA results for wear volumes of EBM-X and EBM-Z specimens*

| ANOVA for test performed in PBS environment | | | | | | |
|---|---|---|---|---|---|---|
| ***Source of Variation*** | ***SS*** | ***df*** | ***MS*** | ***F*** | ***P-value*** | ***F crit*** |
| Between Groups | 35766.66 | 3.00 | 11922.22 | 1.39 | **0.28** | 3.24 |
| Within Groups | 137494.60 | 16.00 | 8593.41 | | | |
| | | | | | | |
| Total | 173261.26 | 19.00 | | | | |
| ANOVA for test performed in C1 environment | | | | | | |
| ***Source of Variation*** | ***SS*** | ***df*** | ***MS*** | ***F*** | ***P-value*** | ***F crit*** |
| Between Groups | 186.85 | 3.00 | 62.28 | 0.17 | **0.92** | 3.24 |
| Within Groups | 5875.64 | 16.00 | 367.23 | | | |
| | | | | | | |
| Total | 6062.48 | 19.00 | | | | |

The wear response of the materials can be interpreted by the mechanical properties imposed by each individual specimen. Archard's model considers wear rate of metals as an inverse function of their hardness. Meaning, greater the hardness of a material higher is its resistance to wear. Mill-annealed specimen for both cases of the test environment cordially exhibits Archard's law. However, EBM-built samples do not fully exhibit the trend. Apparently, the hardness varies within 3 % between the two EBM specimens. The abrasive wear resistance of a material is known to be dependent on the hardness/modulus ratio (H/E) for tests performed in similar environment and test conditions. A material whose H/E ratio is high provides greatest resistance to wear. The ratio shows that abrasive wear resistance of a material can be increased either by increasing the hardness or by decreasing the elastic modulus [35]. *Table 12* shows the H/E ratio for mill-annealed, EBM-X and EBM-Z specimen calculated by simply taking the ratios of the average indentation hardness and elastic modulus obtained from IIT.

*Table 12: Hardness to Elastic Modulus ratio for Ti6Al4V builds*

| Materials | Value H/E ratio | Wear volume ($\mu m^3$) | |
| --- | --- | --- | --- |
| | | PBS | C1 |
| Mill-annealed | 4.39 | 296.66 | 23.29 |
| EBM-X | 3.94 | 569.04 | 26.27 |
| EBM-Z | 3.56 | 612.03 | 31.39 |

The ratio shows greatest value for mill-annealed, followed by, vertically sliced EBM-X specimen and by horizontally sliced EBM-Z specimen. Interestingly, in both cases of the test environment PBS and C1, the wear response follows inversely to the H/E ratio. The results obtained show that H/E ratio provides a good measure in correlating the wear response of the material to the combined effects of their corresponding hardness and elastic modulus.

## 5.4 Conclusion

It has been shown that conventionally manufactured mill-annealed specimen shows superior wear due to well-established homogeneous isotropic grain morphology. Therefore, regardless of sliding motions and working environments, the wear behavior exhibits consistent nature tribological response. It is more evident that the resistivity of the mill-annealed specimen against tribocorrosion is superior than EBM built Ti6Al4V specimens. However, the clearly shown anisotropic effect of the EBM-built samples on dry wear is now less significant in PBS. EBM-X illustrated superior wear-corrosion resistivity than EBM-Z in both test environments. Sliding direction does not affect wear trend for both EBM-X and EBM-Z specimen in PBS.

Improved wettability and greater viscosity of protein-extracellular matrix (C1) construct stable lubricative layer that inhibits direct contact of slider tip on specimen surface. Consequently, it considerably reduces wear damage on all specimen surfaces.

Overall, the experimental study investigated the wear response of conventionally manufactured Ti6Al4V with additively manufactured (AM), EBM-Ti6Al4V in relation to surface anisotropy, varying physiological environments and sliding orientations. The tribological response of the material is in accordance to the measured mechanical properties. The combined influence of anisotropic grain morphology and synovial fluid lubrication is very complicated to understand the wear resistivity of EBM-built implants. The superior wear resistance of mill-annealed specimen suggests post process and heat treatment may be necessary for biomedical applications of EBM built Ti6Al4V.

## 5.5 References

1. Hussein, M. A., Mohammed, A. S., & Al-Aqeeli, N. (2015). Wear characteristics of metallic biomaterials: a review. *Materials*, *8*(5), 2749-2768.

2. Molinari, A., Straffelini, G., Tesi, B., & Bacci, T. (1997). Dry sliding wear mechanisms of the Ti6Al4V alloy. *Wear*, *208*(1), 105-112.

3. Kok, Y., Tan, X., Tor, S. B., & Chua, C. K. (2015). Fabrication and microstructural characterisation of additive manufactured Ti-6Al-4V parts by electron beam melting: This paper reports that the microstructure and micro-hardness of an EMB part is thickness dependent. *Virtual and Physical Prototyping*, *10*(1), 13-21.

4. Do, D. K., & Li, P. (2016). The effect of laser energy input on the microstructure, physical and mechanical properties of Ti-6Al-4V alloys by selective laser melting. *Virtual and Physical Prototyping*, *11*(1), 41-47.

5. Al-Bermani, S. S., Blackmore, M. L., Zhang, W., & Todd, I. (2010). The origin of microstructural diversity, texture, and mechanical properties in electron beam melted Ti-6Al-4V. *Metallurgical and materials transactions a*, *41*(13), 3422-3434.

6. Rafi, H. K., Karthik, N. V., Gong, H., Starr, T. L., & Stucker, B. E. (2013). Microstructures and mechanical properties of Ti6Al4V parts fabricated by selective laser melting and electron beam melting. *Journal of Materials Engineering and Performance*, *22*(12), 3872-3883.

7. Galarraga, H., Lados, D. A., Dehoff, R. R., Kirka, M. M., & Nandwana, P. (2016). Effects of the microstructure and porosity on properties of Ti-6Al-4V ELI alloy fabricated by electron beam melting (EBM). *Additive Manufacturing*, *10*, 47-57.

8. Lu, S. L., Tang, H. P., Ning, Y. P., Liu, N., StJohn, D. H., & Qian, M. (2015). Microstructure and mechanical properties of long Ti-6Al-4V rods additively manufactured by selective electron beam melting out of a deep powder bed and the effect of subsequent hot isostatic pressing. *Metallurgical and Materials Transactions A*, *46*(9), 3824-3834.

9. Sreekanth, P. R., & Kanagaraj, S. (2013). Wear of Biomedical Implants. In *Tribology for Scientists and Engineers* (pp. 657-674). Springer New York.

10. Kurtz, S., Ong, K., Lau, E., Mowat, F., & Halpern, M. (2007). Projections of primary and revision hip and knee arthroplasty in the United States from 2005 to 2030. *J Bone Joint Surg Am*, *89*(4), 780-785.

11. Doorn, P. F., Campbell, P. A., & Amstutz, H. C. (1996). Metal Versus Polyethylene Wear Particles in Total Hip Replacements: A Review. *Clinical orthopaedics and related research*, *329*, S206-S216.

12. Kohn, D. H. (1998). Metals in medical applications. *Current Opinion in Solid State and Materials Science*, *3*(3), 309-316.

13. Pabinger, C., Biedermann, R., Stöckl, B., Fischer, M., & Krismer, M. (2003). Migration of metal-on-metal versus ceramic-on-polyethylene hip prostheses. *Clinical orthopaedics and related research*, *412*, 103-110.

14. Park, J. B., & Bronzino, J. D. (2000). The biomedical engineering handbook. *Boca Raton, FL: CRC Press*, *4*, 1-8.

15. Dorr, L. D., Wan, Z., Longjohn, D. B., Dubois, B., & Murken, R. (2000). Total hip arthroplasty with use of the Metasul metal-on-metal articulation. *J Bone Joint Surg Am*, *82*(6), 789-789.

16. Ahlroos, T., & Saikko, V. (1997). Wear of prosthetic joint materials in various lubricants. *Wear*, *211*(1), 113-119.

17. Tipper, J. L., Ingham, E., Jin, Z. M., & Fisher, J. (2005). (iv) The science of metal-on-metal articulation. *Current Orthopaedics*, *19*(4), 280-287.

18. Amstutz, H. C., Campbell, P., Kossovsky, N., & Clarke, I. C. (1992). Mechanism and clinical significance of wear debris-induced osteolysis. *Clinical orthopaedics and related research*, *276*, 7-18.

19. Herb, K., Cho, S., & Stiles, M. A. (2006). Temporomandibular joint pain and dysfunction. *Current pain and headache reports*, *10*(6), 408-414.

20. Marchetti, C., Bernasconi, G., Reguzzoni, M., & Farina, A. (1997). The articular disc surface in different functional conditions of the human temporomandibular joint. *Journal of oral pathology & medicine*, *26*(6), 278-282.

21. Lucas, L. C., Buchanan, R. A., Lemons, J. E., & Griffin, C. D. (1982). Susceptibility of surgical cobalt-base alloy to pitting corrosion. *Journal of biomedical materials research*, *16*(6), 799-810.

22. Merritt, K., & Brown, S. A. (1996). Distribution of cobalt chromium wear and corrosion products and biologic reactions. *Clinical Orthopaedics and Related Research*, *329*, S233-S243.

23. Woodman, J. L., Black, J., & Jiminez, S. A. (1984). Isolation of serum protein organometallic corrosion products from 316LSS and HS-21 in vitro and in vivo. *Journal of Biomedical Materials Research Part A*, *18*(1), 99-114.

24. Essner, A., Schmidig, G., & Wang, A. (2005). The clinical relevance of hip joint simulator testing: in vitro and in vivo comparisons. *Wear*, *259*(7), 882-886.

25. Hall, R. M., Bankes, M. J. K., & Blunn, G. (2001). Biotribology for joint replacement. *Current Orthopaedics*, *15*(4), 281-290.

26. Moharrami, N., Langton, D. J., Sayginer, O., & Bull, S. J. (2013). Why does titanium alloy wear cobalt chrome alloy despite lower bulk hardness: a nanoindentation study?. *Thin Solid Films*, *549*, 79-86.

27. Hirakawa, K., Jacobs, J. J., Urban, R., & Saito, T. (2004). Mechanisms of failure of total hip replacements: lessons learned from retrieval studies. *Clinical orthopaedics and related research*, *420*, 10-17.

28. Niki, Y., Matsumoto, H., Otani, T., Yoshimine, F., Inokuchi, W., & Morisue, H. (2003). Gigantic popliteal synovial cyst caused by wear particles after total knee arthroplasty. *The Journal of arthroplasty*, *18*(8), 1071-1075.

29. Jo, E. (2012). Normal Joint Structure. Notes on Rheumato-logy. *University College London. Archived from the ori-ginal on*, *19*.

30. McGregor, D. B., Baan, R. A., Partensky, C., Rice, J. M., & Wilbourn, J. D. (2000). Evaluation of the carcinogenic risks to humans associated with surgical implants and other foreign bodies—a report of an IARC Monographs Programme Meeting. *European journal of cancer*, *36*(3), 307-313.

31. Li, Y., Yang, C., Zhao, H., Qu, S., Li, X., & Li, Y. (2014). New developments of Ti-based alloys for biomedical applications. *Materials*, *7*(3), 1709-1800.

32. Nag, S., Banerjee, R., & Fraser, H. L. (2005). Microstructural evolution and strengthening mechanisms in Ti–Nb–Zr–Ta, Ti–Mo–Zr–Fe and Ti–15Mo biocompatible alloys. *Materials Science and Engineering: C*, *25*(3), 357-362.

33. Bortel, E. L., Charbonnier, B., & Heuberger, R. (2015). Development of a synthetic synovial fluid for tribological testing. *Lubricants*, *3*(4), 664-686.

34. Blewis, M. E., Nugent-Derfus, G. E., Schmidt, T. A., Schumacher, B. L., & Sah, R. L. (2007). A model of synovial fluid lubricant composition in normal and injured joints. *Eur Cell Mater*, *13*, 26-39.

35. Menezes, P. L., Ingole, S. P., Nosonovsky, M., Kailas, S. V., & Lovell, M. R. (2013). *Tribology for scientists and engineers*. Springer, New York.

36. Yan, M., & Yu, P. (2015). An Overview of Densification, Microstructure and Mechanical Property of Additively Manufactured Ti-6Al-4V—Comparison among Selective Laser Melting, Electron Beam Melting, Laser Metal Deposition and Selective Laser Sintering, and with Conventional Powder. In *Sintering Techniques of Materials*. InTech.

37. Murr, L. E., Esquivel, E. V., Quinones, S. A., Gaytan, S. M., Lopez, M. I., Martinez, E. Y., ... & Stafford, S. W. (2009). Microstructures and mechanical properties of electron beam-rapid manufactured Ti–6Al–4V biomedical prototypes compared to wrought Ti–6Al–4V. *Materials characterization*, *60*(2), 96-105.

38. Curran, S., Hoskin, T., Williams, S., Scholes, S. C., Kinbrum, A., & Unsworth, A. (2013). Does surface wettability influence the friction and wear of large-diameter CoCrMo alloy hip resurfacings?. *Proceedings of the Institution of Mechanical Engineers, Part H: Journal of Engineering in Medicine*, *227*(8), 847-858.

# Chapter 6: Conclusion and Future Works

The surface damage of EBM built Ti6Al4V was examined in the context of process-induced anisotropy and environment. A nanoindenter-based micro scale fretting wear test provided a first glimpse at the effects of surface grain structure on dry and wet wear mechanisms. This technique allows for different grain structure near the surface to be scratched with well-characterized single asperity contact with microscale resolution.

In order to identify grain structure in the electron beam melting processed Ti6Al4V as a function of build orientation, specimen surfaces with different printing patterns were ground and polished to be mirror-like surface. The mirror finished specimen surfaces were subjected to continuous cyclic sliding contact against a pure titanium sphere to simulate fretting motion at femoral head-femoral stem interfaces. This experiment was repeated in three different environments (ambient with ~35% humidity, phosphate buffer saline solution, and protein-hyaluronic acid solution) to understand the influence of synovial joint fluid on wear mechanism. Metallographic microscopy and profilometric measurement allows precise characterization of surface morphology and tribological responses. This experimental technique with high resolution of depth-sensing nanoindentation provides opportunities to study process-dependent mechanical-chemical surface failure.

Fundamental mechanical responses against depth-sensing nanoindentation present the greatest hardness on mill-annealed surface while highest elastic modulus on vertically developed EBM part. Hardness to elastic modulus ratio (H/E) indicates mill-annealed Ti6Al4V possesses superior mechanical properties. However, dry wear tests result in the least wear resistance on mill-annealed Ti6Al4V surface. As illustrated in Hall-Petch relationship, small grain size increases resistance to plastic deformation and therefore

suppresses mobility of cross-slip of dislocations through grain boundaries. Small wear rate of EBM built specimen surfaces can be explained by fine lamellar α grains that delays dislocation pile-ups and confined volume of plastic zone. Hence, contact stress with relatively higher friction coefficient in ambient environment would be consumed to break the titanium oxide layer rather than plastically deform the subsurface. This is often referred to as the oxidative wear. Mechanical contact of similar materials (titanium slider on titanium alloy surface) leads to greater friction heat and microwelding as soon as the oxide layer is damaged. In the early stage of reciprocating motion, alternation of oxidative wear and adhesive tear-off takes place, and subsequent shearing motion induces dislocations along the maximum shear plane. Continuous reciprocating shearing motion of slider head, once dislocations are accumulated results in microscale slip bands to be produced. Dislocation pile-up will ultimately reach to critical size and turn into microcrack. This hypothesis would be explained by the very low shear strength and small strain-hardening behavior of Ti6Al4V. Micrographic inspection clearly presented two-layered debris band surrounding wear trench, i.e. fine TiO debris at outer-band and larger plastically deformed metal particles at inner-band. It implies there would be transition of wear mechanisms during a course of fretting motions. It is also notable that this transition of wear mechanism was not observed in the previous wear experiment using silicon nitride spheres on EBM built Ti6Al4V in Chapter 3.

Wear damage rate in PBS increases compared to dry wear tests. In liquid condition, boundary lubrication would reduce the friction coefficient and convection heat transfer may moderate friction heat at the contact area. In addition, PBS solution would play a role as electrolyte that helps stable TiO layer regrowth continuously. Hence, contact stress will

be released mainly by plastic deformation of the subsurface. As discussed, Ti6Al4V exhibits lower shear strength, insignificant strain hardening behavior, as well as sensitivity to strain rate. As a result, the dominant wear mechanism in PBS would be surface fatigue delamination. Accumulated dislocations will be transformed to microcracks and these microcracks will be propagated. Ultimately, contact residual stress and contact pressure accelerate surface fatigue, and produce large plate-like wear particles. Very brittle wear particles due to plastic deformation and oxidation will plough the plastically deformed surfaces. Consequently, during fatigue sliding contact in PBS solution, wear rate could be exponentially accelerated with cycles of sliding.

In albumin-hyaluronic acid solution, the protein-extracellular matrix layer completely separates direct contact of slider head. The higher viscosity and lower surface tension enable smooth synovial lubrication. As a result, the wear rate decreased drastically on all Ti6Al4V specimens.

In summary, significant findings through this project are:

- Experimental results from dry wear test illustrated anisotropic behavior of EBM built Ti6Al4V implant materials.

- In ambient environment, it is evident that the wear mechanism changes from oxidative wear to fatigue wear.

- In PBS, environmental electrochemistry and mechanical contact are synergistically combined to accelerate surface damage.

- Existence of protein-extracellular matrix improves joint lubrication. It is important to secure the stable biochemical environment that enables to maintain effective synovial lubrication.

# VITA

*Sanjay Shrestha was born in Banepa, Nepal on December 1991. He completed his high school and undergraduate degree from Kathmandu University, Dhulikhel, Nepal. Between 2009 and 2013, he earned a degree of Bachelor's of Science in Engineering majoring in Mechanical Engineering. He was admitted to Youngstown State University, Department of Mechanical and Industrial Engineering in January 2014 where he worked as a graduate research assistant under Dr. Guha Manogharan and Dr. Jae Joong Ryu and completed his research successfully. He is expected to receive a Master of Science in Mechanical Engineering degree in May 2017.*